ENSO Initiation Mechanisms

By

Erin E. Thomas

A dissertation submitted in partial fulfillment of
the requirements for the degree of

Doctor of Philosophy
(Atmospheric and Oceanic Sciences)

at the
UNIVERSITY OF WISCONSIN-MADISON
2017

Date of final oral examination: 12/04/2017

The dissertation is approved by the following members of the Final Oral Committee:
Dr. Daniel J. Vimont, Professor, Atmospheric and Oceanic Sciences
Dr. Galen McKinley, Adjunct Professor, Atmospheric and Oceanic Sciences,
Professor, Earth and Environmental Sciences, Columbia University
Dr. Ankur Desai, Professor, Atmospheric and Oceanic Sciences
Dr. Tristan L'Ecuyer, Professor, Atmospheric and Oceanic Sciences
Dr. Greg Nemet, Associate Professor, Public Affairs and Env. Studies
Dr. Matthew Newman, Adjunct Professor, Atmospheric and Oceanic Sciences,
Senior Research Scientist, CIRES; NOAA-Physical Sciences Division

Abstract

ENSO Initiation Mechanisms

by Erin E. Thomas

El Niño-Southern Oscillation (ENSO) variability is influenced by numerous oceanic and atmospheric phenomena which complicate our ability to predict and analyze the mechanisms responsible for generating ENSO diversity. This research utilizes statistical and physical modeling to identify both observationally-grounded and physically meaningful mechanisms that influence ENSO development.

Interactions between the Pacific Meridional Mode (PMM) and ENSO are investigated using the National Center for Atmospheric Research (NCAR) Community Earth System Model (CESM) and an intermediate coupled model (ICM). The two models are configured so that the CESM simulates the PMM but not ENSO, and the ICM simulates ENSO but not the PMM, allowing for a clean separation between the PMM evolution and the subsequent ENSO response. An ensemble of CESM simulations is run with an imposed surface heat flux associated with the North Pacific Oscillation (NPO) generating a sea surface temperature (SST) and wind response representative of the PMM. The PMM wind is then applied as a forcing to the ICM to simulate the ENSO response. The positive (negative) ensemble-mean PMM wind forcing results in a warm (cold) ENSO event although the responses are not symmetric (warm ENSO events are larger in amplitude than cold ENSO events), and large variability between ensemble members suggests that

any individual ENSO event is strongly influenced by natural variability contained within the CESM simulations. Sensitivity experiments show that (i) direct forcing of Kelvin waves by PMM winds dominates the ENSO response, (ii) seasonality of PMM forcing and ENSO growth rates influences the resulting ENSO amplitude, (iii) ocean dynamics within the ICM dominate the ENSO asymmetry, and (iv) the nonlinear relationship between PMM wind anomalies and surface wind stress may enhance the La Niña response to negative PMM variations. Implications for ENSO variability are discussed.

In a forecasting framework, the predictability of ENSO events depends on the characteristics of both the forecast initial conditions as well as the stochastic forcing that occurs after the forecast is initialized. In this framework, stochastic forcing is capable of improving the predictability of the ENSO event if it excites optimal initial conditions that maximize deterministic ENSO growth. However, it can also be detrimental to the predictability of the event if it excites unpredictable growth or interference after the forecast is initialized. This study describes an empirical framework using Linear Inverse Modeling (LIM) techniques that identifies observationally-grounded spatial and temporal characteristics of the stochastic forcing that contributes to the development of ENSO diversity. The noise forcing patterns show NPO-like patterns are associated with the development of CP conditions and South Pacific Oscillation (SPO)-like conditions as well as positive zonal wind anomalies in the western Pacific are associated with EP development. We apply this framework to several historical ENSO events containing a diverse range of spatial and temporal characteristics to estimate the relative roles of deterministic dynamics

versus noise forcing towards ENSO diversity. Overall it is determined ENSO events are impacted by a large variety of phenomena that can influence the event throughout its evolution. Additionally, the role of noise forcing for ENSO development varies greatly for any given event and characterizing the structures within the noise forcing is challenging. However, the methods described in this study provides a single framework for parsing through the myriad processes that contribute to ENSO diversity.

The LIM framework is used to calculate the noise forcing patterns associated with generating ENSO diversity within NCAR's CESM. The noise forcing structures identified within the model match the observed noise forcing well. The results show an NPO-like pattern during boreal winter (DJF) associated with the CP optimal initial conditions. The SPO-like pattern in the southern Hemisphere and positive zonal wind stress anomalies in the western Pacific also appear in relation to the EP optimal initial conditions although they occur during JJA in the CESM, rather than MAM as seen in observations. These noise forcing structures of interest are then used to force three sets of ensemble experiments using the fully-coupled CESM to determine the physical mechanisms through which they are able to initiate ENSO events. The results support previous findings and show the NPO is capable of initiating ENSO variability through the PMM. Interestingly, neither EP noise forced experiments generate ENSO events. However, the SPO heat flux forcing experiment creates an SST pattern that resembles the EP optimal and the equatorial wind stress experiment generate a thermocline structure that resembles part of the EP optimal.

These results overwhelming indicate that the noise forcing plays a critical role in the development of ENSO diversity. Unfortunately, noise forcing is highly variable and may or may not be important in the development of any given ENSO event. This has important implications for the skill to which ENSO events can be predicted.

This work is dedicated to my wonderful family and friends. Your positive presence in my life made the last several years not only productive but incredibly enjoyable.

Acknowledgements

Many people made this dissertation possible. First of all, none of this would have been possible without the guidance from my advisor, Dan Vimont. Thank you for providing me with this opportunity and shaping my graduate career. Your positive attitude has been an integral part of the success of this research and making my overall experience at the University of Wisconsin one I will cherish for years to come. Additionally, thank you to all of my committee members for valuable comments and helpful input throughout this entire process. Also, thank you to Matt Newman and Mike Alexander at NOAA ESRL/CIRES in Boulder, Co for a fun winter full of linear inverse modeling and snowboarding.

Second, my friends have been wonderfully supportive. Claire, Elin, Elena and Alex: you all have been incredibly supportive and optimistic throughout this process. Your friendship is irreplaceable and means more to me than I will ever be able to express. I am incredibly fortunate to have you all in my life and look forward to our future adventures!

Third my family have forever been my largest support system. Thank you, Mom and Dad, for always taking my (sometimes too frequent) phone calls in good humor. You have provided a safe, supportive and non-judgmental environment to discuss topics ranging from science to shoes. I am so thankful for everything you have done for me over the years. Also, thanks to my brother, Brendan, for constantly grounding me, providing the big picture and for being my comic relief whether it was needed or not. You three are my constants and without your love I would not be where I am today.

Additionally, thanks to Claire Pettersen and Anne Sophie Daloz for proofreading several parts of this dissertation and Sarah Larson for invaluable discussions about the CESM model which made the last chapter of this dissertation possible. Furthermore, thank you

all my current co-authors (Dan Vimont, Matt Newman, Cecile Penland, Michael Alexander and Cristian Martinez-Villalobos) for help in the preparation of several chapters contained within which have already been published or submitted for publication.

Finally, The Community Earth System Model (CESM) project is supported by the National Science Foundation and the Office of Science of the U.S. Department of Energy. Computing resources were provided by the Climate Simulation Laboratory at the National Center for Atmospheric Research's (NCAR) Computational and Information Systems Laboratory (CISL), sponsored by the National Science Foundation and other agencies. This work was supported by the National Science Foundation (NSF) under Climate and Large Scale Dynamics Grant 1463970, the United States Department of Energy (DOE) Project DE-SC0005301, and The University of Wisconsin Climate, People and Environment Program.

Contents

List of Figures

List of Tables

Abbreviations

CESM	**C**ommunity **E**arth **S**ystem **M**odel
CP	**C**entral **P**acific
ENSO	**E**l **N**iño **S**outhern **O**scillation
EP	**E**astern **P**acific
ICM	**I**ntermediate **C**oupled **M**odel
KW	**K**elvin **W**ave
NPO	**N**orth **P**acific **O**scillation
PMM	**P**acific **M**eridional **M**ode
RW	**R**ossby **W**ave
SPO	**S**outh **P**acific **O**scillation
SPMM	**S**outh **P**acific **M**eridional **M**ode
SSH	**S**ea **S**urface **H**eight
SST	**S**ea **S**urface **T**emperature

Chapter 1

Introduction

1.1 El Niño - Southern Oscillation

El Niño - Southern Oscillation (ENSO) is the largest source of interannual variability in the tropical Pacific (McPhaden et al., 2006, Philander, 1990, Wallace et al., 1998). ENSO variability comprises both warm events (El Niño) and cold events (La Niña) which typically reach peak magnitude during Northern Hemisphere winter. ENSO alters the location of the warmest sea surface temperature (SST) which, in turn, shifts the location of the tropical convection (Graham and Barnett, 1987). The state of ENSO can significantly affect global climate patterns since deep convection in the tropics is a major energy source driving global scale atmospheric circulation (Gill 1980; Hoskins and Karoly 1981; Hirst 1986; Jin and Hoskins 1995; Trenberth et el. 1998; Neelin et al. 1998; Hoerling et al. 1997; Diaz et al. 2001; Alexander et al. 2002). ENSO climate teleconnections often result in extreme regional impacts such as changes in rainfall, droughts, heat waves, forest

fires, flooding, landslides, and crop failures across the globe (Caviedes 1975; Enfield 1989; Alexander et al. 2002). Typical El Niño climate impacts are summarized in Figure 1.1.

Understanding ENSO behavior and predicting ENSO events is critical given the widespread and often destructive impacts. However, understanding ENSO behavior is not a simple task. Many phenomena are known to be capable of influencing the spatial and temporal characteristics of ENSO variability: including the Madden-Julian Oscillation, westerly wind busts, extratropical atmospheric forcing, and thermocline dynamics among others (e.g. Anderson et al. 2013; Batstone and Hendon 2005; Boschat et al. 2013; Cane and Zebiak 1985; Battisti 1988; Capotondi et al. 2015; Chang et al. 2007; Chen et al. 2015; Fedorov et al. 2015; Gebbie et al. 2007; Larson and Kirtman 2013; Kapur et al. 2011; Kapur and Zhang 2012; Lengaigne et al. 2002, 2004; Levine and Jin 2017; Moore and Kleeman 1999; Penland 1996; Vimont et al. 2003a,b; Wang and An 2002; Karnauskas 2013). Additionally, it has been shown the spatial structures of each ENSO event can vary widely, thus generating significantly different climatic impacts (Larkin and Harrison 2005; Kumar et al. 2006; Ashok et al. 2007; Weng et al. 2007, 2009; Kao and Yu 2009).

El Niño events occur approximately every two to seven years. However, the timing, magnitude, evolution, and spatial patterns of these events is highly variable (e.g. Penland 2010, Capotondi et al. 2015; Deser et al. 2012). Such large diversity introduces difficulties when it comes to fully understanding the ENSO dynamics and accurately predicting these events. One highly active area of ENSO research focuses on the physical mechanisms capable of initiating ENSO events (e.g. Vimont 2003a, b; Larson and Kirtman 2013, 2014; McPhaden 1999). Characterizing the underlying processes of ENSO initiation should improve our ability to predict events with greater lead times, and therefore provide more time to prepare for potential climate impacts. The skill of these predictions depends on our knowledge of the complicated interactions between the processes that influence ENSO

initiation and development (Latif et al. 1998; Jin et al. 2008; Hu et al. 2014; Dayan et al. 2014; Newman and Sardeshmukh 2017). The research presented in this dissertation explores some of the mechanisms that can generate ENSO.

1.2 History of ENSO

Fishermen off the coast of Peru were aware of changes in the local ocean currents long before written records were being made (Enfield 1989). Knowledge of changes in the direction and temperature of the local ocean currents that influenced the quality of the local fisheries was orally passed from generation to generation. The first written record of this semi-regular phenomenon occurring at the end of the calendar year was made by explorer Fransisco Pizarro in the 1500's (Enfield 1989; Murphy 1926). This phenomenon termed "El Niño" was first thought to be a counter-current (Pezet 1895). In 1895, Pezet addressed the 6th International Geographical Congress in London about the ocean current changes noted by the South American fishermen claiming observations such as warm water arriving at the end of the calendar year at irregular intervals and coincident climate impacts such as anomalous rain and winds. In the early 1900's several more studies were published mentioning specific observations of the changes in temperature, direction and timing of local ocean currents in the equatorial regions off the west coast of South America (Coker 1918; Murphy 1923, 1926; Walcott 1925).

The origin of what is now known as the Southern Oscillation began in the late 1800's and early 1900's, with attempts to forecast the monsoon in India and Northern Australia by studying patterns of atmospheric pressure over large spatial areas in the Pacific (Lockyer and Lockyer 1902). Sir Gilbert Walker first coined the term "Southern Oscillation" in the early 1920's and published several papers discussing global atmosphere weather patterns,

in which he defines the Southern Oscillation using surface pressure in several different locations around the southern Pacific ocean (Walker 1928, 1932).

The beginning of our understanding of the couped ocean - atmosphere mode of variability we now refer to as ENSO started in the late 1960's. Bjerknes (1969) showed the relationship between the ocean phenomenon near the coast of South America referred to as El Niño and the atmospheric pressure pattern known as the Southern Oscillation. Bjerknes (1969) is the first to suggest the tropical atmosphere and ocean are coupled, thus generating a paradigm shift in how researchers viewed tropical Pacific variability. Bjerknes (1969) described an air-sea coupling feedback, now referred to as the Bjerknes feedback. This positive feedback mechanism is understood to be a prominent mechanism necessary for the growth of ENSO events (e.g. Neelin et al. 1998; Sheinbaum 2003). The Bjerknes feedback mechanism works as thus: decreasing the strength of the equatorial easterlies related to changes in the Southern Oscillation reduces equatorial upwelling, which in turn increases SST. These positive SST anomalies decrease the zonal temperature gradient which further reduces the Walker circulation. Bjerknes (1969) suggested this feedback may generate a self-sustained cycle, although he did not provide a process that could generate a "turnabout between trends". A mechanism responsible for switching from warm El Niño conditions to the cool La Niña state was not provided until an understanding of ocean basin adjustment and wave theory was developed (refer to Section 1.3).

The occurrence of the strong 1982-1983 El Niño event triggered another fundamental shift in the field of ENSO research: prior to this event, most research focused on the development of individual events and understanding the mechanisms that generated warm SST anomalies in the eastern equatorial Pacific ocean. However, little work had been done to identify the cause of the irregular periodicity/behaviors of ENSO. This resulted in a failure to predict the large magnitude 1982-1983 El Niño event which developed in

an unexpected way (Gill and Rasmusson 1983). The failure to predict the occurrence of this extreme event motivated the launch of the Tropical Ocean-Atmosphere (TAO) array and Tropical Ocean - Global Atmosphere (TOGA) program to generate in-situ observations of SST, subsurface temperature, sea level, ocean velocity and surface winds in the equatorial Pacific (McPhaden et al. 1998; Wallace et al. 1998). Additionally, there was a large increase in modeling studies to further understand the complexity of ENSO dynamics employing a full hierarchy of models (from simple, parameterized toy models to the complex, fully-coupled global climate models) (Neelin et al. 1998). The research motivated by the 1982-1983 ENSO event proved that the interactions between forcing mechanisms and ENSO response was more complex than originally thought.

1.3 ENSO Dynamics

The tropical Pacific typically has easterly trade winds which concentrate warm surface waters in the western equatorial Pacific. This thick surface layer of warm water is referred to as the "warm pool". The warm pool tends to generate deep tropical convection which drives the Walker circulation (e.g. Bjerknes 1969; Julian and Chervin 1978). The thermocline, the boundary between warm, well mixed, surface water and cold, deep water, is deep in the western Pacific due to thickness of the warm pool. Due to the easterly trade winds pushing warm surface waters to the west, a "cold tongue" of cooler water forms in the eastern equatorial Pacific. The cold tongue is generated due to equatorial upwelling that brings cool water from below the shallow thermocline to the surface. Figure 1.2 depicts the state of the ocean and atmosphere of the tropical Pacific during neutral conditions.

Early studies identified several mechanisms capable of generating changes in tropical Pacific SST (see Barnett 1977 for a review). These studies suggest weakened trade winds

generate positive SST anomalies through i) increases in the north equatorial counter current, ii) alterations in the local surface heat fluxes, or iii) reductions in equatorial upwelling. Many of these mechanisms generate warm SST anomalies in tropical Pacific and play a role in creating ENSO variability. However, ocean adjustment and wave theory are also necessary for a complete understanding of ENSO behavior (e.g. Godfrey 1975).

Ocean dynamics are critically important in the evolution of ENSO events through coupled air-sea interactions in the tropical Pacific (Neelin et al. 1998), although ENSO-like variability can be simulated without ocean dynamics (Clement et al. 2011). During El Niño conditions (Figure 1.2), sea level pressure (SLP) associated with the Southern Oscillation weaken the trade winds. Once initiated, ENSO conditions support self amplification through the coupled air sea interactions of the Bjerknes feedback mechanism (Bjerkenes 1969). It is well documented that ocean adjustment to relaxed trade winds, or positive zonal wind anomalies along the equator, is highly dependent upon ocean dynamics in which equatorial trapped waves propagate zonally along the thermocline (e.g. Wyrtki 1975; Godfrey 1975; Kessler 1991; Clarke 1992; Neelin et al. 1998; Zebiak and Cane 1987; Battisti 1988; Battisti and Hirst 1989; Schopf and Suarez 1988; Suarez and Schopf 1988; Graham and White 1988; Boulanger and Menkes1999; Sheinbaum 2003). This delayed oscillator theory describes how positive wind anomalies along the equator excite downwelling Kelvin waves which propagate eastward along the thermocline. Downwelling Kelvin waves relax the strong zonal tilt of the thermocline, since they deepen the thermocline in the eastern Pacific, which results in positive SST anomalies. Westerly wind anomalies also excite slow westward propagating Rossby waves. These Rossby waves reflect off the western boundary and propagate eastward as upwelling Kelvin waves. When the upwelling Kelvin waves reach the eastern Pacific, at a time lag behind the downwelling Kelvin waves, they return the thermocline to its neutral position and terminate

the ENSO event.

Additionally it is well documented that three important positive feedback mechanisms for ENSO growth include i) the zonal advective feedback, ii) the upwelling feedback and iii) the thermocline feedback (e.g. Battisti and Hirst 1989; Suarez and Schopf 1988; Jin 1997; Neelin et al. 1998; Dijksta 2006). The zonal advective feedback mechanism acts through positive zonal wind anomalies that advect warm water from the western Pacific toward the east across the mean zonal temperature gradient thus generating positive SST anomalies in the east. These positive SST anomalies further relax the trade winds which strengthens the zonal advection and amplifies the warm SST. The upwelling feedback mechanism operate via a relaxation of the easterly trade winds that in turn reduces wind induced equatorial upwelling. Decreased upwelling reduces the amount of cool water being brought to the surface from below thus generating positive SST anomalies. The associated increase in SST further relaxes the trade winds thus amplifying the existing SST anomalies. Lastly, the thermocline feedback mechanism suggests as easterly trade winds relax the thermocline in the eastern Pacific deepens (through ocean adjustment). The deeper thermocline means that eastern Pacific equatorial upwelling no longer brings cold water from below the thermocline to the surface, but rather warm water from above the thermocline. This generates strong positive SST anomalies in the eastern Pacific, which further relax the trade wind strength.

Cold ENSO (La Niña) events are typically characterized by the opposite patterns of warm ENSO events (Figure 1.2). One exception is that La Niña events are typically weaker in amplitude than El Nino events; particularly when the maximum SST anomalies occur in the eastern Pacific (Larkin and Harrison 2002). Additionally, La Niña events contain different teleconnection patterns and durations (Hoerling et al. 1997; Okumura and Deser 2010). Cold ENSO events occur when SLP variability associated with the

Southern Oscillation increases the strength of the trade winds. Stronger trade winds confine the warm pool to the far western Pacific and generate cold SST anomalies in the eastern Pacific.

Generally ocean adjustment to external forcing, oceanic wave dynamics, and the necessary feedback mechanisms for ENSO growth are well understood and accepted. Our understanding of these mechanisms and their influence on SST allows for some ENSO predictability (Flugel and Chang 1996; Latif et al. 1998; Jin et al. 2008). Currently, ENSO prediction based on statistical and physical model is more skillful that persistence forecasts at lead time of 6-12 months (Latif et al. 1998). However, the prediction skill of coupled models is dependent upon the model ability to simulate the mean state and the skill of the forecast decreases as lead time increases (Jin et al. 2008). Furthermore, the skill of ENSO forecasts initialized in spring are much lower than forecasts initialized later in the year due to the possibility of decaying ENSO events occurring (Jin et al. 2008). One unresolved issue relates to whether ENSO variations are self sustained or stochastically forced. One theory for the underlying mechanism that explains ENSO variability suggests ENSO variability is a self sustained oscillation that contains irregularities due to external forcing or diversity in internal dynamics (Graham and White 1988; Eckert and Latif 1997; Kleeman and Moore 1997; Kleeman and Power 1994; Chen et al. 2004). However, observational evidence does not support regular oscillatory behavior between positive and negative phases and indicates ENSO is an 'event like' disturbance (Kessler 2002). In support of the observational evidence, several studies suggest the tropical Pacific is a linearly stable system in which ENSO is triggered by stochastic forcing (e.g. Penland and Sardeshmukh 1995; Penland 1996; Eckert and Latif 1997; Blanke et al. 1997; Chang et al. 1996; Moore and Kleeman 1999; Zavala-Garay and Moore 2003). However, more work needs to be done in order to explain observed temporal and spatial

diversity of ENSO.

1.4 ENSO Diversity

Observational analysis show individual ENSO events contain large spatial variations in SST anomalies (Ashok et al. 2007; Kug et al. 2009). These analyses led to the recent classification of two types of ENSO events: Central Pacific (CP) and Eastern Pacific (EP) (Kao and Yu 2009; Takahashi et al. 2011). EP events (also referred to as canonical or cold tongue events) are characterized by largest magnitude SST anomalies in the eastern tropical Pacific (Ashok et al. 2007; Kug et al. 2009, 2010a; Kao and Yu 2009; Takahashi et al. 2011)). The maximum magnitude SST anomalies during CP events (also known as ENSO Modoki, or warm pool events) occur in the central tropical Pacific (Ashok et al. 2007; Kug et al. 2009, 2010a; Kao and Yu 2009; Takahashi et al. 2011). Understanding the differences between CP and EP events is crucial as each type appears to have different climate teleconnections (Larkin and Harrison 2005; Capontondi et al. 2015; Kumar et al. 2006; Weng et al. 2007).

Since the maximum positive SST anomalies are in the eastern Pacific during EP events and in the central Pacific during CP events, the location of the deep atmospheric convection is different between the two types of ENSO events. Deep convection in the tropics excites atmospheric Rossby waves, which have large impacts on the mid-latitudes (e.g. Gill 1980; Hoskins and Karoly 1981; Jin and Hoskins 1995). Therefore, a shift in the location of the tropical diabatic forcing associated with the deep convection can have significant global impacts (e.g. Diaz et al. 2001). This shift in diabatic forcing can be seen by the associated change in the location of precipitation for the two types of ENSO events (Figure 1.3; Kao and Yu 2009). In agreement, Ashok et al. (2007) show

CP events significantly influence the Walker circulation by shifting the location of the updraft branch, associated with deep convection, to the central Pacific.

Ashok et al. (2007) specifically discuss the global teleconnections associated with CP ENSO events, which include changes to SLP, upper-level geopotential heights, precipitation, temperature, and surface wind patterns. The effects of CP events may propagate into the mid-latitudes more efficiently during the winter when the jet streams are stronger (Ashok et al. 2007). Additionally, Larkin and Harrison (2005) show that seasonal temperature and precipitation patterns over the United States are vastly different during CP and EP events. For example, the central US experiences wintertime cooling during EP events but warming during CP events (Larkin and Harrison 2005). Although many studies show different global teleconnection patterns during CP and EP events (see Capotondi et al. 2015 for a review), uncertainties exist due to a relatively short observational record and a large variety of CP and EP definitions used.

1.4.1 Defining CP and EP Events

Most studies utilize empirical orthogonal function (EOF) analysis to identify the leading modes of SST variability in the Tropical Pacific to separate and define CP and EP events (e.g. Ashok et al. 2007; Kao and Yu 2009, Yu and Kim 20111; Kim et al. 2012a,b; Takahashi et al. 2011; Vimont et al. 2014). Using observational data, Ashok et al. (2007) defined the EP ENSO event as the first EOF of monthly SST anomalies in the tropical Pacific, while the El Nino Modoki, or CP event, was defined as the second EOF. Figure 1.4 shows the spatial pattern of SST anomalies associated with the leading EOFs. The first mode shows the largest amplitude SST anomalies occur in the eastern Pacific, while the second mode contains the largest amplitude SST anomalies in the central Pacific.

Other observational studies use a combination of regression and EOF analysis to separate and define CP and EP events (Kao and Yu 2009, Yu and Kim 20111; Kim, S.T. et al. 2012b). To define EP (CP) events this method removes the linear regression of SST anomalies onto the Nino4 (Nino1+2) index prior to the EOF calculation. The spatial patterns obtained via the regression-EOF method are very similar to other studies where EP events have large warm SST anomalies in the eastern Pacific and CP events contain maximum positive SST anomalies in the central Pacific.

More recently, Takahashi et al. (2011) suggested idealized EP and CP ENSO events are a linear combination of the leading two EOF patterns of SST variability. This indicates the two ENSO 'types' are not distinct but describe the nonlinear evolution of ENSO. By defining ENSO diversity via a combination of the leading modes of SST variability, this method suggests any individual ENSO event can project onto both EP and CP patterns. In other words, any given ENSO event can have characteristics of both CP and EP events in various amounts (Kug et al. 2009; Takahashi et al. 2011; Vimont et al. 2014). Takahashi et al. (2011) defined the EP Index as $(PC1 - PC2)/\sqrt{2}$ and the CP Index as $(PC1 + PC2)/\sqrt{2}$. The SST spatial patterns of the EP and CP ENSO events obtained via Takahashi et al. (2011) are shown in Figure 1.5. The EP and CP Index, as defined by Takahashi et al. (2011), is simply a rotation of the principal component coordinate system and how individual ENSO events project onto both patterns of variability. Vimont et al. (2014) use this method to define CP and EP events when calculating the optimal initial conditions and growth patterns of each ENSO type.

1.4.2 Spatial Structures and Temporal Evolution of CP and EP events

Many studies use lagged correlation and regression analyses to compare and contrast the physical structures of SST and subsurface temperature anomalies of CP and EP ENSO events (Ashok et al. 2007; Kao and Yu 2009; Kim et al. 2012b). Studies using both observations and model simulations support EP events evolve as thus: SST anomalies first appear in the eastern Pacific, near the coast of South America and amplify and expand westward into the Pacific until the peak of the ENSO event, after which the SST anomalies begin to decay (Kao and Yu 2009, Kim et al. 2012b).

CP events, however, are characterized by SST anomalies beginning, amplifying, and decaying in the central Pacific. SST evolution during CP events shows no propagation as in EP events, but appears as a standing mode (Ashok 2007; Kao and Yu 2009; Kim, S.T. et al. 2012a,b). Results from a fully coupled climate model supports the observed spatial pattern of CP events, however, the magnitude of the simulated events is much too weak (Kim et al. 2012b). This indicates the model may capture the correct forcing mechanism of CP events but the wrong intensity or efficiency. The anomalous SST pattern between 6 and 12 months prior to the peak magnitude of CP events corresponds to the structure of the Pacific Meridional Mode (PMM) (Kim et al. 2012b; Vimont et al. 2014; Capotondi et al. 2015).

Comparisons of the subsurface temperature structure between EP and CP event in observations and model simulations indicate EP and CP events develop through different mechanisms (e.g. Newman et al. 2011a; Fedorov et al. 2015; Capotondi and Sardeshmukh 2015; Capotondi et al. 2015; Lopez and Kirtman 2013; Hu et al. 2014; Karnauskas 2013; Vimont et al. 2014). The propagation of subsurface temperature anomalies along the

thermocline during EP events indicates these events are primarily driven by thermocline variability and equatorial wave propagation (Kao and Yu 2009; Kim et al. 2012b). CP ENSO subsurface temperature structures are characterized by stationary temperature anomalies above the thermocline depth amplifying and decaying in the central Pacific (Kao and Yu 2009; Kim et al. 2012a,b). Furthermore, studies have investigated the linearity of positive and negative phases of CP and EP ENSO events. Kao and Yu (2009) show EP events have larger magnitude warm events, or are positively skewed, while CP events have larger magnitude cold events, or are negatively skewed.

1.4.3 Mechanisms for Generating ENSO diversity

While any given ENSO event can contain characteristics of both CP and EP events, the mechanisms influencing the generation of the two types of events differ (e.g. Kug et al. 2009; Takahashi et al. 2011; Vimont et al. 2014; Meinen and McPhaden 2000; Horii et al. 2012). Capotondi and Sardeshmukh (2015) show both SST precursors and the thermocline initial state are critical to the capture the development of CP and EP spatial characteristics. However, CP events, which contain maximum SST anomalies in the central Pacific where the thermocline is deep, may be less influenced by thermocline feedbacks and more influenced by zonal advective feedbacks (Kao and Yu 2009; Lopez and Kirtman 2013). CP events also appear to be heavily influenced by extratropical atmospheric forcing (Yeh et al. 2009; Kim et al. 2012b; Yu and Kim 2011; Furtado et al. 2012). EP events, on the other hand, contain peak amplitude SST anomalies in the east Pacific where the thermocline is shallow. Due to the shallow thermocline depth, EP events are highly influenced by thermocline feedbacks (e.g. Battisti 1988).

To identify the extratropical interactions of EP and CP events, Yu and Kim (2011) applied a lead-lag correlation analysis of the dominant modes of extratropical SLP variability to

the EP and CP indices. The first mode of extratropical SLP variability, or first principal component (PC1), corresponds to the Aleutian low and lags both EP and CP events. The second mode of extratropical SLP variability, corresponds to the North Pacific Oscillation (NPO; Rogers 1981; Linkin and Nigam 2008) and lags EP events but leads CP events.

The NPO appears to be an extra tropical forcing mechanism important to the generation of ENSO variability, and CP events in particular (Vimont et al. 2001, 2003a,b; Alexander et al. 2010; Vimont et al. 2009; Vimont 2010; Pegion and Alexander 2013; Thomas and Vimont 2016; Chang et al. 2007; Alexander et al. 2010; Yu and Kim 2011; Kim et al. 2012b; Park et al. 2013; Kao and Yu 2009). Other studies highlight the significance of the PMM SST structure in the development of ENSO events (Kim et al. 2012b; Ma et al. 2017). More specifically, the PMM structure is part of the optimal initial condition that maximizes CP ENSO growth (Vimont et al. 2014, Capotondi and Sardeshmukh 2015). Additionally, other studies suggest CP events are more heavily influenced by atmospheric forcing than thermocline variations (Yeh et al. 2009; Kim et al. 2012a).

Recently, You and Furtado (2017) identified an important EP precursor containing a southern hemisphere dipole structure in SLP during austral fall (MAM) and spring (SON) they title the "South Pacific Oscillation" (SPO). Similar SLP patterns are also found in Penland and Matrosova (2008). It it possible the SPO patterns are associated with a SST pattern referred to as the south Pacific Meridional Mode (SPMM; Zhang et al. 2014). Min et al. (2017) also relate the SPMM to SST anomalies in the eastern Pacific which may have EP ENSO implications. Furthermore, EP events with strong EP characteristics, such as the 1997/1998 El Niño event, have been linked to the occurrence of westerly wind busts (WWBs) in the western tropical Pacific (Boulanger and Menkes 1999; McPhaden 1999; Harrison and Chiodi 2009; Federov et al. 2015; Chen et al. 2015).

Further characterization of the underlying processes that distinguish the generation of CP from EP events will ultimately improve our ability to predict the spatial characteristics of ENSO events with greater lead times. This will provide increased time for society prepare for resulting climatic impacts. The skill of such predictions depends on improving our knowledge of the complicated interactions between the processes that influence the initiation and development of different ENSO events.

1.4.4 ENSO Diversity, Climate Change, and Natural Variability

It is important to understand the rate of occurrence of CP and EP events since they have significantly different initiation mechanisms and global teleconnections. Observational analysis suggests that CP events have increased in frequency during recent decades (Ashok et al. 2007). Ashok et al. (2007) suggest the apparent increase in CP frequency may be due to a change in the background state of the present climate, although, more evidence is required. Specifically, they suggest the increased frequency of CP events is due to weakened trade winds, which in turn decreases the zonal sea surface temperature gradient and a flattening of the thermocline (Ashok et al. 2007). An ensemble of eleven CMIP3 models using projected climate scenarios, the Special Report for Emission Scenario A1B projection (SRESA1B), also attributes the apparent increase in CP ENSO events to a change in the background state of the climate due to anthropogenic climate change (Yeh et al. 2009). Yeh et al. (2009) show this increase in frequency, in agreement with Ashok et al. (2007), may be due to a zonal flattening of the thermocline structure due to changes in the trade winds. However, Hu et al. (2012) find increased thermocline tilt in recent decades. They argue the results of Ashok et al. (2007) may be due a sampling issue and show interdecadal variability in the thermocline rather than the response to a trend in climate change (Hu et al. 2012).

Although there is evidence that ENSO diversity is influenced by anthropogenic climate change several studies show the apparent increase in frequency of CP events may be fully explained by natural variability (Newman et al. 2011b; Kim et al. 2012a). Newman et al. (2011b) identify multivariate red noise patterns from observations using linear inverse modeling techniques. Then, through spectral analysis, they illustrate that the red noise matches the variability of CP and EP events. Furthermore, the variations of CP and EP events can be reproduced using multivariate red noise and the observed frequency of CP and EP events is less than expected due to natural variability (Newman et al. 2011b). These results indicate the observational record of CP and EP events is not long enough to significantly attribute observed trends to external forcing or climate change.

Furthermore, Kim et al. (2012a) used cyclostationary-EOF analysis to analyze the frequency of CP and EP events. They identify the leading EOF modes of tropical SST and determine CP and EP events can be described as combinations of theses two modes. Central Pacific events occur when the two modes are 'in phase', while EP events occur when the two modes 'out of phase'. The authors then analyze the phase relationship between the two leading SST modes within the observational record and determine that, although the modes have been 'in phase' in recent years, the observational record is too short to attribute observed changes in the CP frequency to climate change. To compensate for the inadequate observational record, the fully coupled Geophysical Fluid Dynamics Laboratory (GFDL) model is used. The model simulates both CP and EP events well and shows the phase relationship between the two leading SST modes, and thus the frequency change of CP events, can be explained by natural variability. Our understanding of the relationship between climate change and ENSO diversity is compromised by the limited historical sample size. Therefore, the use of dynamical models is critical to address the gaps in knowledge about what causes ENSO diversity.

1.5 Physical vs Statistical Dynamical Models

Scientists use many different techniques to study the complex behaviors of ENSO variability. Techniques include the use of observations as well as dynamical models. Two commonly used types of dynamical models used are physical models and statistical models. Coupled physical climate models are ideal for testing mechanisms between previously identified dynamical structures. However, due to the sensitivity of ENSO variability to model biases and the lack of observations, it can be difficult to recreate and identify realistically representative relationships in physical models. Conversely, Statistical dynamical models are observationally based and, therefore, ideal for identifying observationally grounded dynamical connections. Unfortunately, it is difficult to determine if the connections identified have a physical basis using statistical models alone.

Since each type of dynamical model (physical and statistical) contains complimentary strengths and weaknesses, experiments that utilize both types of models will ensure the results are both observationally grounded as well as physically realistic. The research presented in this dissertation uses both empirical statistical dynamical models and physical climate models in order to identify structures influencing ENSO development and test the physical mechanisms responsible for the connection.

1.6 Overarching Framework

ENSO initiation is complicated by a multitude of interrelated processes that influence tropical Pacific variability, such as extra-tropical atmospheric variability, stochastic forcing, and thermocline dynamics. Isolating the interactions between these processes and ENSO development is a non-trivial, yet necessary, challenge to improve our understanding of ENSO initiation and predictability skill. This research will 1) further characterize the

interactions between the extra-tropical forcing and ENSO, 2) identify the role of stochastic forcing on the development of CP and EP events, and 3) determine the physical mechanisms connecting noise forcing structures to subsequent ENSO development.

Project 1) We identify the specific mechanisms that excite ENSO events due to extra-tropical atmospheric forcing through the use of an ensemble of physical model experiments. This study is performed in the forward sense where the initial state, dynamics, and the forcing of the system are specified first. Then, the model is run forward in time to estimate the response of the system to the external forcing. Using a combination of two physical climate models we isolate interrelated processes that operate in tandem in the Tropical Pacific. This framework allows us to determine the mechanisms through which ENSO growth due to extra-tropical atmospheric forcing occurs.

Project 2) Statistical dynamical modeling identifies observationally-grounded noise forcing patterns that generate CP or EP growth. From some set of initial conditions, predictable ENSO growth occurs via deterministic dynamics. A specific set of initial conditions will maximize this growth, referred to as optimal initial conditions. Noise forcing influences the deterministic evolution of ENSO in three possible ways: i) it may contribute to the ENSO growth, ii) create error or perturb the state away from the what expected via the deterministic dynamics, or possibly iii) have no effect on the evolution of the state. In this deterministic dynamics vs noise forcing framework, noise forcing is also responsible for creating the optimal initial conditions that maximize CP or EP growth. This study is performed in the backwards sense where we first calculate the deterministic growth of CP and EP events from Tropical Pacific observations. We then estimate the rapidly varying noise forcing that generates the optimal initial conditions that maximize CP and EP deterministic growth.

Project 3) Finally, physical model experiments characterize the physical mechanisms that connect the previously identified noise forcing structures and ENSO development. This study is, again, performed in the forward sense where the initial state, dynamics, and forcing of the system are specified first. The model is then run forward in time to determine the response to applied forcing. Physical model experiments allow us to identify the mechanisms of how the noise forcing generates ENSO events.

1.6.1 Scientific Questions

Specifically, this research will answer the following scientific questions:

1: What are the physical mechanisms that excite ENSO events due to extra-tropical atmospheric forcing ?

2: What structures within the rapidly varying noise forcing generates the optimal initial conditions that maximize growth toward CP or EP ENSO characteristics thus leading to ENSO diversity?

3: What physical mechanisms allow the noise forcing to build into CP and EP ENSO events?

In an effort to answer these scientific questions we use a combination of physical and statistical model experiments. Chapter 2 uses physical model experiments in order to determine the physical mechanisms that excite ENSO events due to extra-tropical atmospheric forcing. Chapters 3 presents a new methodology in which we utilize a statistical model to identify stochastic noise patterns that contribute to EP and CP ENSO growth. Chapter 4 shows an application of this statistical methodology by analyzing the relative roles of deterministic dynamics and noise forcing during several past ENSO events.

Chapter 5 presents the noise forcing structures that maximize CP and EP growth within the National Center for Atmospheric Research (NCAR) Community Earth System Model (CESM). Chapter 6 presents a series of physical model experiments to analyze the physical mechanisms through which noise forcing structures generate ENSO diversity within the CESM.

1.7 Copyrights

The information contained in several of the following chapters represent manuscripts that have been published (Chapter 2) or are currently undergoing the peer-review process (Chapters 3 and 4). The information contained in the remaining chapters (Chapters 5 and 6) are being prepared for submission. Since the published articles are being reproduced for educational purposes, I am required to acknowledge current copyrights.

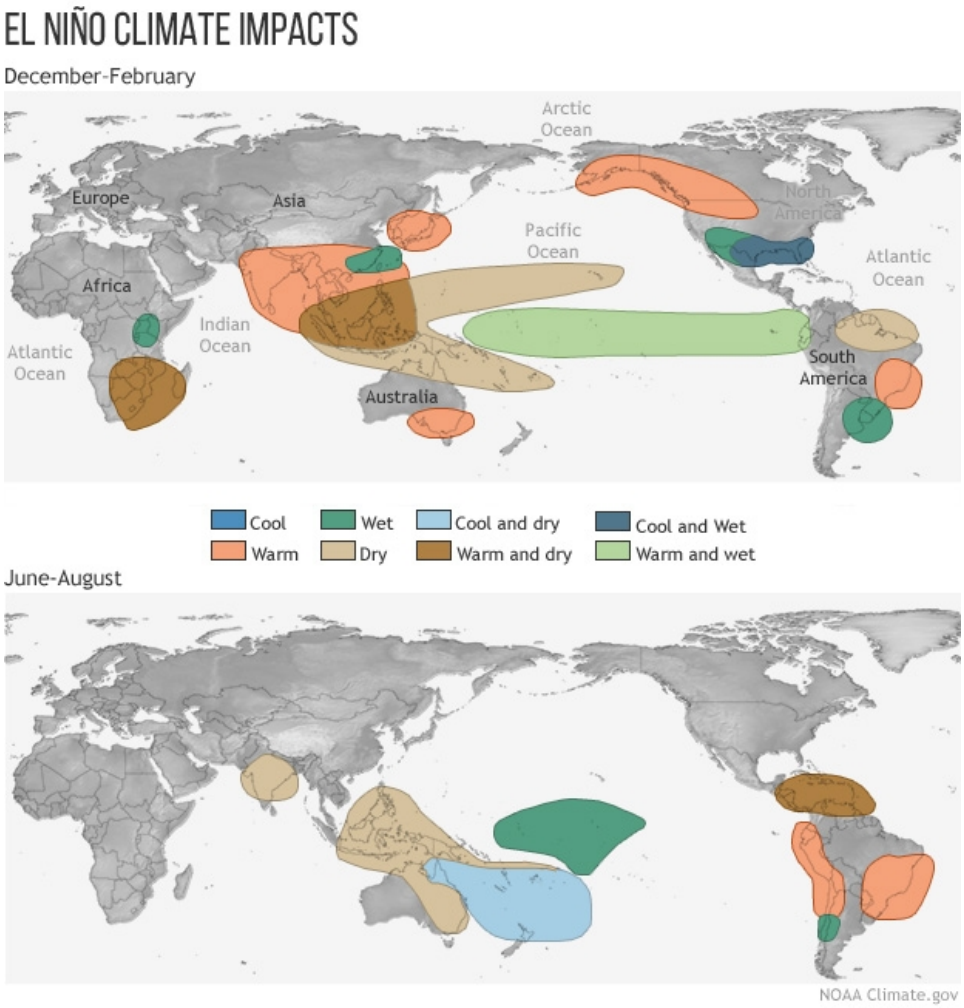

FIGURE 1.1: Typical winter and summer El Niño climate impacts. Figure courtesy of pmel.noaa.gov.

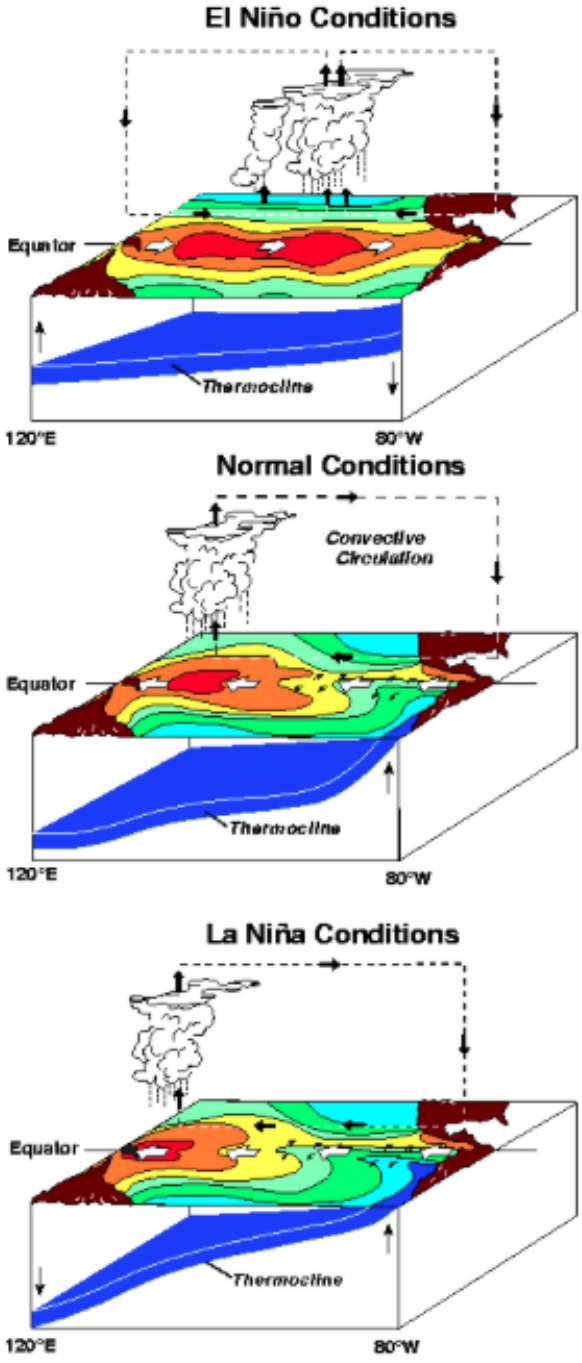

FIGURE 1.2: Typical atmospheric and ocean conditions in the tropical Pacific during neutral, El Niño and La Niña states. Figure courtesy of pmel.noaa.gov.

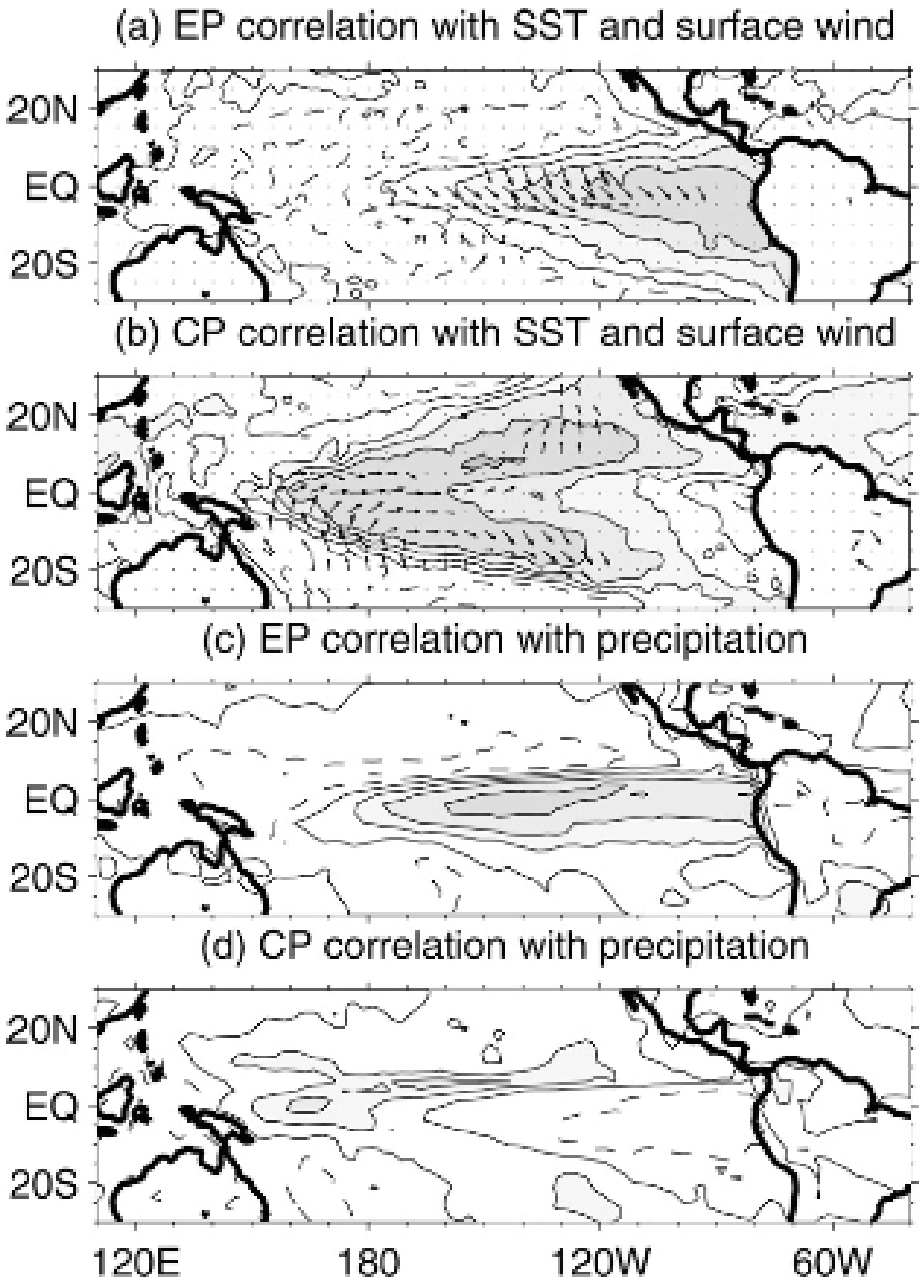

FIGURE 1.3: Correlation coefficients between the principal components of the EP- and CP-EOFs and surface wind, SST, and precipitation anomalies. (a), (c) The correlations with the EP-EOF; (b), (d) the correlations with the CP-EOF. In (a) and (b) the correlations with the surface wind anomalies are shown as vectors and contours show the correlations with the SST anomaies; correlations with the precipitation anomalies are shown in (c) and (d). Contour intervals are 0.3 for all panels; dashed lines denote negative values. Highlighted vectors indicate the correlation coefficients pass the 95% significance level estimated by a two-tailed t test. Figure 9 in Kao and Yu 2009.

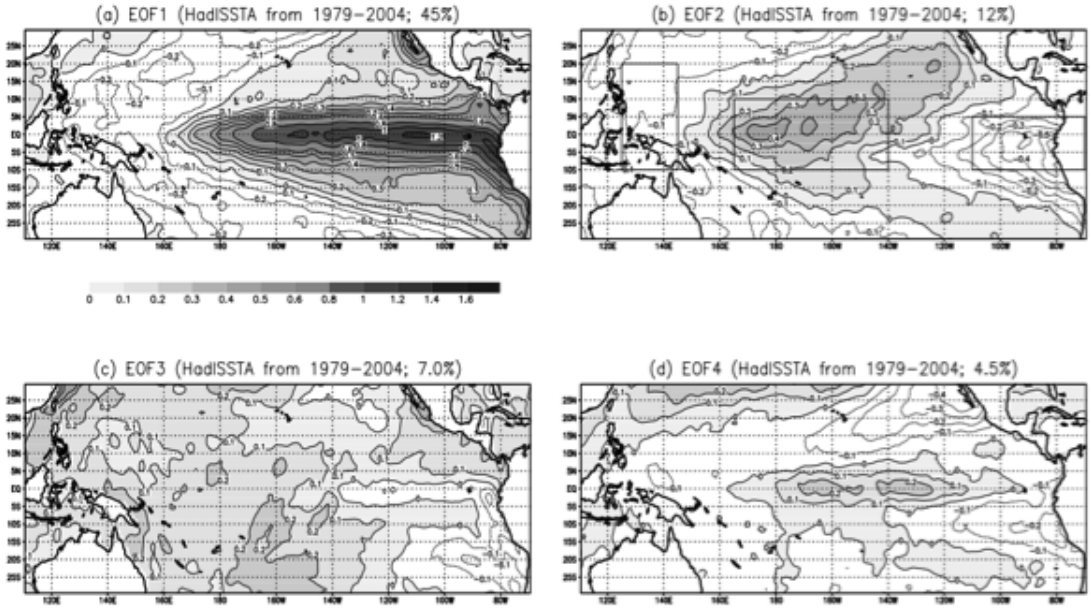

FIGURE 1.4: The first four EOF modes of tropical Pacific SST anomalies (1979-2004) multiplied by respoective standard deviations of the principal components. Units in °C. Figure 2 in Ashok et al. 2007.

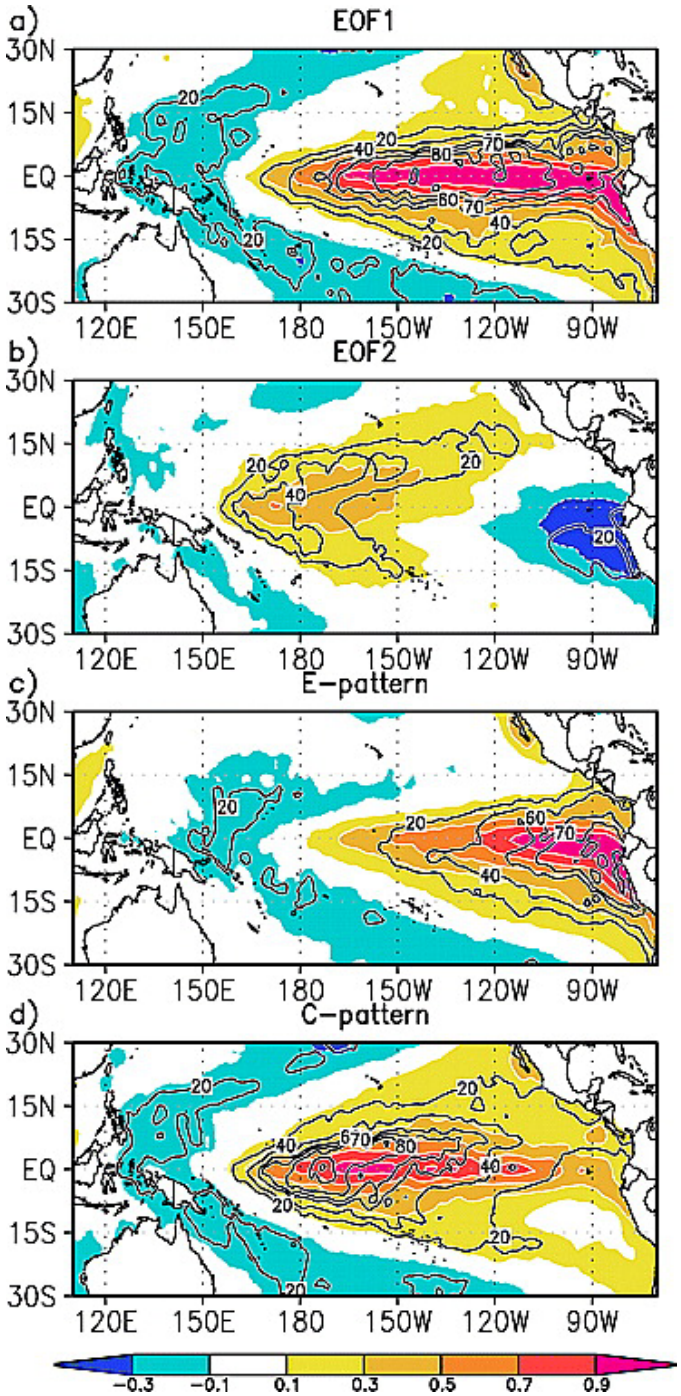

FIGURE 1.5: Linear regression coefficients (°C, shading) between 1870-2010 HadISST SST and EP and CP indices. Figure 3 in Takahashi et al. 2011.

Chapter 2

Modeling the mechanisms of linear and nonlinear ENSO responses to the Pacific Meridional Mode

The content of this chapter has been published the *Journal of Climate* as Thomas, E. E., and D. J. Vimont, 2016: Modeling the mechanisms of linear and non-linear ENSO responses to the Pacific Meridional Mode.

2.1 Introduction

The dominant mode of variability in the tropical Pacific is the El Niño - Southern Oscillation (ENSO; Wallace et al. 1998) phenomenon. While all ENSO events evolve differently, warm ENSO (El Niño) events are generally characterized by warm sea surface temperature (SST) anomalies in the central and eastern Pacific, a reduction in the climatological

zonal trade wind strength in the central tropical Pacific, and a deepening of the thermocline in the central and eastern tropical Pacific (McPhaden et al., 1998, Rasmusson and Carpenter, 1982, Wallace et al., 1998). Although cold ENSO (La Niña) events are generally characterized by the opposite structure, warm and cold ENSO events are not symmetric opposites[1]. In particular, cold ENSO events tend to be weaker in amplitude overall, and tend to have relatively larger amplitude in the central Pacific compared to the eastern Pacific (Larkin and Harrison, 2002). It is generally thought that ocean dynamics play a critical role in the evolution of ENSO events through their role in coupled ocean-atmosphere interactions in the tropical Pacific (Neelin et al., 1998), though variability with ENSO-like characteristics can be simulated without ocean dynamics (Clement et al., 2011).

The second-most dominant statistical mode of coupled ocean-atmosphere variability in the tropical Pacific is the Pacific Meridional Mode (PMM; Chiang and Vimont 2004). The positive phase of the PMM is characterized by a northward meridional SST gradient around the location of the climatological Inter-Tropical Convergence Zone (ITCZ), a corresponding northward shift of the climatological ITCZ, and meridional winds that blow toward warmer water (the negative phase contains the opposite structure). Unlike ENSO, the PMM does not require ocean dynamics for its existence and instead evolves via a positive feedback between wind-induced evaporation and SST – the so-called WES feedback (Chang et al., 1997, Vimont, 2010, Xie and Philander, 1994). In short, positive SST anomalies drive an atmospheric circulation that includes a reduction in the climatological trade wind strength, which reduces the climatological evaporative heat flux over the original positive SST anomalies.

[1]Here and throughout the manuscript, we use the phrase "symmetric" or "asymmetric" to describe the extent to which warm and cold ENSO structures are polar opposites (symmetric), or exhibit differences in amplitude or structure (asymmetric).

It has been shown that the PMM and ENSO are related through the so-called "seasonal footprinting mechanism" (SFM) (Alexander et al., 2010, Chang et al., 2007, Park et al., 2013, Vimont et al., 2003a). The SFM operates as follows: mid-latitude atmospheric variability associated with the atmospheric North Pacific Oscillation (NPO) (Linkin and Nigam, 2008, Rogers, 1981) generates positive SST anomalies in the eastern subtropical Pacific through a relaxation of the climatological trade winds. These SST anomalies have a strong projection on the spatial structure of the PMM. The SST anomalies persist beyond the time scale of NPO variations, and subsequently propagate equatorward and westward via air-sea feedbacks (Liu and Xie, 1994, Vimont, 2010, Vimont et al., 2009) in a manner very similar to the PMM. The SST anomalies generate an atmospheric circulation that can lead to the development of an ENSO event during the ensuing months (Alexander et al., 2010, Chang et al., 2007, Vimont et al., 2003a,b). While there is some discussion in the literature about the equivalence of the SFM and the PMM, for the purposes of this paper we assume that the two are intimately related, as the dynamical processes that govern PMM evolution provide the conduit by which mid-latitude atmospheric variability can impact ENSO through the SFM.

Despite evidence for the PMM's influence on ENSO, the specific mechanisms that link the PMM to ENSO are not clear. Observational (Vimont et al., 2003a) and model (Alexander et al., 2010, Vimont et al., 2003b) analyses suggest that the link occurs through the direct forcing of equatorial Kelvin waves by wind stress anomalies associated with the PMM, which lead to a deepening of the thermocline in the eastern Pacific. In a different view, recent studies suggest that changes in the trade winds induce heat content anomalies in the equatorial region which lead to ENSO variation through "trade-wind charging" (Anderson and Perez, 2015, Anderson et al., 2013) or through a "discharge-recharge" paradigm (Anderson and Maloney, 2006, Jin, 1997). Specifics of how the PMM interacts

with ENSO are important due to the seasonal timing of the PMM and the seasonality of the ENSO growth rate. The PMM's influence on ENSO is likely to be most prominent if that influence occurs at a time when ENSO growth rates are largest [the seasonal ENSO growth rate is related to a potential instability due to equatorial upwelling in regions of vertical thermocline perturbations (Battisti, 1988)]. This possibility, though, has not been explored.

Many recent studies have documented the role of the extra-tropics on the spatial characteristics of ENSO since two types of ENSO events have been defined. This may have large implications on global climate since these ENSO events, termed Central Pacific (CP) and Eastern Pacific (EP), produce significantly different teleconnection patterns and climatic impacts (Ashok et al., 2007, Kao and Yu, 2009, Kumar et al., 2006, Larkin and Harrison, 2005, Weng et al., 2007, 2009). While any individual ENSO event may contain characteristics of both types of event (Kug et al., 2009, Takahashi et al., 2011, Vimont et al., 2014), extra-tropical atmospheric forcing, such as the NPO, has been suggested to influence the development of CP ENSO events (Alexander et al., 2010, Kim et al., 2012a, Vimont et al., 2014, Yu and Kim, 2011). Additionally, Lin et al. (2014) show the PMM is important to the generation of CP ENSO events through the SFM, although preexisting thermocline conditions may influence this relationship (Capotondi and Sardeshmukh, 2015). Despite the connection between the PMM and CP ENSO events, the main goal of this study is not to directly simulate the PMM's role in ENSO diversity, but rather to better understand mechanisms by which the PMM interacts with ENSO variability in general.

Identifying the specific processes and mechanisms through which extra-tropical atmospheric forcing, especially the NPO, influences the development of ENSO events requires further attention. Understanding the interactions between the PMM that contribute to

the evolution of ENSO events can guide predictability studies of ENSO events. For example, Larson and Kirtman (2014) show the PMM is an important precursor to ENSO although it is not, yet, a reliable predictor. In this study we use a combination of two models containing complementary sets of physics in order to separate and characterize the interactions between the extra-tropics and ENSO development. The National Center for Atmospheric Research (NCAR) Community Earth System Model (CESM) in "slab ocean" configuration contains the necessary air-sea interactions to generate a response representative of the PMM to a surface heat flux associated with the North Pacific Oscillation, but is unable to fully simulate ENSO due to the lack of ocean dynamics. An intermediate coupled model (hereafter referred to as the ICM) (Battisti, 1988), which contains the necessary ocean dynamics to simulate ENSO variability but not the PMM (due to the lack of wind-induced evaporation), is used to simulate the ENSO response to the atmospheric forcing generated by CESM. It is important to note the ICM used is unable to simulate ENSO diversity with respect to CP and EP events, which is a caveat for this study. However, here we are interested in using the ICM to isolate the mechanisms by which PMM variability influences ENSO-like variability in general. The thermodynamic air-sea interactions contained in CESM and the ocean dynamics in the intermediate coupled model cleanly separate the two primary mechanisms responsible for linking PMM and ENSO events, allowing us to identify the different processes responsible for the simulated ENSO response.

This chapter is organized as follows. The CESM model description, NPO forcing, and PMM response to the NPO forcing are described in section 2. Section 3 describes the ICM and presents the ENSO response of the ICM to the PMM atmospheric forcing (generated by the CESM). Section 4 identifies the non-linear sources generating asymmetry between warm and cold ENSO responses, and section 5 summarizes and discusses the results.

2.2 CESM1.2

The PMM response to the NPO forcing is simulated using the National Center for Atmospheric Research Community Earth System Model. This study simulates the PMM as opposed to using the observed PMM in order to cleanly isolate PMM dynamics from ENSO dynamics. Isolating the PMM from ENSO is difficult in the observed record since the PMM evolution is linked to the subsequent evolution of ENSO, and hence lagged inferences about the PMM evolution would be "contaminated" by ENSO mechanisms such as the Bjerknes feedback and thermocline influences. This section describes the experimental setup, NPO heat flux forcing and PMM response to the NPO forcing.

2.2.1 Model Description and Experimental Setup

Experiments utilizing the NCAR CESM are performed to determine the response from a surface heat flux forcing associated with the NPO. The model is run with approximately a 2°x2° horizontal grid (f19_g16 resolution), 30 layer vertical resolution, Community Atmosphere Model version 5 (CAM5) physics, prescribed modal aerosols, and coupled to a slab ocean model (SOM). This configuration contains the ocean-atmosphere thermodynamic coupling necessary to simulate PMM variability through the SFM (Vimont et al., 2001), however, the SOM is unable to simulate ENSO variability since it contains no ocean dynamics. The SOM calculates the change in mixed layer temperature as:

$$\rho c_p h_{mix} \frac{dT_{mix}}{dt} = F_{net} - Q_{flx}, \tag{2.1}$$

where ρ is the density of ocean water, c_p is the specific heat, h_{mix} is the depth of the mixed layer, T_{mix} is the temperature of the mixed layer (assumed to be the same as the

surface temperature), F_{net} is the net surface heat flux, and Q_{flx} is a prescribed seasonally varying term that represents the horizontal and vertical oceanic heat flux divergence in the mixed layer column.

We repeat the model experiments that were performed in Vimont et al. (2009) (hereafter referred to as VAF2009) in which the CESM is forced by surface heat flux anomalies associated with the NPO (described below), except that here the observed NPO heat flux and an updated version of the atmospheric model (CAM5) are used. Results are only briefly described here; for further analysis, see Vimont et al. (2009).

The NPO net surface heat flux anomalies are calculated as follows. Empirical orthogonal function (EOF) analysis is applied to intraseasonal sea level pressure (SLP) anomalies in the North Pacific (20°N-90°N, 110°E-70°W) using the NCEP reanalysis between 1948-2002. The intraseasonal filter is constructed by removing the boreal winter (NDJFM) mean for each year from the corresponding monthly values during that year, effectively removing interannual variability. The intraseasonal filter is applied so that the calculation of the net surface heat flux associated with the NPO will be less influenced by the resulting change in SST. Since the change in SST will be calculated directly by the model, it should not be incorporated into the externally applied heat flux forcing. The NPO is defined as the second EOF of boreal winter (NDJFM) intraseasonal sea level pressure anomalies. The NPO is defined using NCEP reanalysis data since the 2nd EOF of a long control CESM simulation (with climatological SST) does not represent the NPO pattern well (not shown). The NPO surface heat flux is estimated by regressing the intra-seasonally filtered net surface heat flux (calculated from NCEP reanalysis) onto the standardized second principal component of SLP. We define the positive phase of the NPO (+NPO) as positive SLP anomalies over Alaska and the North Pacific and negative SLP anomalies over the subtropical Pacific. Figure 2.1 shows the sea level pressure and net surface heat

flux associated with the +NPO. The negative phase of the NPO (–NPO) is simply the opposite polarity. Positive heat flux is defined as downwards into the ocean. We note that the positive and negative phases of the NPO may not be linear opposites; we do not incorporate that source of nonlinearity into this study, as our intent is simply to use the NPO to excite the PMM.

A 50-year control simulation, and two sets of experiments each containing an ensemble of 40 branch simulations, are run. Each of the 40 ensemble members in the branch simulation experiments is initialized from an October 1st initial condition that is taken from each of the final 40 years of the control simulation (the first 10 years are discarded as a model spin-up period) and run for 20 months. The first 40 member ensemble is forced with the net surface heat flux associated with the positive phase of the NPO (Figure 2.1), while the second set of ensemble simulations are forced with the net surface heat flux associated with the negative phase of the NPO (Figure 2.1, opposite polarity). A one standard deviation anomaly of NPO heat flux forcing is applied to the SOM in boreal winter (November-March) by adding it as an extra term to (Equation 2.1). The forcing is set to zero in April, and the model continues to evolve (unforced) for the remainder of the 20-month simulation. Due to the linear temporal interpolation of mid-month boundary conditions to the higher temporal resolution required by the model time step, the applied NPO forcing starts increasing in mid October, reaches full strength by mid November, then linearly decreases from full strength to zero between mid-March and mid-April.

2.2.2 CESM Response to NPO Heat Flux Forcing

The seasonal progression of the ensemble-mean low-level wind and sea surface temperature response of the CESM to positive and negative NPO forcing is shown in Figure 2.2 (left and right columns, respectively), and largely matches the results found in VAF2009.

The +NPO forcing generates an anomalously warm SST structure extending southwestwards from the eastern subtropical Pacific towards the central tropical Pacific. This SST structure, characteristic of the PMM, propagates further into the tropics and reaches its peak magnitude during the boreal spring (MAM) following the wintertime NPO forcing.

To show the relative timing of the ensemble-mean PMM response to the NPO forcing, we plot the time evolution of the applied NPO forcing and ensemble-mean PMM index (normalized by their peak amplitudes) in Figure 2.3. The NPO index shows the constant forcing applied to the CESM during boreal winter (NDJFM). Linear ramp-up and ramp-down of the forcing are evident from Oct-Nov and Mar-Apr, respectively. The PMM index is calculated by projecting the SST pattern simulated by the CESM onto the spatial pattern of the PMM [defined by applying Maximum Covariance Analysis to non-ENSO tropical SST and 10m winds over the time period 1950-2005; see Chiang and Vimont (2004) for details]. The resulting ensemble-mean time series in Figure 2.3 is normalized by its maximum amplitude. The simulated PMM SST time series peaks in April (year1) immediately after the NPO forcing is shut off, consistent with a simple integration of the applied forcing. We note the simulated wind time series peaks around the same time or slightly later than the SST response.

Due to thermodynamic coupling, the PMM SST anomalies persist into late summer/fall (JJA-SON), long after the NPO forcing has been removed (Figure 2.2e-j). They slowly decay through the following winter (DJF). As in VAF2009, westerly wind anomalies in the western and central tropical Pacific are generated during the boreal summer (JJA) and fall (SON) due to the persistent warm SST anomalies (Figure 2.2e,g). The –NPO forcing generates a wind response that is approximately a symmetric opposite to the +NPO simulation. Cold SST anomalies extend southwestward from the eastern subtropical Pacific and propagate into the tropics through spring (MAM), where they persist into

the summer/fall (JJA-SON). The cold SST anomalies in the tropics initiate easterly wind anomalies in the western and central tropical Pacific during summer (JJA) and fall (SON). The asymmetry of the ensemble mean CESM response to positive and negative NPO heat flux was investigated and was found to be small compared to the symmetric response (results not shown). The symmetry of the atmospheric response will be addressed in the context of ENSO variability Section 2.3.2.

In the slab ocean model the evolution of SST can only be influenced by changes in the surface heat flux (Equation 2.1), which also largely matches the response found in VAF2009. Here, we only compare the response to the +NPO forcing results to the results obtained by VAF2009 since the response to the –NPO is largely the opposite sign. The CESM shows a decrease in downwelling shortwave radiation and an increase in precipitation in the western and central tropical Pacific during the spring (MAM) following the positive NPO forcing. The response during the summer (JJA) is similar, though shifted slightly northward. The latent heat flux response to the +NPO, similar to the results in VAF2009, shows decreased upwards surface latent heat fluxes in the western tropical Pacific that expand to the central Pacific subtropics through the summer, while increased upwards latent heat fluxes are located in the eastern subtropical Pacific during boreal spring and summer. These results are not shown due to the similarity with the results from VAF2009 (see Fig. 4 in VAF2009).

2.3 Intermediate Coupled Model

The PMM wind anomalies from the CESM simulations, as described in the previous section, are used as an external forcing to an intermediate coupled model that contains the necessary physics to simulate ENSO, but not PMM variations. In this section, we present the results from the ICM experiments.

2.3.1 Model Description and Experimental Setup

The ICM used in this study is the Battisti (1988) version of the Zebiak and Cane (1987) intermediate coupled model. Realistic changes were made to three key model parameters (Thompson and Battisti, 2001): the model's ocean damping rate (changed from 2.5 yr^{-1} to 1 yr^{-1}), the surface drag coefficient (changed from 3.2x10^{-3} to 2.0x10^{-3}), and Rossby wave reflection efficiency (reduced from 100% to 80%). The primary result of these parameter alterations is to produce a linearly stable ENSO regime in which the model requires external forcing to generate ENSO variability.

The ICM simulates the ENSO response to the PMM atmospheric forcing (as described in the previous section). This ICM contains the necessary ocean dynamics to simulate ENSO variability but does not contain the necessary air-sea thermodynamic interaction (i.e. the WES feedback mechanism) needed to simulate the PMM. The two-layer atmosphere is governed by linear shallow water equations on a beta plane and is forced by atmospheric heating anomalies that result from wind convergence and evaporation from SST anomalies (Battisti, 1988, Gill, 1980, Zebiak and Cane, 1987). The rectangular, reduced gravity ocean model (30°N:30°S, 124°E:80°W) contains an upper layer governed by linear shallow water wave dynamics and a motionless deep layer. The upper layer includes a fixed depth (50m) surface mixed layer that determines SST through a temperature tendency equation (Battisti, 1988). The fully coupled ICM internally calculates the anomalous pseudo-wind stress vector on the ocean due to external forcing and coupling as follows:

$$\tau = \mathbf{u_t}|\mathbf{u_t}| - \mathbf{u_m}|\mathbf{u_m}|, \tag{2.2}$$

where $|\mathbf{u}|$ is the amplitude of the wind vector $\mathbf{u}$, and the total wind $\mathbf{u_t}$ is the sum of

the mean wind ($\mathbf{u_m}$; this includes the annual cycle), an externally applied wind forcing if applicable ($\mathbf{u_f}$), and the internal ICM coupled response ($\mathbf{u_c}$):

$$\mathbf{u_t} = \mathbf{u_m} + \mathbf{u_f} + \mathbf{u_c}. \tag{2.3}$$

To determine the ENSO response to the PMM, we force the ICM with CESM-simulated wind response to the NPO forcing. The full 20-months (October through May) of CESM-simulated wind anomalies, which capture the growth and decay of the PMM, are applied to the ICM to determine the ENSO response to a realistic PMM pattern and evolution. We apply the CESM forcing ($\mathbf{u_f}$) as either the anomalous ensemble-mean wind (as in Figure 2.2), or as each of the 40 individual ensemble member wind anomalies from both the +NPO and –NPO forced CESM experiments. The wind anomalies are calculated as the difference between the ensemble mean (or individual member) and the mean of the CESM control simulation in order to retain non-linearities in the wind forcing. Hereafter, the imposed CESM wind will be referred to as the external "PMM forcing" for the ICM, with the response to the +NPO (–NPO) forced CESM experiments referred to as +PMM (–PMM) forcing.

Four versions of the ICM are run for each external forcing: a fully coupled model, an uncoupled ocean-only model, a model in which only oceanic Rossby waves respond to the external forcing (RW-model), and a model in which only oceanic Kelvin waves respond to the external forcing (KW-model). The fully coupled model allows for full air-sea interactions and atmospheric feedback to influence the oceanic response. The uncoupled model removes all atmospheric feedback to the ocean ($\mathbf{u_c}$ is set to zero), thus allowing the ocean to only respond to the external forcing. The RW-model and KW-model allow the external forcing ($\mathbf{u_f}$) to excite only oceanic Rossby or Kelvin waves, respectively, while

permitting the coupled wind anomalies ($\mathbf{u_c}$) to interact fully with the ocean model. Note that in the Battisti (1988) ICM the shallow water ocean model state is projected into Kelvin and Rossby wave space and the state is evolved via wave characteristics. Thus, in the RW-model $\mathbf{u_f}$ is set to zero in (Equation 2.3) for the Kelvin wave forcing but retained for the Rossby wave forcing and vice-versa for the KW-model. Note that $\mathbf{u_c}$ is retained for both routines in both models so that once an ENSO event is initiated, it can evolve via both Kelvin and Rossby wave propagation. An additional set of sensitivity experiments is run to investigate the source of asymmetry in the ENSO response to PMM forcing, which will be described in Section 2.4.

A wide range of sensitivity experiments are run using various combinations of the PMM external forcing and ICM physics. These experiments (numbered 1 through 10) are summarized in Table 2.1. Readers should refer to Table 2.1 for all references to experiments. For all experiments the phrases "symmetric" and "asymmetric" refer to the degree to which the model response to positive and negative forcing is similar in amplitude but with reverse polarity ("symmetric"), vs. not-similar even with reverse polarity ("asymmetric").

2.3.2 ENSO Response to PMM Forcing

The fully coupled (Experiment 1, Table 2.1) ICM Niño3.4 index (N34) response to the positive and negative ensemble-mean external forcing is shown as black solid lines in Figure 2.4a and Figure 2.4b, respectively. Note that the fully-coupled ENSO response (black solid line, Fig. Figure 2.4a) is normalized by its peak value and plotted in Figure 2.3 to illustrate the sequencing of NPO, PMM and ENSO in our experimental setup. Although the PMM is nearly symmetric (Figure 2.2), the ENSO response generated by this forcing

is not (Fig. Figure 2.4). The sources of asymmetry will be discussed in detail in Section 2.4. The fully coupled ICM N34 index response to the ensemble-mean wind forcing (black) indicates that positive (negative) PMM forcing generates a large warm (cold) ENSO event in boreal fall, approximately one year after the NPO forcing is applied. The N34 index exceeds 1°C during the warm ENSO event. The cold ENSO event, however, is about half the magnitude of the warm event with the N34 index reaching only -.5°C. The fully coupled ICM forced with –PMM also generates a warm ENSO event of similar magnitude to the initial cold ENSO event, the year following the initial cold event. This rebound event of the opposite sign is not seen in the +PMM forced simulations which simply decay throughout the year following the peak of the initial event.

The uncoupled ICM simulations (green lines, Figure 2.4) show the uncoupled oceanic N34 index response to only the PMM forcing since the influence of the Bjerknes feedback is removed (Experiment 2). The externally forced response is about half the amplitude of the fully coupled response and decays to zero earlier than the fully coupled ENSO events. The reduced magnitude of the response is especially apparent in the +PMM forced simulations (Figure 2.4a). In contrast to the coupled case, the uncoupled response to the –PMM (Figure 2.4b) does not generate a warm rebound event following the initial cold event suggesting the warm rebound is not generated by the PMM forcing, but a result of the coupled response.

The anomalous SST and thermocline structure of the fully coupled ENSO response due to the ensemble-mean +PMM and –PMM forcing is shown in Figure 2.5. Since we are primarily interested in the mechanisms responsible for ENSO generation, we only show the seasons leading up to the peak of the ENSO event. The fully coupled ICM shows a warm (cold) ENSO event peaking in SON(1), approximately one year after the positive (negative) NPO forcing is initially applied. However, the magnitude of the cold

SST anomalies is weaker than the warm event and the largest cold SST anomalies are concentrated in the eastern Pacific, whereas the warm event SST anomalies extend farther west.

The seasonal evolution of the anomalous thermocline response, relative to climatological thermocline depth specified in the model, to the PMM forcing is shown as black contours in Figure 2.5. As early as MAM(1), thermocline anomalies emerge in the northwestern equatorial Pacific, between 0°-15°N, and about 120°-180°E. These anomalies appear prior to substantial SST anomalies, so are likely a direct Rossby wave response to the forcing. By JJA(1) the eastern equatorial Pacific experiences a deepened (shoaled) thermocline for the +PMM (–PMM) forced simulations. Despite the asymmetric response of eastern equatorial Pacific SST by JJA(1) the thermocline anomalies are largely symmetric until SON(1) and beyond.

To determine the robustness of the response to the ensemble-mean PMM forcing we analyze the spread of the N34 index responses across the 40 ensemble members to +PMM and –PMM wind forcing for the fully coupled ICM (Experiment 3). The black lines in Figure 2.6 show the response of the ICM to the ensemble-mean PMM wind forcing (as in Figure 2.4). Although the ENSO response to the ensemble-mean PMM forcing clearly suggests the importance of the extra-tropical atmospheric forcing to ENSO generation, the large spread of the individual ensemble responses indicates the ICM is highly sensitive to perturbations in the external PMM wind forcing. To estimate the spread of the ENSO responses we calculate the month containing the largest standard deviation about the mean of all individual ensemble members for both the +PMM and –PMM forced simulations, which are 1.07°C during October and 0.87°C during November, respectively. The conclusions are not sensitive to the month used in the spread calculation. Due to the large spread among ensemble responses, especially for the +PMM case, we can conclude

that natural variability, which is captured by the unforced, internal variability contained within the CESM, likely has a large influence on the formation of any given ENSO event due to its impact on the simulated PMM wind structure. Still, the average response of all individual ICM ensemble members (not shown) is very similar to the ICM response to the ensemble-mean PMM forcing (black lines), and there is a clear tendency for individual +PMM forcings to result in warm ENSO events (red lines, Figure 2.6a), while individual –PMM forcings result in cold ENSO events (blue lines, Figure 2.6b).

2.3.3 Rossby Wave and Kelvin Wave Responses

The effectiveness of PMM wind anomalies in exciting Rossby and Kelvin waves is important because it provides guidance for what physical processes to monitor for understanding PMM/ENSO relationships. Also, both the PMM wind anomalies and ENSO growth rates experience strong seasonality. As a result, the timing of the SST response to PMM forcing (which will appear in the eastern Pacific much more rapidly for Kelvin wave forcing than for Rossby wave forcing) may depend on details of how the forcing excites an equatorial response.

The SST response in the RW-model (Experiment 4) illustrates the evolution of the ICM when the external forcing is only allowed to excite equatorial Rossby waves. The RW model does not generate a ENSO event for the positive forcing case (red curve, Figure 2.4a). However, the negative forcing excites a large persistent warm ENSO event (red curve, Figure 2.4b). The seasonal SST and thermocline response in the RW model is shown in Figure 2.7. During the early seasons [MAM(1) and JJA(1)] both +PMM and –PMM forcing produce thermocline anomalies in the northwestern tropical Pacific, as in Experiment 1. Early in the season, these thermocline anomalies have nearly symmetric structures between the positive and negative forced experiments. However, the

SST response in the eastern Pacific is very different for the two simulations. In particular, the +PMM forcing produces very weak negative SST anomalies in the eastern equatorial Pacific while the –PMM forcing produces larger and more wide-spread positive SST anomalies from JJA(1) through DJF(2); this discrepancy is discussed within the context of thermocline-SST feedbacks in Section 4. The larger and more-widespread anomalies in the negative forcing simulation are more likely to excite coupled feedbacks during JJA(1) and SON(1), at which time ENSO growth is most pronounced. In either case, the response to Rossby wave forcing tends to counteract the fully coupled response (Figure 2.4).

The KW-model simulations (Experiment 5, blue curves in Figure 2.4) indicate that Kelvin wave excitation from the +PMM (-PMM) forcing dominates the generation of the warm (cold) ENSO events. The seasonally averaged SST and thermocline structures of the externally forced Kelvin wave response are shown in Figure 2.8. As with the RW model, the thermocline response is relatively symmetric during MAM(1) and JJA(1), and starts to diverge after SON(1), especially in the western equatorial Pacific. The associated SST anomalies in the eastern equatorial Pacific have larger amplitude for the +PMM than for the –PMM forcing. In the western Pacific, thermocline anomalies for the KW-model simulations are far more confined to the equator than the structures seen in Experiments 1 and 3, especially during SON(1). Western Pacific thermocline anomalies in the KW-model experiments can only be caused by the internally-generated coupled wind anomalies in the KW-model (as $\mathbf{u_f}$ does not force Rossby waves in the KW-model). The meridionally broader structure in the fully coupled experiments (Experiments 1 and 3) suggests that PMM wind anomalies ($\mathbf{u_f}$) force higher-order Rossby waves which are less effective (via smaller reflection coefficients) at generating Kelvin waves that ultimately generate the ENSO response in the eastern equatorial Pacific.

2.3.4 Seasonality

The role of the PMM in generating ENSO depends both on the direct response to PMM forcing and to the ENSO growth rate, the latter of which is largest during boreal summer and fall (Battisti, 1988). To investigate the dependence of the ENSO response to the seasonality of the PMM, we ran the ICM with the positive PMM wind forcing applied with a 0 month (identical to Experiment 1), +3 month, +6 month, and +9 month lag (Experiment 6). The original (lag 0mo) PMM forcing refers to the observed CESM timing of the PMM, where the PMM amplitude peaks in boreal spring (MAM) (Figure 2.3 shows the timing of the original PMM forcing). For the lag +3mo experiment the same sequence of CESM-generated PMM wind forcing is applied to the ICM, but it is applied 3mo *after* the CESM timing [i.e. the PMM peaks during summer, (JJA)]. We lag the wind forcing rather than rerunning CESM with lagged NPO forcing so that we can use an identical wind forcing in the ICM to cleanly separate the effect of seasonality in the ENSO growth rate from seasonality of the PMM. In a similar way, the lag +6mo refers to the PMM peaking in fall (SON), and the lag +9mo refers to the peak of the PMM occurring in winter (DJF).

Figure 2.9 shows the N34 index responses of the uncoupled (top) and fully coupled ICM (bottom) to the lagged +PMM forcing. The solid line indicates the ENSO response to the original PMM forcing (lag 0), the dashed line shows the response to the PMM forcing applied at lag +3mo, the dotted line shows the response to lag +6mo PMM forcing, and the dot-dash line shows the response to lag +9mo PMM forcing. The uncoupled ICM simulations (Figure 2.9a) all result in similar magnitude ENSO events with N34 index peaking at .5°C. However, the N34 index peaks in January for the lag +3mo forcing, in March for the lag +6mo forcing, and in July for the lag +9mo forcing. The shift in the timing of the uncoupled ENSO event is consistent with the lag of the applied PMM

forcing and indicates that the direct response does not depend strongly on seasonality of the forcing. Kelvin and Rossby Wave model simulations with lagged forcing also support this result (not shown).

The fully coupled simulations show the importance of the seasonality of the ENSO growth rate due to coupled interactions with the seasonally varying mean state (Figure 2.9b). The lag +9mo and lag 0 simulations indicate the strongest ENSO response occurs when the Kevin wave signal reaches the eastern Pacific in boreal summer and fall, respectively, corresponding to the timing of large potential instability for ENSO (Battisti, 1988). In terms of thermocline/SST relationships, this large instability corresponds to boreal summer and fall, when zonal SST gradients are largest across the Pacific, and the thermocline in the eastern equatorial Pacific is nearest to the surface (Zhu et al., 2015). The weakest ENSO response occurs when the Kelvin wave signal arrives in the eastern Pacific during boreal spring (lag +6mo simulation, Figure 2.9b), which corresponds to a minimum in oceanic instability and ENSO growth potential. At that time, mean zonal wind and mean zonal SST gradients are weak, and the thermocline is farthest from the surface in the eastern Pacific, reducing potential ENSO growth (Zhu et al., 2015). While the lagged PMM forcing represents a physically unrealistic situation, since the PMM has an observed seasonality, the results are instructive since they demonstrate that timing of the PMM forcing as it occurs in nature is best suited to generate ENSO growth.

2.4 Sources of Asymmetry

This section identifies the sources of ENSO asymmetry simulated by the ICM. The four potential sources producing the asymmetry within our experiments include: asymmetry in the PMM forcing; the atmospheric heating calculation within the ICM, which includes an iterative convergence feedback and nonlinear dependence on regions of mean state

moisture convergence (Zebiak and Cane, 1987); the non-linear calculation of pseudo-stress from wind within the ICM (Equation 2.2); and oceanic dynamics, primarily the effect of upwelling on an anomalously shallow or deep thermocline. In this section we systematically remove each of these nonlinear processes to investigate the influence of each on the asymmetric ENSO response to the PMM forcing. We note that of the various sources of asymmetry, the atmospheric heating calculation and the relationship between subsurface temperature and thermocline depth are very dependent on parameterizations within the ICM, while the wind and pseudo-stress calculations are not (i.e. asymmetric results due to asymmetric wind forcing or non-linear pseudo-stress calculations may be more generally applicable in nature). This will be addressed in more detail in Section 2.5.

First, the role of asymmetry in the ensemble-mean CESM simulated PMM *wind* is examined. In calculating the wind stress (Equation 2.2), the externally applied wind forcing $\mathbf{u_f}$ was replaced with either $+1$ times the *positive* PMM wind anomalies (identical to the positive forcing in experiment 1), or -1 times the *positive* PMM wind anomalies. Thus, the fully coupled ICM is forced with linear opposite PMM *wind*, referred to as the positive and negative forcing (Experiment 7). The resulting N34 indices due to the positive and negative wind forcing are plotted as a solid and dashed black lines, respectively, in Figure 2.10a and are nearly indistinguishable from the corresponding indices in Figure 2.4. This is consistent with the approximately symmetric PMM wind response to NPO forcing, as seen in Figure 2.2, and indicates that any slight asymmetry of the PMM wind is not responsible for the asymmetric ENSO responses. For consistency, experiments 7, 8, 9 and 10 will continue to use $+1$ (-1) times the positive PMM wind anomalies for "positive" ("negative") forcing, respectively.

Next, the role of nonlinearity in the pseudo-stress calculation (Equation 2.2) is examined by using linearly opposite *pseudo-stress* to force the ICM (Experiment 8). To estimate a

"linear" component of the pseudo-stress, the pseudo-stress anomalies ($\tau'_{\mathbf{t}}$) are calculated separately for the forcing ($\mathbf{u_f}$) and the coupled ($\mathbf{u_c}$) wind anomalies via:

$$\tau'_{\mathbf{f}} = (\mathbf{u_m} + \mathbf{u_f})|\mathbf{u_m} + \mathbf{u_f}| - \mathbf{u_m}|\mathbf{u_m}| \quad (2.4)$$

$$\tau'_{\mathbf{c}} = (\mathbf{u_m} + \mathbf{u_c})|\mathbf{u_m} + \mathbf{u_c}| - \mathbf{u_m}|\mathbf{u_m}| \quad (2.5)$$

$$\tau'_{\mathbf{t}} = \tau'_{\mathbf{f}} + \tau'_{\mathbf{c}} \quad (2.6)$$

where $\tau'_{\mathbf{t}}$ is the total psuedo-stress anomaly applied in the model. First, the +PMM wind forcing is used to calculate $\tau'_{\mathbf{f}}$ and the ICM is run by replacing (Equation 2.2) with (Equation 2.5); results are plotted as a solid blue line in Figure 2.10a. Next, the ICM is re-run with the same $\tau'_{\mathbf{f}}$ calculated from the +PMM wind [i.e. (Equation 2.3) is the same] but $\tau'_{\mathbf{f}}$ in (Equation 2.5) is multiplied by -1 to simulate a negative external forcing. Hence, the resulting $\tau'_{\mathbf{f}}$ in (Equation 2.5) is the exact linear opposite of the "positive" case. The resulting N34 evolution (plotted as blue dashed line in Figure 2.10a) remains very similar to the fully coupled case (Experiment 1, black line in Figure 2.4b). The similarity of the N34 evolution from Experiment 7 (black lines Figure 2.10a) and Experiment 8 (blue lines Figure 2.10a) indicates the nonlinear pseudo-stress calculation plays a minor role in the asymmetric ENSO response in this case.

Nonlinearity in the atmospheric heating is implicitly addressed in the uncoupled simulations (Experiment 2; green lines in Figure 2.4), which show that warm ENSO events produced by +PMM wind anomalies have larger amplitude than the cold ENSO events produced by the –PMM forcing. We repeated the uncoupled experiment with linearized wind (as in Experiment 7) or linearized pseudo-stress (as in Experiment 8), and found the results did not differ substantially from the original uncoupled case (Experiment 2). Results from the linearized uncoupled experiments are not shown due to similarity with

the original uncoupled simulations. We also determined the iterative quality of the heating calculation from the model had little influence on the results. As such, nonlinearity in the atmospheric heating calculation is not responsible for the asymmetric ENSO response to the PMM.

Finally, to show the asymmetric ENSO response is largely a result of the relationship between thermocline depth and anomalous vertical temperature gradients, the subsurface temperature dependence on thermocline depth was made symmetric around the mean thermocline depth (Experiments 9 and 10). The model parameterizes the subsurface temperature anomaly (T_{sub}) in terms of the upper layer height anomaly (h), or thermocline depth anomaly, as follows (Battisti, 1988):

$$T_{sub} = \Theta(h)[\tanh[\lambda(h_{bar} + 1.5|h|)] - \tanh[\lambda h_{bar}], \tag{2.7}$$

where parameters Θ = 28 K and λ^{-1} = 80 m for h > 0, and Θ = -40 K and λ^{-1} = 33 m for h <= 0, and h_{bar} is the mean thermocline depth along the equator as a function of longitude (solid line; Figure 2.11). For the linearized thermocline experiments the parameters are changed to Θ = 28 K and λ^{-1} = 80 m for h > 0, and Θ = -28 K and λ^{-1} = 80 m for h <= 0 which results in a symmetric subsurface temperature structure as a function of the thermocline depth perturbation (dashed line; Figure 2.11). The original asymmetry between positive and negative thermocline anomalies is related to the vertical temperature structure of the ocean and equatorial upwelling, and is dependent on the mean thermocline depth (h_{bar}): SST tendency in locations where the mean thermocline is near the surface (e.g. the eastern equatorial Pacific) is more sensitive to changes in thermocline depth (via mean upwelling) than regions where the mean thermocline is far from the surface.

Figure 2.10b shows the same simulations as in Figure 2.10a, except using the symmetric subsurface temperature (T_{sub}) structure as described above. The fully coupled N34 index response to the linear PMM wind forcing (solid and dashed black lines respectively, Experiment 9) indicates that the asymmetry in the T_{sub} parameterization is largely responsible for the asymmetric N34 response. However, with symmetric T_{sub} parameterization, the response to –PMM wind anomalies has *larger* amplitude than the response to +PMM wind anomalies. When the nonlinearity in the wind stress calculation is also removed (Experiment 10, blue lines in Figure 2.10b), the ENSO response to the PMM forcing is nearly symmetric. These results show that in the absence of nonlinearity arising from T_{sub} asymmetry (e.g. where the thermocline-SST feedbacks are weak) the wind stress calculations and other nonlinearities tend to produce stronger *cold* ENSO events. Implications of this finding will be discussed in Section 2.5.

2.5 Conclusions

A set of ensemble simulations using the NCAR Community Earth System Model (CESM) and the Battisti (1988) version of the Zebiak and Cane (1987) intermediate coupled model (ICM) were run to examine the ENSO response to the Pacific Meridional Mode (PMM). These two models were chosen due to the complementary physics each model contains. The CESM (run with CAM5 physics coupled to a slab ocean model) contains the atmosphere-ocean coupling required to simulate the PMM, but does not contain ocean dynamics to simulate ENSO. The ICM contains the necessary ocean dynamics to simulate ENSO, but is unable to simulate the PMM due to lack of wind-induced evaporation. The combination of the CESM and the ICM used in this study cleanly separates the interactions between the PMM and ENSO, thus allowing us to identify the dominant mechanisms through which the PMM interacts with ENSO.

We find the CESM generates a response representative of the PMM when forced with the surface heat flux associated with the North Pacific Oscillation (NPO), consistent with VAF2009. The positive (negative) NPO forcing initiates a persistent warm (cold) SST anomaly that propagates into the tropical Pacific. This SST anomaly subsequently generates westerly (easterly) wind anomalies in the western and central equatorial Pacific. We find the symmetric response of the CESM to the NPO forcing is much larger than the asymmetric response, suggesting that the PMM is essentially linear.

While our CESM results support the known connection between the NPO and PMM variability, the results from the ICM experiments reflect the importance of extra-tropical atmospheric forcing in the development of ENSO events through the PMM. The fully coupled ICM produces a warm (cold) ENSO event that peaks in the boreal fall (SON) when forced with the +PMM (–PMM) ensemble-mean wind anomalies. Although this model tends to simulate ENSO events that peak a couple of months early, it is a useful tool for diagnosing the connection between the PMM and ENSO. Previous studies also show the connection between PMM variability and ENSO variability (Chang et al., 2007, Larson and Kirtman, 2013, Lin et al., 2014, Vimont et al., 2003a, 2014, Zhang et al., 2009); here, the specific mechanisms through which PMM variability excites ENSO development are explored. The sensitivity experiments performed using the ICM in this study show oceanic Kelvin waves are the dominant mechanism responsible for ENSO development due to PMM atmospheric forcing. This is especially true for the response to the positive forcing. Although Kelvin waves dominate the initial ENSO response to both positive and negative PMM atmospheric forcing, we find externally excited oceanic Rossby waves are only significant for the ENSO response in the tropical Pacific in the –PMM forced case. Furthermore, we show the importance of the seasonality of the PMM on ENSO generation through interactions with Kelvin and Rossby wave mechanisms.

The seasonality of the CESM simulated PMM, which peaks in boreal spring, supports ENSO growth through Kelvin wave propagation. These results support the importance of Kelvin wave propagation in ENSO development found in previous studies (Alexander et al., 2010, Vimont et al., 2003a,b).

The large spread between individual ensemble members indicates the importance of natural variability in the PMM/ENSO relationship. Natural variability, captured by the unforced, internal variability of the CESM, is especially important to the structure of simulated PMM wind anomalies. Variations in the initial conditions and random noise result in a large range of ENSO responses between ensemble members. Due to this large spread, we conclude natural variability has important implications for the predictability of ENSO through the PMM. Although the ensemble shows a clear bias towards warm (cold) ENSO events when forced with positive (negative) PMM winds, not all PMM simulations generate an El Niño event, supporting the results found in Chang et al. (2007). Other studies show similar a relationship between the PMM and ENSO. Larson and Kirtman (2015) also find a warm ENSO bias in response to the positive PMM. The large spread between ensemble members may indicate low skill for ENSO predictability using solely the PMM. Similarly, Larson and Kirtman (2014) show little skill in ENSO forecasts using the PMM, motivating further research to better understand the role of natural variability and stochastic forcing in ENSO development.

We also found the ENSO response simulated by the ICM to positive and negative PMM wind anomalies is asymmetric, despite the ICM being in a linearly stable regime. Several sensitivity experiments utilizing the ICM demonstrated that ocean dynamics within the ICM dominate the ENSO asymmetry. Most notably, the non-linear parameterization of sub-thermocline temperature in the ICM dominates the asymmetry in the ENSO response to PMM forcing. After "symmetrizing" (i.e. making symmetric around the mean

thermocline depth) the sub-thermocline temperature parameterization as a function of thermocline depth, we find the ICM produces stronger *negative* ENSO events due to wind stress calculations and other nonlinearities.

The nonlinearities of the ICM are understood and known to be strongly dependent on the thermocline parameters. However, the results obtained after these thermocline nonlinearities are removed may shed some light on observed ENSO behaviors. The N34 results from simulations containing a symmetric thermocline-SST feedbacks indicate the importance of the wind stress effects that were previously masked by the thermocline dynamics. In these simulations, the ICM generates larger magnitude cold ENSO events, indicating the importance of the wind stress on ENSO variability in the absence of strong thermocline variations. Although the ICM is incapable of simulating ENSO diversity, these results may have implications for ENSO characteristics that may be masked by the large non-linear thermocline behaviors. For example, events that rely less on thermocline-SST feedbacks, such as Central Pacific (CP) ENSO events (Kao and Yu, 2009), may be more influenced by atmospheric forcing. We do, in fact, find stronger cold ENSO events in the absence of thermocline / temperature asymmetry largely due to wind stress, which is consistent with the negative skewness of CP ENSO events (Kao and Yu, 2009). We reiterate, though, a more complete analysis of how the PMM influences ENSO diversity should be conducted with a model that better simulates such ENSO diversity.

We acknowledge the use of an unrealistic intermediate coupled model with known biases in this study. Despite these limitations, results herein do contribute to our understanding of PMM / ENSO interactions. In particular, the results highlight the importance of directly-forced Kelvin waves in the PMM's influence on ENSO initiation, and the potential importance of non-linearity in wind stress and thermocline/SST interactions in producing nonlinear ENSO responses. Furthermore, the results from individual model

simulations show that natural variability and stochastic forcing may play a very strong role in ENSO initiation and development. Future work to identify stochastic forcing structures that are either favorable or detrimental for ENSO development with respect to the NPO/PMM initiation mechanism, including development of ENSO diversity which is not fully addressed herein, would be beneficial.

TABLE 2.1: Summary of Intermediate Coupled Model Experiments

Experiment	Forcing	Result	Interpretation
(1) Full ICM	+/− Ensemble-mean PMM Wind	+PMM ⇒ + ENSO −PMM ⇒ −ENSO	Greater amplitude response to +PMM
(2) Uncoupled	As in (1)	As in (1)	Weaker amplitude response than in (1)
(3) Full ICM: Ensemble	+/− PMM Wind of individual ensemble members	Ensemble mean as in (1), Individual runs vary widely	As in (1), but role of natural variability is important
(4) RW-model	As in (1)	+PMM ⇒ no ENSO −PMM ⇒ +ENSO	PMM forced Rossby waves do not strongly influence fully coupled response
(5) KW-model	As in (1)	As in (1), but greater amplitude	PMM forced Kelvin waves dominate fully coupled response
(6) Seasonally Shifted Forcing	+PMM Wind shifted by 0, 3, 6 or 9 months	All produce warm ENSO events, but largest amplitude for lag 0 and lag +9mo	Seasonality of ENSO growth rate influences amplitude of response
(7) Linear Wind	+PMM Wind, −1∗(+PMM Wind)	As in (1)	As in (1)
(8) Linear Stress	+PMM Stress, −1∗(+PMM Stress)	As in (1)	As in (1)
(9) Linear Wind and Thermocline	As in (7)	+PMM event has lesser amplitude than –PMM event	When thermocline effects removed, other non-linearities generate larger cold ENSO events
(10) Linear Stress and Thermocline	As in (8)	ENSO response is nearly linear	Non-linear ENSO response, as in (1), is dominated by thermocline

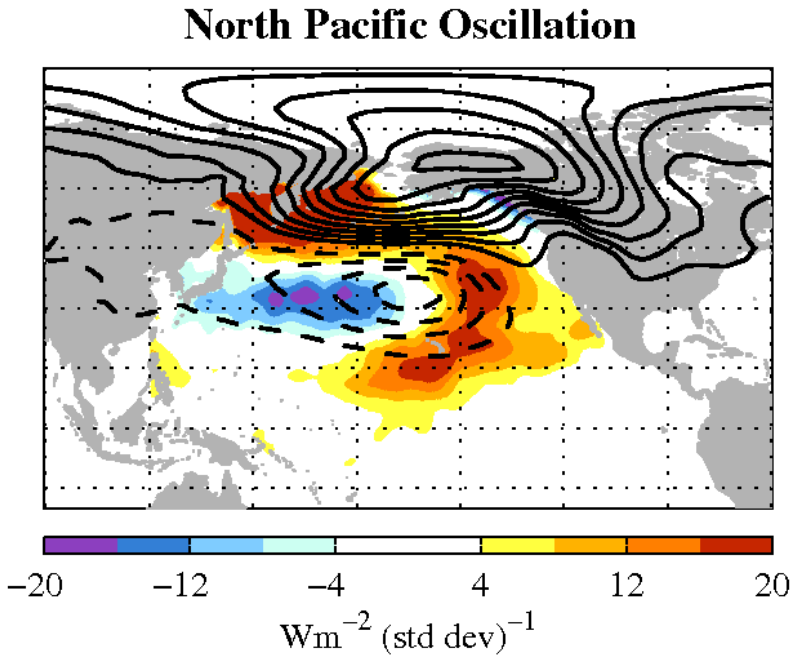

FIGURE 2.1: Boreal winter sea level pressure (black contours) and net surface heat flux (shading) associated with the positive phase of the NPO (defined as the second EOF of intra-seasonal SLP in the North Pacific). The SLP contour interval is 0.5 mb (std dev)$^{-1}$. Solid (dashed) contours correspond to positive (negative) values. The zero contour has been omitted. Downward heat fluxes are defined as positive. The negative phase of the NPO is the opposite polarity.

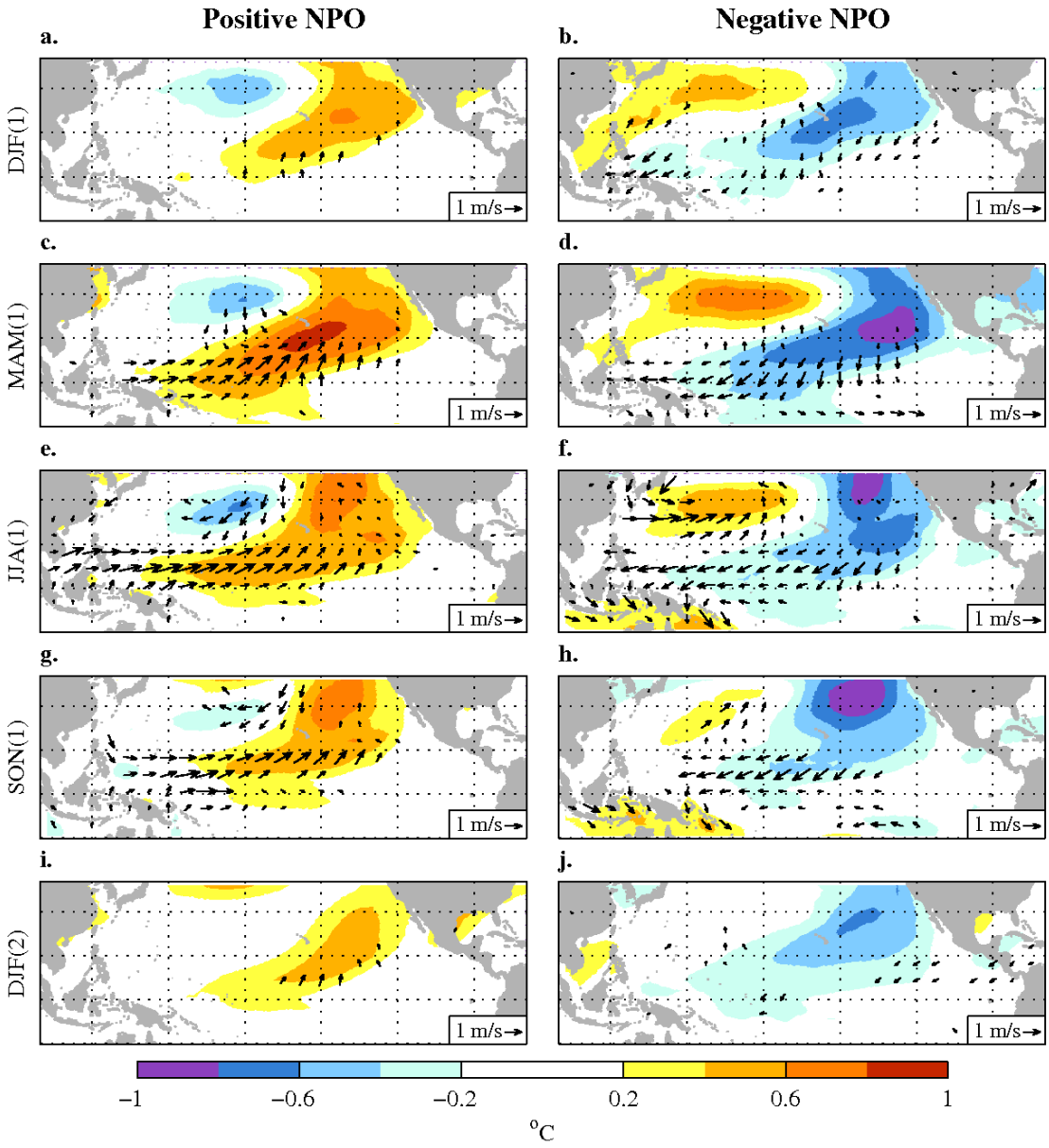

FIGURE 2.2: Seasonally averaged ensemble-mean CESM SST (shaded) and low level wind (vectors) anomalies due to positive (left column) and negative (right column) NPO surface heat flux forcing. Values are only plotted where they exceed the 95% confidence level based on a two tailed univariate (or bivariate in the case of vectors) T-test.

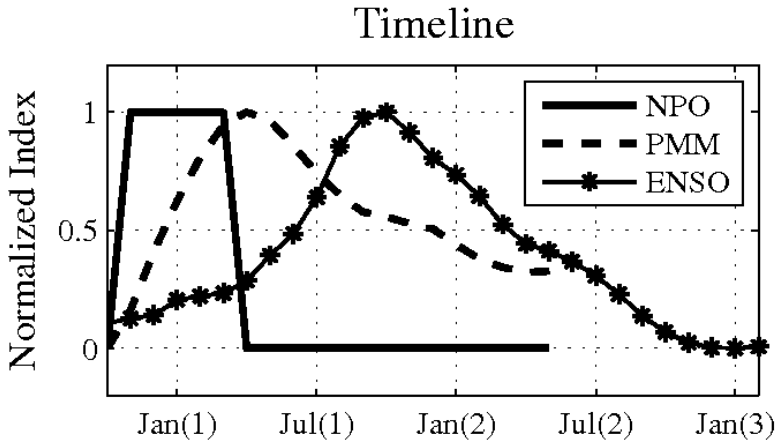

FIGURE 2.3: Timeline showing the relative occurence of the NPO heat flux forcing (solid line), the PMM (dashed line), and the resulting ENSO event (stars); see text for details. The NPO index shows constant, maximum forcing applied to the 20-month CESM simulations during boreal winter (NDJFM). The PMM index is calculated by projecting the ensemble-mean SST pattern simulated by the CESM onto the spatial pattern of the PMM defined by Chiang and Vimont (2004) and represents the ensemble-mean temporal evolution of the PMM forcing for the ICM. The PMM index is normalized by the maximum amplitude. The ENSO index (Niño3.4 index) represents the ENSO response to the 20 month ensemble-mean PMM wind forcing.

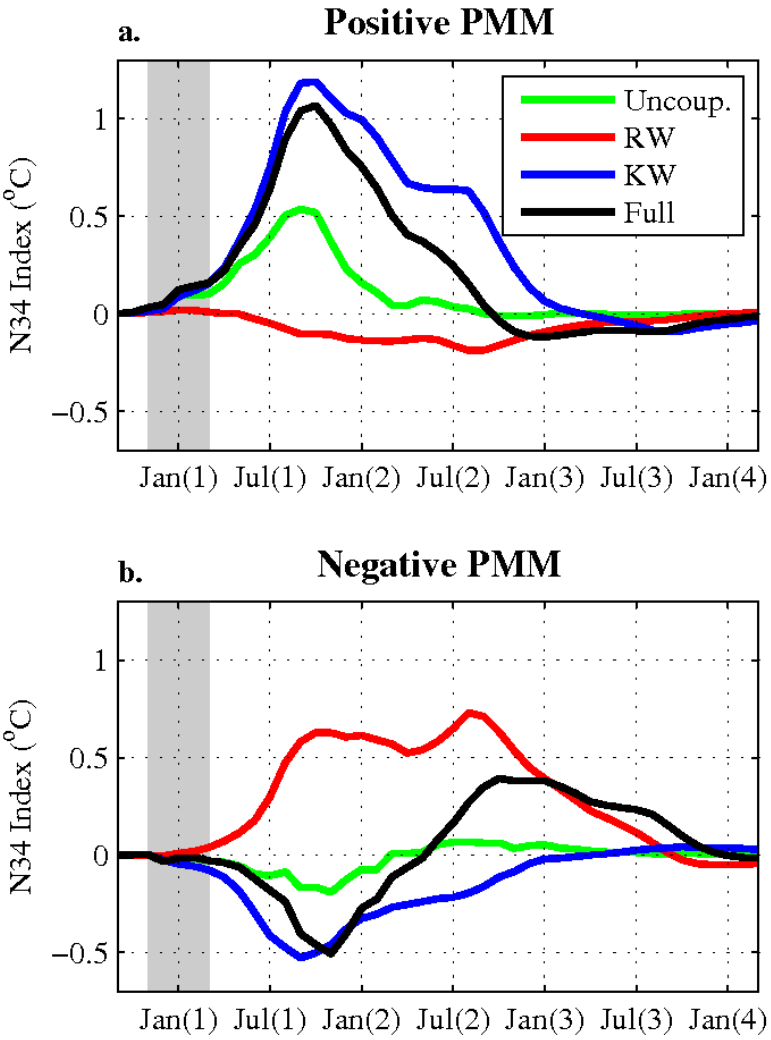

FIGURE 2.4: Niño3.4 index response of the Intermediate Coupled Model to the ensemble-mean PMM wind forcing. Top (bottom) figure shows the response to the positive (negative) PMM wind forcing. The Niño3.4 Index responses of the fully coupled model (black), uncoupled model (green), Rossby wave model (red), and Kelvin wave model (blue) are shown for each forcing. Timing of the boreal winter NPO is indicated with grey shading.

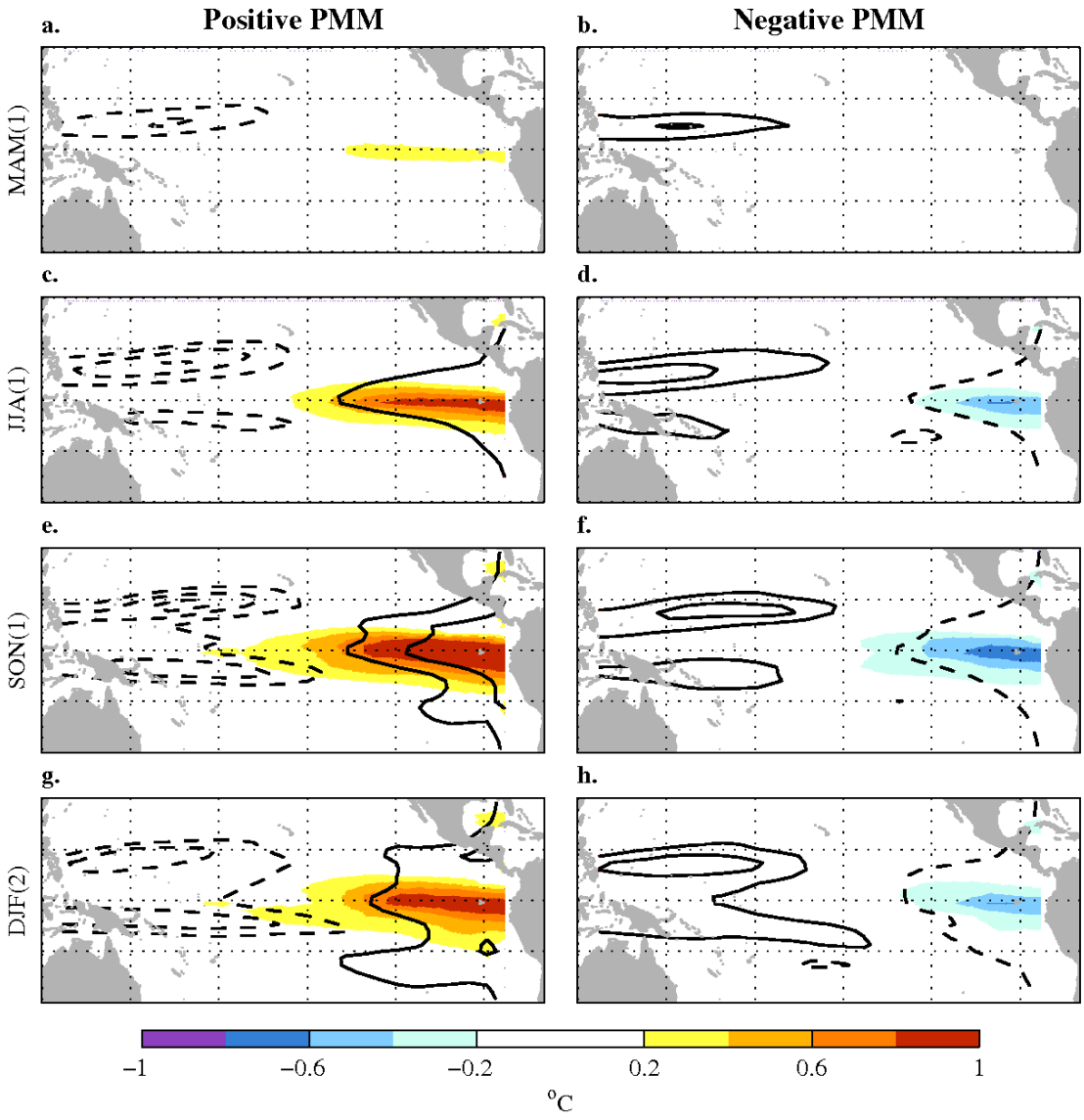

FIGURE 2.5: Fully coupled Intermediate Coupled Model SST (shading) and thermocline depth (black contours) response to positive (left column) and negative (right column) ensemble-mean PMM wind forcing. The thermocline contour interval is every 2.5m. Solid (dashed) contours correspond to a deeper (shoaled) thermocline. The zero contour has been omitted.

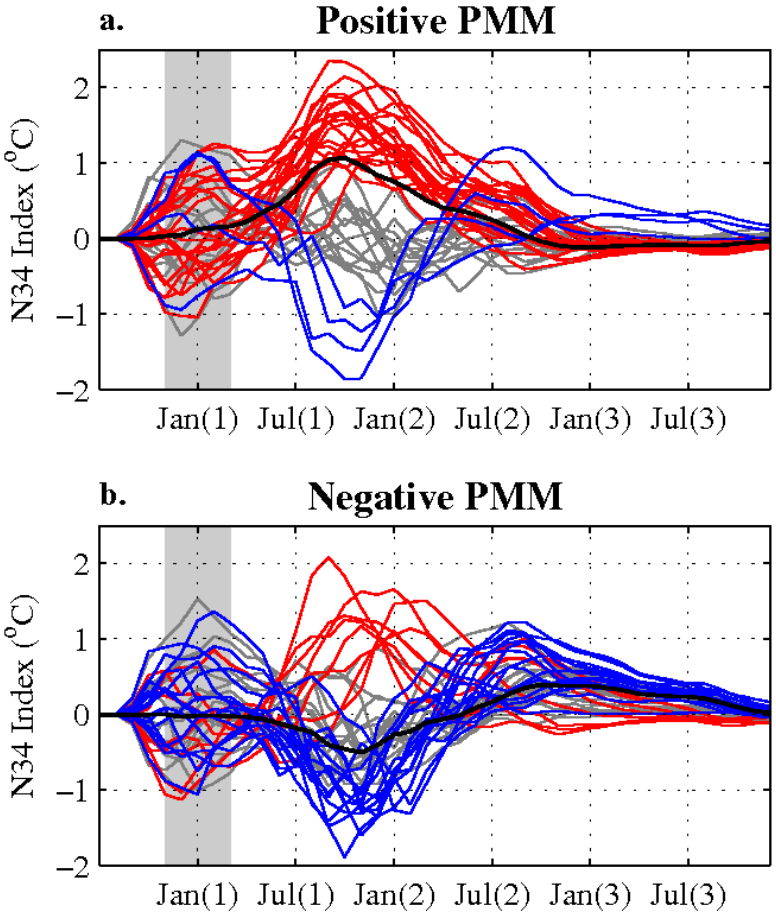

FIGURE 2.6: Ensemble of fully coupled Intermediate Coupled Model Niño3.4 Index responses to the external wind forcing associated with the (a) positive and (b) negative PMM. Black lines show the fully coupled response to the ensemble-mean external atmospheric forcing as seen in Fig. 3. Red lines indicate ensemble members resulting in a warm ENSO event (El Niño). Blue lines indicate ensemble members resulting in a cold ENSO (La Niña) event. Grey lines indicate neutral ENSO events. Warm ENSO events are defined when the N34 index >= 1.0 between Aug(year 1) and Feb(year 2). Cold ENSO events are defined when the N34 index <= –1.0 between Aug(year 1) and Feb(year 2). Neutral events occur when the -1.0 < N34 index < 1.0.

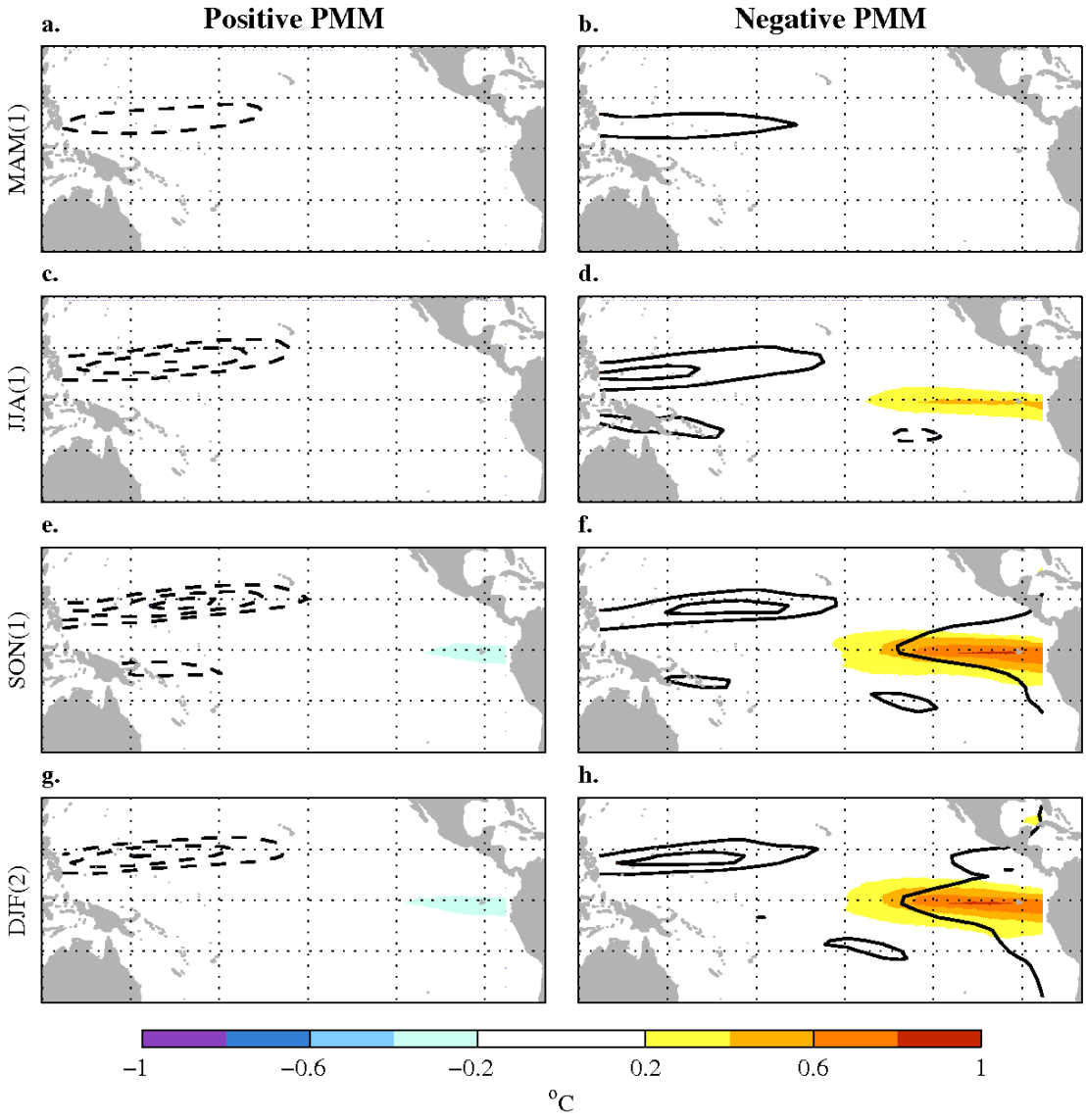

FIGURE 2.7: As in Figure 2.4 for the Rossby Wave Intermediate Coupled Model.

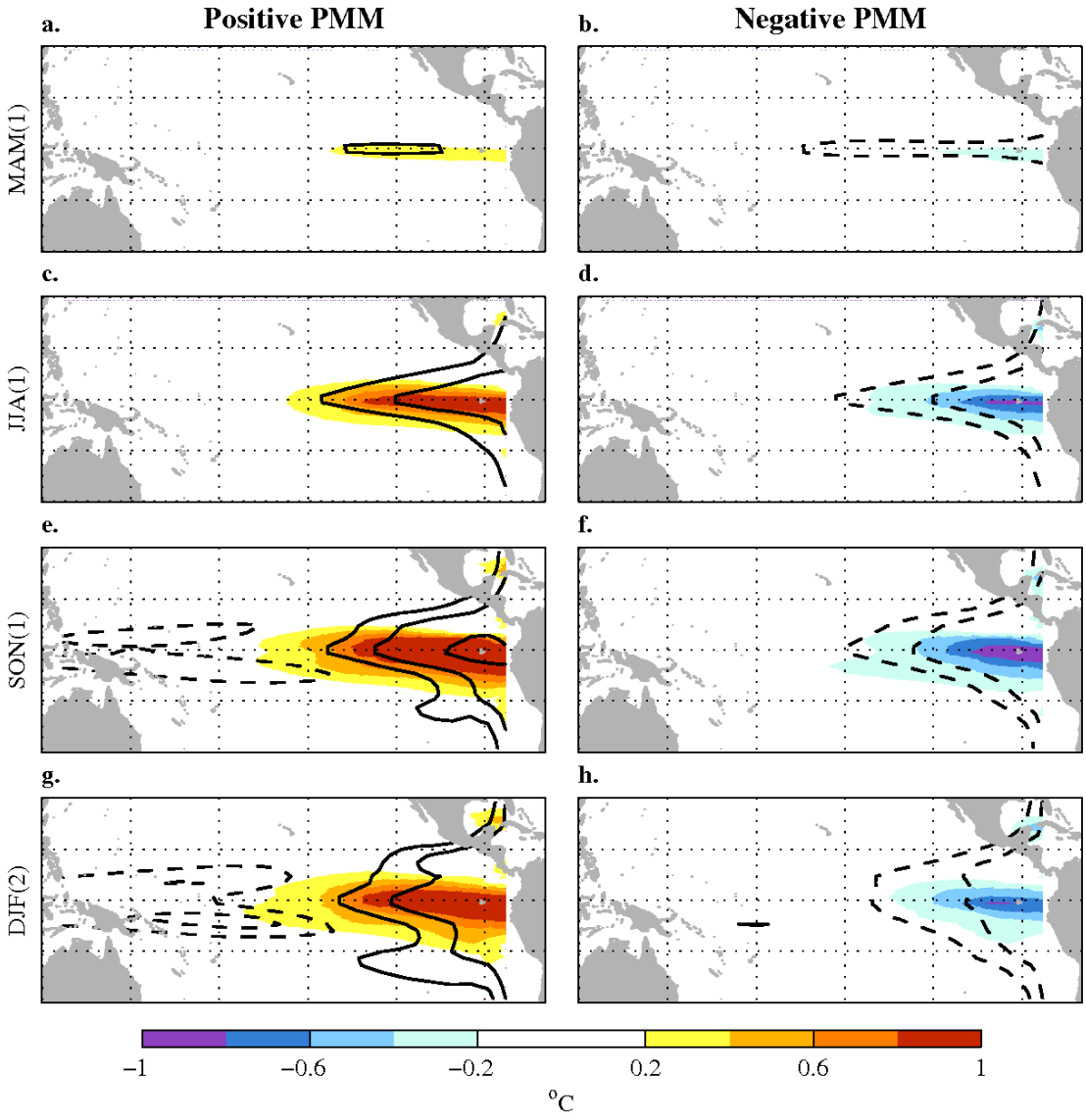

FIGURE 2.8: As in Figure 2.4 for Kelvin Wave Intermediate Coupled Model.

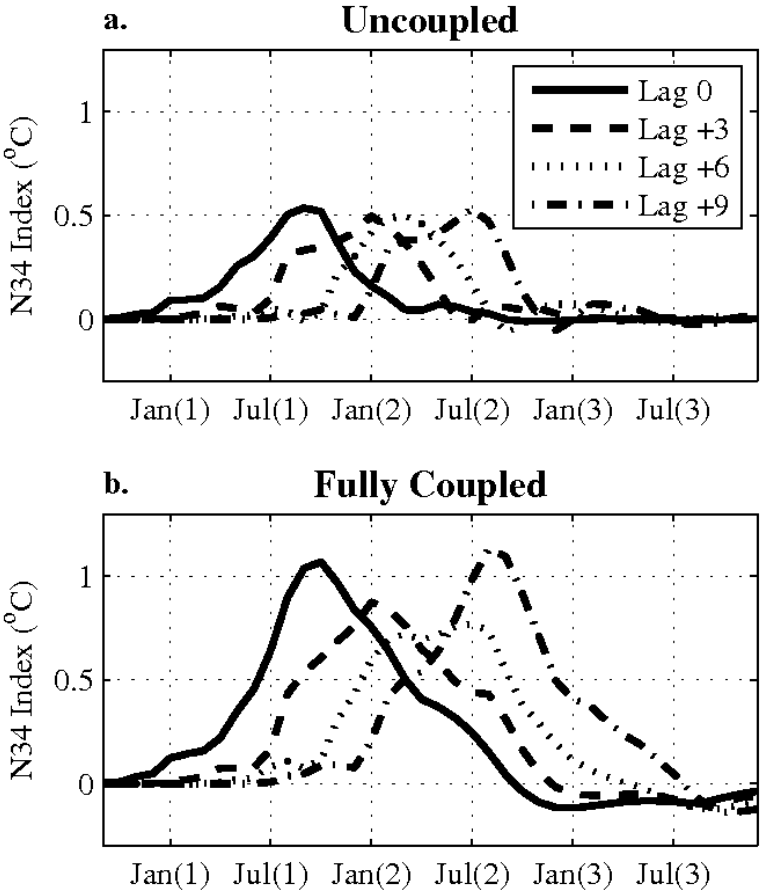

FIGURE 2.9: Niño3.4 index responses of the (a) uncoupled and (b) fully coupled ICM to seasonally lagged positive PMM wind forcing. The solid line indicates the response original +PMM forcing (lag 0), the dashed line shows response when the positive PMM forcing is applied at a +3 month lag, the dotted line shows the response to the forcing at a +6 month lag, and the dot-dash line shows the response to the forcing at a +9 month lag.

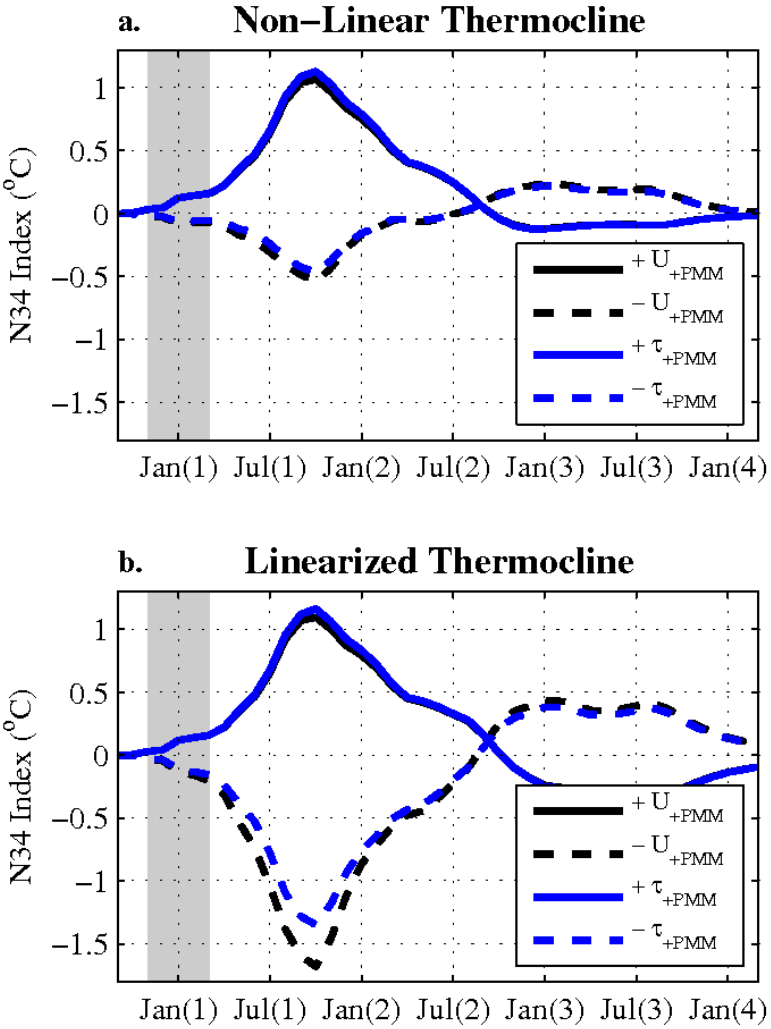

FIGURE 2.10: Niño3.4 Index responses to linearized experiments with the Intermediate Coupled Model. Figure (a) shows the fully coupled model simulations run with positive (solid lines) and negative (dashed lines) ensemble-mean PMM forcing. The black lines represent the linearized PMM *wind* forcing experiment where the sign of the positive external wind is reversed to generate the negative wind forcing (Experiment 7, Table Table 2.1). The blue lines show the linearized PMM wind *stress* experiments where the sign of the wind stress due to positive external forcing is reversed to generate the negative wind stress (Experiment 8). Figure (b) shows the same experiments as (a) with linearized thermocline parameters (Experiments 9 and 10).

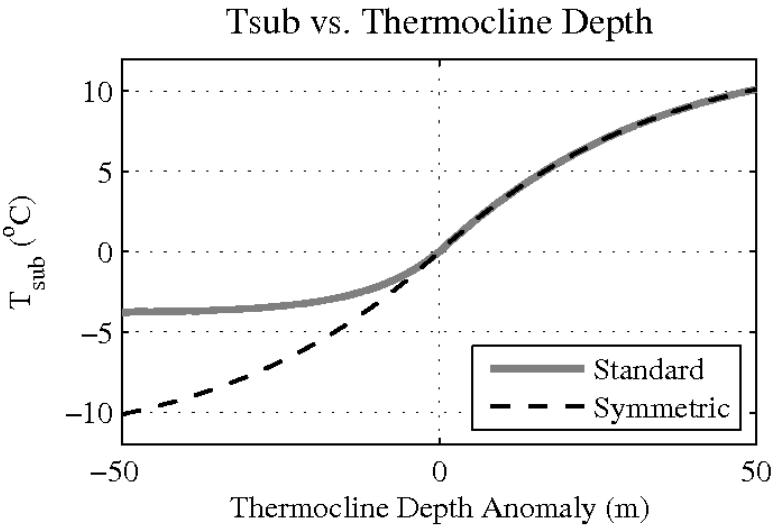

FIGURE 2.11: Intermediate coupled model subsurface temperature structure as a function of the thermocline depth anomaly. The standard thermocline structure is shown in the solid grey line while the symmetric thermocline structure with linearized thermocline parameters is shown in the black dashed line.

Chapter 3

The Role of Stochastic Forcing in generating ENSO Diversity in Observations: Methodology

A subset of the content of this chapter has been accepted with revisions to the *Journal of Climate* as Thomas, E. E., et al.: The Role of Stochastic Forcing in generating ENSO Diversity, *In Review*.

3.1 Introduction

El Niño and the Southern Oscillation (ENSO) is the dominant source of interannual climate variability on Earth (see, e.g., Wallace et al. 1998), and has large impacts on global climate patterns (Alexander et al. 2002; Diaz et al. 2001). While theories exist to explain the gross spatial and temporal characteristics of ENSO evolution (Zebiak and Cane 1987; Battisti 1988; Battisti and Hirst 1989; Suarez and Schopf 1988; Jin 1997;

Penland and Sardeshmukh 1995; Neelin et al. 1998), the spatial and temporal evolution of individual events show considerable diversity (see Capotondi et al. 2015 for a review). Diversity exists within ENSO spatial characteristics, the predictability of events, and the timing of events. Spatial diversity is often characterized using terms such as Central Pacific (CP) or Eastern Pacific (EP) (e.g. Ashok et al. 2007; Capotondi 2013, Capotondi et al. 2015; Kim et al. 2012a,b; Kao and Yu 2009; Yu and Kim 2011; Kug et al. 2009, 2010a). Spatial ENSO diversity arises due to the varying roles of different physical processes allowing any given ENSO event to have a continuous range of CP and EP characteristics (Karnauskas 2013; Capotondi et al. 2015). This study provides a general framework to identify and characterize the role of these physical processes in generating ENSO diversity within the context of the dynamically evolving ENSO system.

A variety of physical processes have been proposed to explain ENSO diversity. In this study, we take a forecast perspective in which the evolution of an individual ENSO event from a given time depends on (i) the specific set of initial conditions that determine how the system will evolve along its deterministic trajectory, as well as (ii) the "external" forcing that, when convolved with the dynamics, pushes the system away from (in general) the deterministic trajectory. A third possibility exists that ENSO diversity is caused by variations in the internal dynamics responsible for ENSO evolution (e.g. Fedorov and Philander 2000, 2001; An and Wang 2000; An and Jin 2000; Wang and An 2002; Yeh et al. 2009; Capotondi and Sardeshmukh 2017). Here, we focus solely on the role of initial conditions and stochastic forcing in generating ENSO diversity.

A variety of studies have implicated external mid-latitude variability in the generation of initial structures in the tropical Pacific that lead to ENSO diversity. Vimont et al. (2014) use linear inverse modeling to identify optimal initial conditions that lead to ENSO events with CP or EP characteristics. They find that CP-related initial conditions are associated

with the Pacific meridional mode (PMM; Chiang and Vimont 2004) through the "seasonal footprinting mechanism" (Vimont et al. 2001, 2003a,b, 2009; Zhang et al. 2009; Yu and Kim 2011; Park et al. 2013). Southern hemisphere atmospheric variability has also been implicated in generating initial heat content anomalies that can influence EP-type ENSO events (You and Furtado 2017). Other studies show ENSO diversity is associated with the initial state of the ocean heat content, ocean dynamics and basin-wide thermocline variations (Meinen and McPhaden 2000; Kao and Yu 2009; Kug et al. 2010; Horii et al. 2012; Vimont et al. 2014; Fedorov et al. 2015). Last, ENSO initial conditions have been associated with forcing from the tropical Indian Ocean or from the subtropical Atlantic (Penland and Matrosova 2006).

Variations in stochastic forcing (here we loosely define stochastic or external forcing as forcing that is external to the essential deterministic dynamics that produce ENSO variability) have also been shown to generate ENSO diversity. Newman et al. (2011b) show that ENSO diversity arises naturally in stochastically-forced linear inverse model simulation with an unchanging dynamical description, confirming that stochastic forcing is a sufficient condition for generating ENSO diversity. Studies also show that ENSO events with strong EP characteristics, such as the 1997/1998 El Niño event, are influenced by westerly wind busts (WWBs) that occur in the western tropical Pacific (Boulanger and Menkes 1999; McPhaden 1999; Harrison and Chiodi 2009; Federov et al. 2015; Chen et al. 2015).

In the present study, we use linear inverse modeling (LIM; Penland and Sardeshmukh, 1995) to identify physical mechanisms associated with the generation of initial states and stochastic forcing that can produce ENSO diversity. LIM provides an observationally based, empirical model that approximates slow dynamical processes via a deterministic

linear dynamical operator, and the effect of fast processes as Gaussian white noise. Penland and Sardeshmukh (1995) use LIM to show ENSO growth can occur via non-normal processes in a linearly stable dynamical system. In that case, stochastic forcing maintains climatological variance, and explains the observed temporal irregularities of ENSO variability. Penland (1996) shows that the linear approximation of the slow dynamics of the Indo-Pacific forced by seasonally varying noise can account for observed temporal ENSO behaviors, such as the seasonal ENSO phase-locking. LIM is also successfully used to forecast the tropical ocean / atmosphere system (Newman 2007; Newman et al. 2011a; Penland and Matrosova 1998; Penland and Magorian 1993; Alexander et al. 2008).

LIM has been successfully used as a diagnostic tool for understanding the physical processes that generate ENSO variability. LIM allows for an objective, observationally grounded calculation of the initial state that maximizes deterministic growth towards a specified final state. Previous studies show that the optimal initial conditions maximizing tropical Pacific SST growth contain SST anomalies north of the equator and in the far eastern equatorial Pacific (Penland and Sardeshmukh 1995; Newman et al. 2011a). Newman et al. (2011a) also show the optimal initial condition contains positive thermocline depth anomalies throughout the central Tropical Pacific. Applying LIM methods to ENSO diversity, Capotondi and Sardeshmukh (2015) show SST precursors alone are not sufficient to the capture the development of ENSO diversity, and the thermocline initial state is important to the capture the development of CP and EP spatial characteristics. Vimont et al. (2014) show the optimal initial conditions that maximize CP growth are strongly related to SST patterns representative of the PMM and deep (shallow) thermocline anomalies in the west (east) Pacific. The optimal initial conditions for EP growth contain positive SST anomalies in the far eastern Pacific and depressed thermocline anomalies throughout the central equatorial Pacific (Vimont et al. 2014).

Although studies have previously characterized the optimal initial conditions for maximum CP and EP growth (Vimont et al. 2014; Capotondi and Sardeshmukh 2015), the specific structures within the stochastic forcing that generate these initial conditions have not been identified. In this study, we characterize the role of stochastic forcing mechanisms in generating CP or EP ENSO characteristics using a LIM forecast framework to separate the deterministic evolution of the tropical Pacific from the unpredictable, or noise forced, evolution. In the forecasting framework, it is possible the noise forcing can excite optimal initial conditions that enhance deterministic growth, and thus improve the predictability of an event. However, the same stochastic forcing may reduce the predictability of the event if it excites the growth of predictions errors after the forecast is initialized or perturbs the state of the tropical Pacific away from expected ENSO growth. It is, therefore, important to identify specific structures within the noise forcing that are associated with the CP and EP optimals.

Following the methods outlined in Penland and Hartten (2014), we empirically calculate the noise forcing conducive to CP and EP growth directly from observations. We then identify the physical mechanisms within the noise forcing that lead to CP or EP growth. This chapter is organized as follows: Section 3.2 describes the methods to empirically estimate the linear dynamics of the tropical Pacific from observations, the optimal initial conditions that maximize CP and EP growth. Section 3.3 explains the methodology for calculating the noise forcing of the CP and EP optimal initial conditions and presents the structures within the noise forcing that lead to CP and EP growth. Section 3.4 discusses the implications of this methodology. The usefulness of this methodology is demonstrated in Chapter 4, where it is applied to several case studies to analyze the relative roles of noise forcing and deterministic dynamics to ENSO development.

3.2 Data and Methods

3.2.1 Data

The LIM is developed using monthly Optimally Interpolated SST (OISST; Reynolds et al. 2002) in the tropical Pacific [120°:285°E, -25°:25°N] and monthly thermocline depth, calculated as the depth of the 20-degree isotherm (Z20) from the NCEP Global Ocean Data Assimilation System (GODAS; Behringer and Xue 2004), between 120°:285°E and -20°:20°N. The SST and Z20 data, from 1982-2016, are averaged onto 2° latitude by 5° longitude grids. The annual cycle for each data set is removed by subtracting the 1982-2016 monthly climatological mean from each month. The monthly anomalies are then smoothed with a 3-month running mean and de-trended using linear regression.

EOF analysis is applied as a prefilter to the monthly SST and Z20 anomalies. The leading 9 SST EOFs and 3 Z20 EOFs are retained to define the state vector x (Equation 3.3). For reference, the leading two EOFs of SST and Z20 are shown in Figure 3.1a-d. The leading EOF of SST (explains 52.1% of the variance) shows a typical canonical ENSO pattern, while the second EOF (explains 12.1% of the variance) strongly projects onto the SST pattern known as the PMM. For reference, the temporal correlation between the PMM time series and PC2 is .82. Figures Figure 3.1e-f show the SST patterns of CP and EP events based upon the Takahashi et al. (2011) definition (Equation 3.1 and Equation 3.2). These definitions are used in Section 3.2.2 to specify the direction of growth in order to estimate the CP and EP optimal initial conditions.

$$C = (PC1/\sqrt{\lambda_1} + PC2/\sqrt{\lambda_1})/\sqrt{2} \tag{3.1}$$

$$E = (PC1/\sqrt{\lambda_1} - PC2/\sqrt{\lambda_1})/\sqrt{2} \tag{3.2}$$

We define the state vector $\mathbf{x}$ as in Vimont et al. (2014) and Newman et al. (2011) with sea surface temperature (SST) and thermocline depth ($Z20$) as follows:

$$\mathbf{x} = [\mathbf{Z_{SST}}, \mathbf{Z_{Z20}}], \tag{3.3}$$

where Z_{SST} is the leading 9 SST principal components (PCs) (explains 88.1% of the variance) and Z_{Z20} are the leading 3 Z20 PCs (explains 45.8% of the variance). The PC's of the state vector are normalized by the square root of the total variance of the respective field; i.e. Z_{SST} is normalized by the square root of the sum of all SST eigenvalues, and Z_{Z20} is normalized by the square root of the sum of all Z20 eigenvalues.

3.2.2 Linear Inverse Model

LIM approximates the evolution of a dynamical system, in this case the tropical Pacific, by a multivariate linear model as follows (Penland and Sardeshmukh 1995):

$$d\mathbf{x}/\mathbf{dt} = \mathbf{L}\mathbf{x} + \zeta, \tag{3.4}$$

where $\mathbf{x}$ is the state of the system, $\mathbf{L}$ is the dynamical system matrix representing the linear approximation to the dynamics of the system (including the linear approximation

to the nonlinear dynamics), and ζ is the white noise forcing. The dynamical system matrix $\mathbf{L}$ can be empirically estimated from a set of observations as presented below, and an empirical estimation of the noise forcing ζ is presented in Section 3.3.1. Previous studies show the tropical Pacific is well represented by this stochastically forced linear system (Penland and Sardeshmukh 1995; Penland 1996). In this LIM framework, the evolution of the state $\mathbf{x}$ can be described as:

$$\mathbf{x(t)} = \mathbf{e^{L(t-t_0)}x(t_0)} + \int_{\mathbf{t_0}}^{\mathbf{t}} \mathbf{e^{L(t-s)}}\zeta(\mathbf{s})\mathbf{ds}, \tag{3.5}$$

where the first term on the right-hand side of the equation represents the deterministic, or predicable, evolution of the system from time t_0 to t (see, e.g., Chang et al. 2004); the second term represents the non-deterministic, unpredictable, or noise-forced, part of the system [observe that the second term includes the stochastic forcing in (Equation 3.4) convolved with the deterministic dynamical evolution through the remaining forecast time]. If the linear model perfectly represents the system, the second term will be equal to the forecast error.

It can be shown that the correlation between $\mathbf{x(0)}$ and the second term of (Equation 3.5) is zero. Defining the Green's function as the matrix yielding the LIM forecast $\mathbf{x}'(\tau)$ when operated on an initial condition $\mathbf{x(0)}$,

$$\mathbf{x}'(\tau) = \mathbf{e^{L\tau}x(0)} = \mathbf{G}_\tau\mathbf{x(0)}, \tag{3.6}$$

where $\mathbf{x}'(\tau)$ is the forecast of the final state at time τ, $\mathbf{x(0)}$ is the initial state, and G_τ is the 'Green's function' or propagator matrix. From (Equation 3.6), one can derive G_τ

and **L** from the lagged covariance statistics of the system:

$$G_\tau = C_\tau / C_0, \tag{3.7}$$

$$\mathbf{L} = \mathbf{ln}(\mathbf{G}_\tau)/\tau, \tag{3.8}$$

where C_τ is the τ-lag covariance matrix of the state vector x and C_0 is the zero-lag covariance matrix of the state vector x. As previously mentioned, the linear operator **L** governs the deterministic evolution of the system over a specific time period τ.

3.2.3 Optimal Initial Conditions

The noise forcing that will maximize the deterministic growth toward CP or EP events will be the noise that pushes the system toward generating the associated optimal initial conditions. Therefore, we first calculate the optimal initial conditions that maximize either CP or EP growth. Using the previously calculated linear dynamics of the system (Equation 3.8), we are able to determine the initial state that maximizes deterministic growth in a given direction (Penland and Sardeshmukh 1995; Newman et al. 2011a; Vimont et al. 2014). The resulting initial structures are, hereafter, referred to as optimal initial conditions. The optimal initial conditions that maximize growth toward CP and EP final conditions are calculated by following the methodology of Vimont et al. (2014). Based upon the definition of CP and EP events (Equation 3.1 and Equation 3.2), we define the vector coordinate directions for CP and EP events as follows:

$$\mathbf{n_{CP}} = \mathbf{1}/\sqrt{\mathbf{2}\lambda_\mathbf{1}}, \mathbf{1}/\sqrt{\mathbf{2}\lambda_\mathbf{2}}, \mathbf{0}, \mathbf{0}, ..., \tag{3.9}$$

$$\mathbf{n_{EP}} = \mathbf{1}/\sqrt{\mathbf{2}\lambda_\mathbf{1}}, -\mathbf{1}/\sqrt{\mathbf{2}\lambda_\mathbf{2}}, \mathbf{0}, \mathbf{0}, ... \tag{3.10}$$

The CP and EP final norm kernels (N), which define the direction of growth, are defined as:

$$N_{CP} = \mathbf{n_{CP}^T n_{CP}} + \epsilon \mathbf{I} \tag{3.11}$$

$$N_{EP} = \mathbf{n_{EP}^T n_{EP}} + \epsilon \mathbf{I} \tag{3.12}$$

where ϵI is the identity matrix times some arbitrary small number ($\epsilon = 10^{-9}$) that is necessary for numerical stability (Tziperman et al. 2008). Using the CP and EP norms above, we estimate the optimal initial conditions ($\mathbf{p}$) that maximize growth (μ) in the direction of the chosen norm (N) over a finite time period (τ) by solving the generalized eigenvalue problem:

$$G_\tau^T N G_\tau \mathbf{p} - \mu(\tau)\mathbf{p} = \mathbf{0}. \tag{3.13}$$

Figure 3.2a and Figure 3.2c show the optimal initial conditions that maximize either CP or EP growth, respectively, over a 6-month time period. We choose to maximize growth over 6 months (τ = 6mo), although the optimal initial conditions for τ = 3mo and τ = 9mo are very similar. The final CP and EP ENSO states are shown in Figure 3.2b and

Figure 3.2d, respectively. Optimal initial and associated final conditions found here are very similar to those previously calculated in Vimont et al. (2014), however, for consistency, we show the structures again since the LIM in this study is constructed with different SST and thermocline data products Figure 3.2. The optimal initial condition that maximizes CP growth shows a spatial SST structure representative of the PMM and a thermocline structure containing an increased zonal thermocline gradient, with deep thermocline anomalies in the western Pacific and shoaled thermocline anomalies in the eastern Pacific. The EP optimal initial condition contains a zonal SST gradient containing positive SST anomalies located in the far eastern Pacific and negative SST anomalies in the western and central Pacific. The EP optimal also suggests that a deepened thermocline across much of the central equatorial Pacific maximizes EP growth.

The temporal evolution of the L2, CP and EP optimal initial conditions (red lines) together with SST PC1 and the CP and EP indices (black lines) are shown in Figure 3.3a-c. The time series of the optimal initial conditions are calculated by projecting the state vector x onto the L2, CP, or EP optimal initial structures. As expected, the L2, CP, and EP optimal initial time series lead the SST PC1, CP index, and EP index, respectively. The maximum lagged correlation for both CP and EP occurs when the optimal leads the index by two months.

3.3 Noise Forcing of CP and EP Optimals

This section describes the methods used to estimate the noise forcing that pushes the tropical Pacific towards a particular state, in particular the optimal initial condition for CP or EP ENSO events. We then diagnose specific physical mechanisms that contribute to that noise forcing.

3.3.1 Stochastic Noise Forcing

The observed stochastic forcing, or noise forcing, of the system can be estimated using a centered difference approximation to (Equation 3.4) following the methodology described in Penland and Hartten (2014):

$$\zeta(\mathbf{t}) \approx (\mathbf{x}(\mathbf{t}+\delta\mathbf{t}) - \mathbf{x}(\mathbf{t}-\delta\mathbf{t}))/\mathbf{2}\delta\mathbf{t} - \mathbf{Lx} \tag{3.14}$$

where $\mathbf{x}$ is the high frequency state vector based on pentad data and $\mathbf{Lx}$ is the deterministic evolution. Here, we reiterate the cautionary note from Penland and Hartten (2014; Supplementary Material) on the centered difference approximation to the continuous system (Equation 3.4). In a Stratanovich system the contemporaneous correlation between the noise and the system state is non-zero, and the centered difference equation approximation in (Equation 3.14) is only valid in the limit as δt goes to zero. In this case, the approximation is justified if the time scale over which (Equation 3.14) is evaluated is short compared to the time scale of the deterministic evolution of the system. Hence, we evaluate (Equation 3.14) using pentad data. Additionally, the centered differencing approximation required by Stratonovich calculus is consistent the structure of the noise covariance matrix calculated using the noise from (Equation 3.14) to the structure of the noise covariance matrix calculated using the fluctuation-dissipation relationship with stationary statistics (not shown; Penland and Sardeshmukh, 1995).

The rapidly varying state vector x is defined as the projection of the pentad SST and Z20 data onto the leading 9 SST and 3 Z20 EOF structures, that were identified from monthly data in Section 3.2. As before, the modes (9 SST and 3 Z20) of the high frequency state vector x are normalized by the square root of the total variance of their

respective variable's monthly resolved data. SST pentad means are calculated from daily OISST from 1982-2016. Pentad means of the Z20 data are calculated from daily GODAS thermocline depth from 1982-2016 (again, the thermocline depth is calculated as the depth of the 20-degree isotherm). Both SST and Z20 pentad data are averaged onto the same 2° latitude by 5° longitude grid as the monthly data. The annual cycle is removed, the data de-trended and smoothed with a five-pentad running mean (our justification for applying a 5-pentad running mean is explained below in Section 3.3.2).

3.3.2 Noise Structures associated with CP and EP Optimals

The noise forcing associated with the CP or EP optimal initial conditions is estimated by projecting the total noise forcing $\zeta(\mathbf{t})$ (Equation 3.14) onto the spatial structures of the optimals. This generates a time series of stochastic forcing that pushes the system state toward the specified ENSO optimal initial condition. We recognize that this methodology neglects the possibility that the deterministic dynamics play a role in developing the optimal. Figure 3.3d and Figure 3.3e show the time series of noise forcing associated with the CP and EP optimals, respectively. Although LIM assumes the noise forcing will be white in time, spectral analysis of the raw noise forcing for the CP and EP optimals shows the variance for periods shorter than 5 pentads is insignificant (Figure 3.3h, i). The decrease in power at high frequencies is expected due to the centered differencing method used to estimate the noise. Due to this characteristic, we apply a 5-pentad running mean to the SST and Z20 data prior to calculating the noise time series to remove the insignificant variance in the noise.

Figure 3.3f shows the seasonal variance of the total noise forcing. The maximum (minimum) variance in the noise forcing occurs during March (August). Figure 3.3g shows the seasonal variance of the noise forcing time series associated with the L2, CP and EP

optimals plotted in blue, red and black, respectively. The variance was smoothed with successive 5- and 7-pentad centered running means. There is some seasonality in the CP noise variance which is highest during boreal winter (DJF). The EP noise variance, on the other hand, contains much stronger seasonality and is highest during boreal spring (MAM) and lowest during fall (SON). Unlike Penland (1996), we do not see a semi-annual seasonal cycle in the noise variance possibly due to the state vector, the data sets used, or the different methodology. Similar results satisfy the time-dependent fluctuation dissipation relation (not shown).

To identify physical mechanisms within the stochastic forcing that contribute to the development of the CP and EP optimal initial conditions, we regress pentad averaged NCEP reanalysis data onto the stochastic forcing time series associated with the optimals. The resulting regression maps are interpreted as variability in a particular field that covaries with the noise forcing of a given optimal initial condition. Pentad means are calculated from daily NCEP Reanalysis data between 1982 and 2016. The annual cycle is removed and the data de-trended. The anomalous NCEP pentad averaged data is then regressed onto the normalized stochastic forcing time series for CP and EP optimals, respectively.

Figure 3.4 and Figure 3.5 show the structures of atmospheric noise and oceanic forcing by the noise, respectively. Figure 3.4 shows regression maps of seasonal sea level pressure (SLP), 850mb wind, and outgoing longwave radiation (OLR) regressed on the noise forcing time series associated with the 6-month CP and EP optimal initial conditions (left and right columns; respectively). Figure 3.5 shows regression maps of seasonal ocean-atmosphere flux (OAFLUX; defined as the sum of sensible heat flux and latent heat flux) and surface wind stress regressed on the noise forcing time series associated with the 6-month CP and EP optimal initial conditions (left and right columns; respectively). It

is worth pointing out that the maps in Figure 3.4 and Figure 3.5 contain a large range of variability, which is not surprising considering that "noise forcing" could include a variety of phenomena.

The CP SLP structures (Figure 3.4; left column) are somewhat seasonally dependent, with the winter hemisphere slightly dominating (in amplitude) the stochastic forcing. Additionally, the CP SLP forcing structures during boreal fall (SON), winter (DJF) and spring (MAM) show a northern hemisphere SLP pattern recognizable as the North Pacific Oscillation. The OAFLUX (Figure 3.5; left column) during these seasons shows a flux into the ocean with a pattern that resembles the PMM. These results support previous studies which show the NPO and PMM is related to the development of CP ENSO events (Yu and Kim 2011; Kim et al. 2012b). The 850mb wind structures (Figure 3.4, left column) are consistent with the SLP patterns. The SLP maps also include structures in the southern hemisphere, most notably anomalous low pressure in the subtropics (around 30°S) throughout the year. These anomalies are associated with only weak downward heat flux anomalies (Figure 3.5; left column).

In contrast to the coherent SLP structures associated with CP noise forcing, the seasonal patterns of SLP stochastic forcing associated with the EP optimal show less influence from the northern hemisphere, although important structures are located in the Southern Hemisphere throughout the year (Figure 3.4; right column). In particular, a dipolar SLP structure is evident during austral fall (MAM) and spring (SON) that resembles the "South Pacific Oscillation" identified as an EP ENSO precursor by You and Furtado (2017). Similar SLP patterns are also found in Penland and Matrosova (2008). The 850mb wind (Figure 3.4; right column) and surface wind stress (Figure 3.5; right column) patterns show positive zonal wind anomalies in the equatorial Pacific throughout the year, although there are slight seasonal differences in the location and magnitude. The zonal

winds lie south of the equator in the western tropical Pacific during DJF, centered close to the equator during MAM and JJA, and north of the equator in the western tropical Pacific during SON. The wind anomalies are weakest during boreal summer (JJA). Since the EP noise variance peaks in boreal spring (MAM; Figure 3.3f), the springtime noise structures are of interest. The springtime (MAM) stochastic forcing of EP optimals show strong low level zonal wind anomalies in the western and central tropical Pacific (Figure 3.4; right column). Interestingly, the ocean-atmosphere flux shows a flux into the ocean in the southern hemisphere off the coast of South America from DJF through JJA (Figure 3.5; right column).

The importance of the noise structures associated with either CP or EP optimal initial conditions will be addressed in the ENSO case studies in Chapter 4.

3.4 Conclusions

This chapter investigates the role of noise in producing ENSO events with eastern Pacific (EP) or central Pacific (CP) characteristics. A forecast perspective is applied using linear inverse modeling (LIM) to separate the deterministic evolution of the tropical ocean / atmosphere system from the noise-forced non-deterministic evolution. In this forecast framework, the noise plays two roles: it can enhance deterministic growth by generating initial conditions with large projection onto optimal initial states, or it can lead to non-deterministic growth (forecast error) by pushing the system away from the deterministic trajectory. While many studies have used LIM to identify optimal initial conditions for EP and CP events, the noise forcing that excites those optimal structures has not been previously identified. This study uses a LIM framework to identify specific noise structures capable of exciting CP and EP optimal initial conditions.

We first use LIM to calculate the linear dynamics of the tropical Pacific and identify the optimal initial conditions that maximize growth towards EP and CP events. We then apply a centered differencing method (Penland and Hartten 2014) to calculate the noise forcing of the tropical Pacific. By projecting the noise forcing onto the CP and EP optimal initial conditions we obtain time series of how the noise pushes the system toward CP or EP optimal initial conditions. These time series are then used to investigate other fields to better understand the structures within the noise forcing that are responsible for generating CP and EP growth.

Prior studies show the importance of extratropical atmospheric forcing and the seasonal footprinting mechanism in the development of CP ENSO events (Yu and Kim 2011). The PMM structure of the CP optimal initial conditions found in this study as well as the corresponding NPO structure of the boreal winter stochastic forcing provide direct empirical evidence in support of these findings. Further, the EP noise forcing identifies equatorial westerly wind activity near 150°E, and the South Pacific Oscillation (SPO; You and Furtado, 2017) as contributors to optimal EP initial conditions.

The technique used in this study contains limitations. For example, LIM uses a linear estimation of the non-linear dynamics. Although we performed tests to check the validity of LIM in the tropical Pacific and previous studies show LIM performs well in the tropical Pacific (e.g. Penland and Sardeshmukh 1995; Newman et al. 2011), it is possible the linear approximation fails to capture some non-linear dynamics properly. Chapter 5 and 6 calculate comparable result in the CESM and test the influence of the noise forcing structures in a coupled general circulation model.

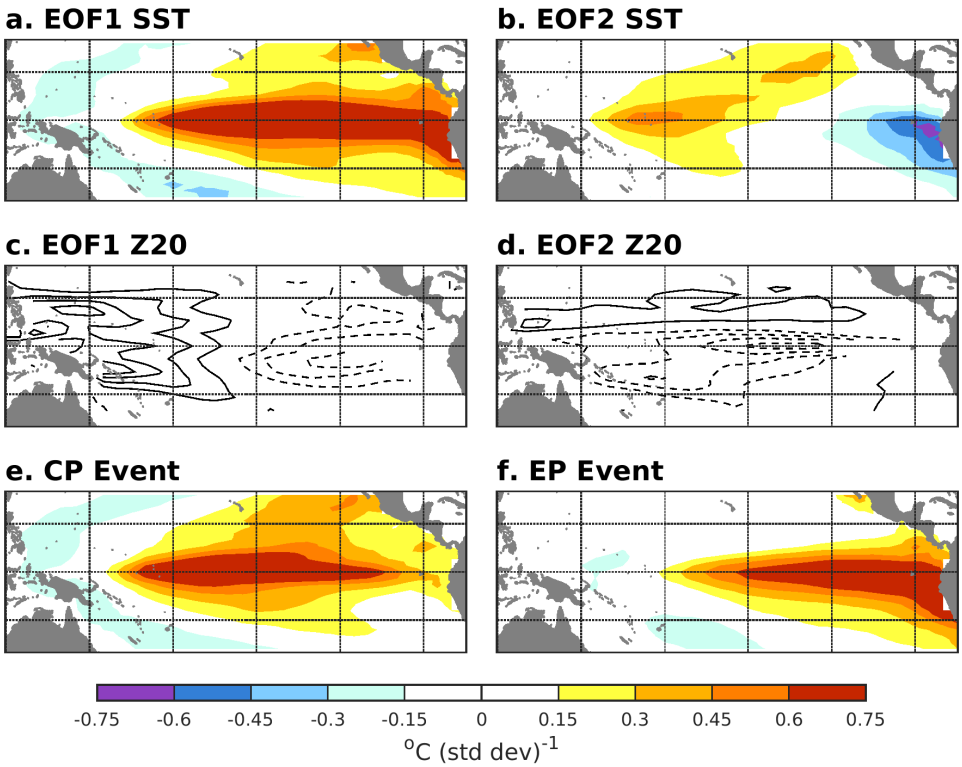

FIGURE 3.1: Leading two EOF patterns of SST(a, b), thermocline depth (c, d), and the defined spatial structure of CP and EP events (e and f; respectively).

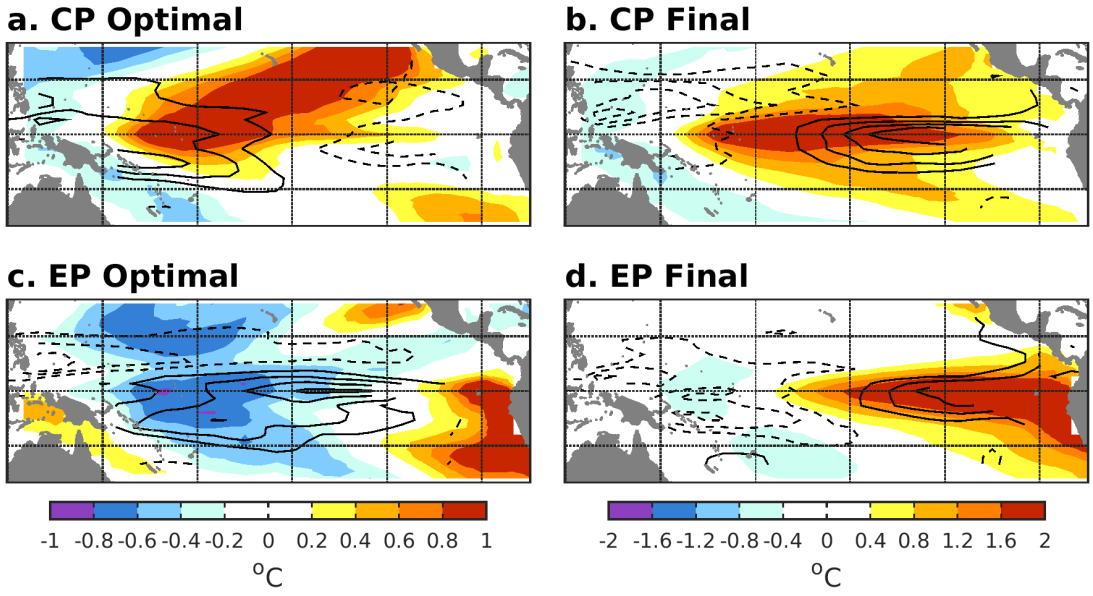

FIGURE 3.2: SST (°C; shading) and thermocline depth (m; black contours) for $\tau = 6$ mo CP and EP optimal initial conditions (a,c) and final states (b,d). SST contour interval is .4°C for the optimals and .8°C for the final conditions. Thermocline depth contour interval is 4m for the optimals and 8m for the final conditions. Positive (negative) thermocline depth anomalies correspond to solid (dashed) contours. The zero contour has been omitted.

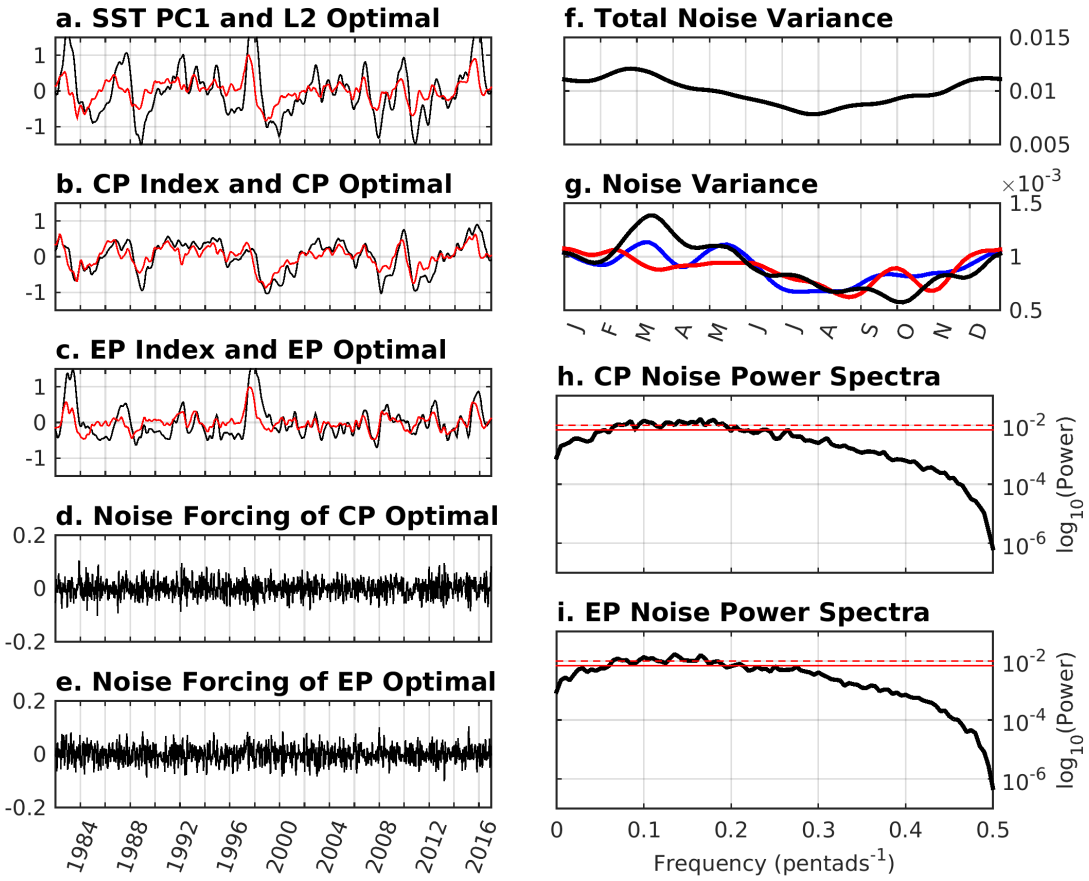

FIGURE 3.3: The temporal evolution of a) SST PC1 (black) and L2 optimal initial conditions (red), b) CP Index (black) and CP optimal initial conditions (red) and c) EP Index (black) and EP optimal initial conditions (red). The noise forcing time series associated with 6-month CP and EP optimal initial conditions shown in d) and e), respectively. The CP and EP noise forcing time series (d, e) are calculated as the projection of $\zeta(t)$ (Equation 3.14) onto the CP or EP optimal initial conditions (Figure 3.2). The seasonal variance of the total noise forcing $\zeta(t)$ is shown in f) while g) shows the seasonal variance of the noise forcing associated with the L2 (blue), CP (red), and EP (black) optimals. The variance is smoothed with successive 5-pentad and 7-pentad running means. H) and i) show the power spectra (solid black) of the unfiltered CP and EP noise forcing time series, respectively. The solid red lines show the white noise null hypothesis, while the dashed red lines show the 95% confidence interval.

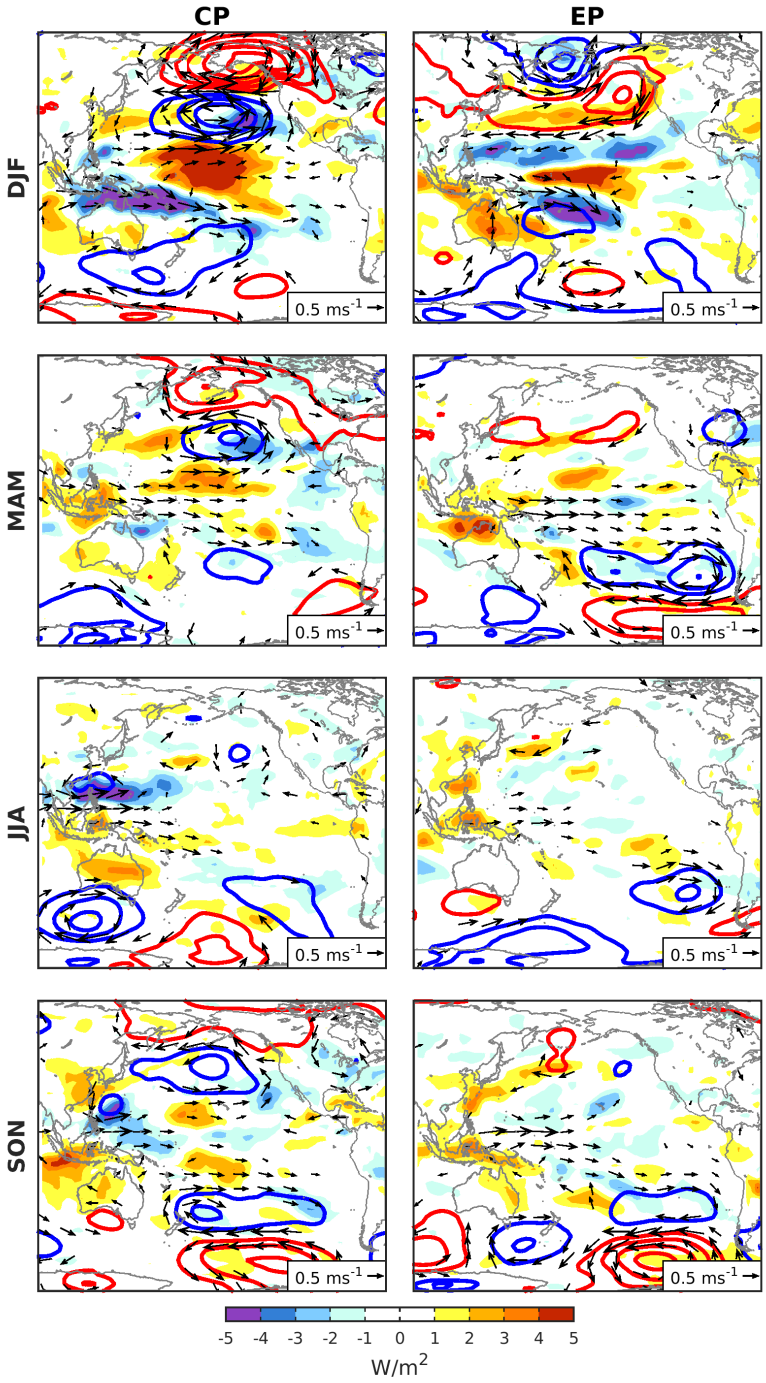

FIGURE 3.4: Atmospheric noise structures associated with Central Pacific and Eastern Pacific optimal initial conditions (left and right columns, respectively). Shown are the seasonal regression coefficients between sea level pressure (SLP; hPa; contours), 850mb wind (m/s; vectors), and outgoing longwave radiation flux (OLR; W/m2; shading) and the noise forcing time series of CP or EP optimal initial conditions. The first row shows the regression coefficients of boreal winter (DJF). The second through fourth rows show the regression coefficients for boreal spring (MAM), summer (JJA) and fall (SON) months, respectively. Positive (negative) SLP indicated with red (blue) contours where the contour interval is every 0.5 hPa. The zero contour has been omitted. OLR is defined as positive upwards. Wind vectors are only shown where the geometric sum of the correlation coefficients is equal to or greater than .1.

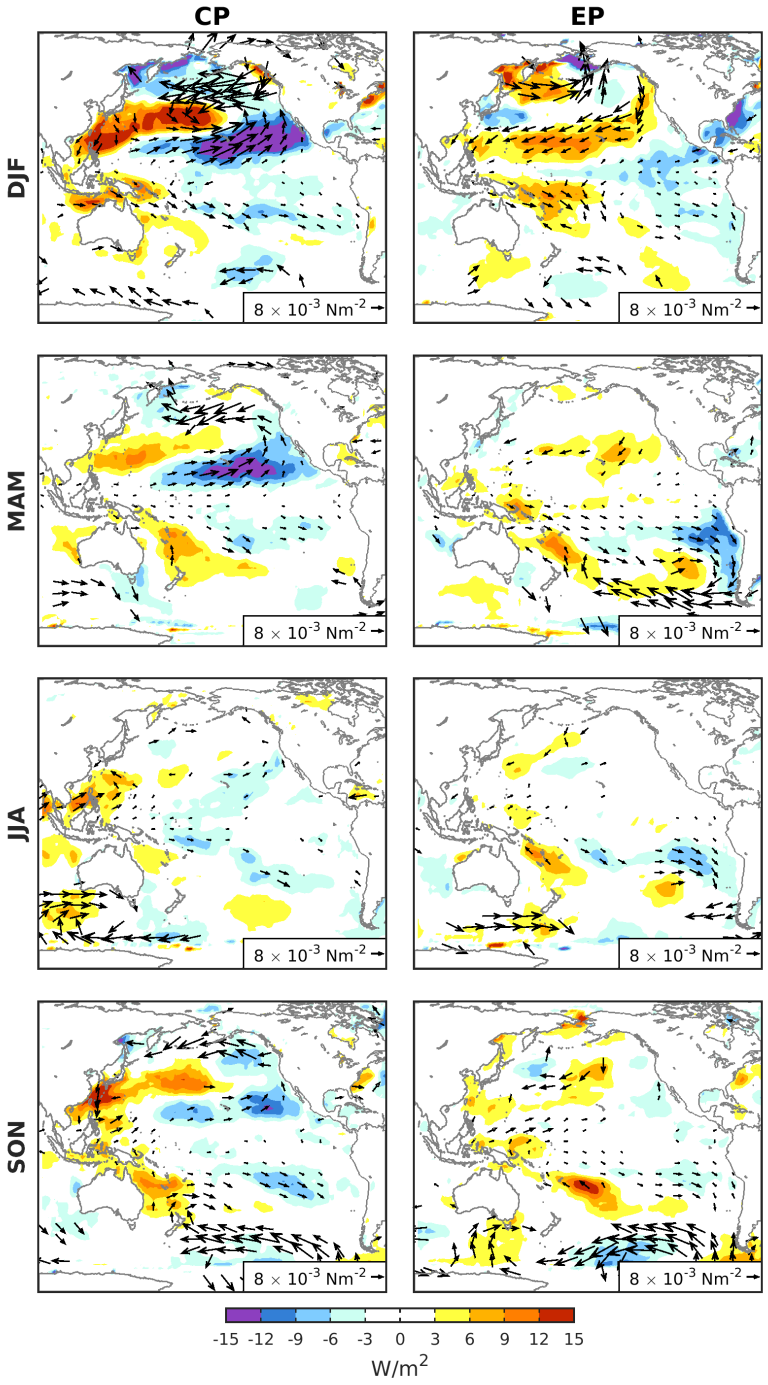

FIGURE 3.5: Noise Forced oceanic structures associated with Central Pacific and Eastern Pacific optimal initial conditions (left and right columns, respectively). Shown are the seasonal regression coefficients between surface wind stress (N/m2; vectors) and ocean-atmosphere flux (OAFLUX; W/m2; shading) and the noise forcing time series of CP or EP optimal initial conditions. The first row shows the regression coefficients of boreal winter (DJF). The second through fourth rows show the regression coefficients for boreal spring (MAM), summer (JJA) and fall (SON) months, respectively. OAFLUX is defined as positive upwards. Wind stress vectors only shown where the geometric sum of the correlation coefficients is equal to or greater than .1.

Chapter 4

The Role of Stochastic Forcing in generating ENSO Diversity in Observations: Application of Methods

A subset of the content of this chapter has been accepted with revisions to the *Journal of Climate* as Thomas, E. E., et al.: The Role of Stochastic Forcing in generating ENSO Diversity, *In Review*.

4.1 Introduction

Under the framework presented in Chapter 3, it is possible noise forcing can excite CP or EP optimal initial conditions that enhance deterministic growth, and thus improve the predictability of an event. However, the same stochastic forcing may reduce the

predictability of the event if it excites the growth of predictions errors after the forecast is initialized or perturbs the state of the tropical Pacific away from expected ENSO growth. In this chapter, we apply the LIM framework to several past ENSO events in order to analyze the relative roles of the initial conditions and deterministic dynamics as well as noise forcing throughout the evolution of individual ENSO events. We estimate the role of noise forcing during the 1982/1983, 1997/1998 EP ENSO events, the 2009/10 CP ENSO event, the 2015-2016 ENSO event, and the 'failed' event of 2014. The implications for CP and EP ENSO predictability will be discussed.

This chapter is organized as follows: Section 2 presents the methods, sections 3-7 present the results from each of the five ENSO case studies, and section 8 discusses the conclusions.

4.2 Methods

Previously, we identified the structures in the noise that push the system towards some optimal initial condition. The optimal initial condition is defined to maximize the deterministic growth [first term on the right-hand side of (Equation 3.5)] towards either a CP or EP event over some time period. In this section, we investigate the role of initial conditions in the deterministic evolution, and the ensuing noise forcing in the non-deterministic evolution of specific ENSO events. We note that the non-deterministic evolution of the system is controlled by the second term in (Equation 3.5). Chang et al. (2004) show that the forcing structure that optimizes error growth over a finite time period from time 0 to τ is obtained as the eigenvector of $B(\tau)$ where:

$$B(\tau) = \int_{\mathbf{0}}^{\tau} \mathbf{e}^{\mathbf{L}^*(\tau-\mathbf{s})}\mathbf{e}^{\mathbf{L}(\tau-\mathbf{s})}\mathbf{ds} \tag{4.1}$$

Here, we investigate the role of noise throughout the evolution of a forecast period.

It is worth noting the relationship between the initial optimals investigated in Section 3.2 and the noise structures that dominate the non-deterministic trajectory. At a given time τ' after the forecast initialization but before a forecast target end time τ, the relationship between the initial optimals and the optimal noise structure can be illuminated by writing (Equation 4.1) as an infinite sum:

$$B(\tau) = \lim [\sum_{\mathbf{k=1}}^{\mathbf{n}} \mathbf{e}^{\mathbf{L}^*(\tau-\kappa\delta\mathbf{s})}\mathbf{e}^{\mathbf{L}(\tau-\kappa\delta\mathbf{s})}\delta\mathbf{s}] \tag{4.2}$$

(where $\delta s = \tau/\mathbf{n}$). Note that at time τ' the argument inside the sum is simply ${G_{\tau-\tau'}}^T G_{\tau-\tau'}$. Hence, the structure that optimally pushes a system away from its trajectory at time τ' between 0 and τ is simply the optimal initial condition at time $\tau - \tau'$. This result is the intuitive statement that at some time τ' after the forecast initialization, the noise structure that optimally ruins a forecast is that which experiences the most transient growth over the remaining forecast time ($\tau - \tau'$). This argument can easily be generalized to investigate growth toward or away from specific norms, and is used to investigate the role of noise forcing in the generation of ENSO events with specific CP or EP characteristics herein. As the optimal initial conditions for 3, 6, and 9mo lags were similar in spatial structure, we use the 6mo optimal initial structure for analysis herein.

We use the LIM to characterize the role of noise forcing during past ENSO events to highlight how the role of the noise forcing can vary for any given event. We select two strong EP events (1982/1983 and 1997/1998), one strong CP event (2009/2010), the recent 2015/2016 event (which displays both CP and EP characteristics) as well as the 'failed' forecast of a 2014 event. The LIM framework allows us to use forecasts as a

diagnostic tool to compare the relative role of the noise forcing, or the unpredictable component, to the deterministic, or the predictable, component of the system for the generation of any given event. Here we briefly describe the methodology used to analyze each event.

The relative role of (i) initial conditions vs. (ii) stochastic forcing is evaluated by running the LIM forward in time with either the (i) deterministic component only [first term on the right-hand side of (Equation 3.5)], or with (ii) the stochastic noise component only [second term on the right-hand side of (Equation 3.5)]. Comparing the observed SST anomalies with (i) the SST predicted by the deterministic component or (ii) the noise forced SST evolution allows us to estimate the relative importance of the noise forcing and deterministic dynamics, or predictable component, for any given event. Note that since the noise forcing in this study is calculated as a residual, by definition, it contains influences from both the stochastic noise forcing as well as non-linearities not captured by the linear approximation to non-linear dynamics. The importance of timing for initial conditions and noise forcing is inferred through initializing the LIM (using the two terms above) from different months, determined as the pentad containing the first day of the respective month.

The LIM framework also allows us to determine the relative roles of CP and EP noise forcing to each event. Similar to the method described above, we run the LIM forward in time using staggered initial conditions. However, by systematically removing the noise that projects onto either the CP or EP optimal, and comparing the resulting SST forecast to the observed SST anomalies we can determine the importance of CP or EP noise forcing in generating the observed ENSO characteristics. We then quantify how well the LIM without the CP or EP noise forcing reproduces the observed SST by calculating the root mean square error ($RMSE$) of the CP index and EP index as follows:

$$RMSE = \sqrt{\sum_{i=1}^{n} (X_{LIM} - X_{Obs})^2 / n} \tag{4.3}$$

where X_{LIM} is the CP or EP index (Equations 3.1 and 3.2) for the LIM SST forecast without CP or EP noise forcing, respectively, X_{Obs} is the CP or EP index of the observed SST, and n is the number of pentads. The RMSE is calculated between the initialization (the first pentad of each month) through the last pentad of the February following the peak of the event. We use both CP and EP indices rather than a single ENSO index (such as the Niño3.4 index) in order to capture the importance of the CP and EP noise forcing to generating strong EP and CP spatial characteristics. It is important to note, however, that any given ENSO event may be influenced by stochastic forcing that is characterized by a combination, or complete lack of, CP and EP forcing.

4.3 1982/1983 El Niño Event

We first analyze the tropical Pacific SST anomalies from the 1982/1983 ENSO event. The Hovmöller diagrams in Figure 4.1 show the observed equatorial SST anomalies of the event (top left) and various LIM simulations of the SST anomalies. The remainder of the top row shows the full LIM simulation [calculated using both terms on the right-hand side of Equation 3.5] which match the observations well no matter when the model is initialized, as expected [this also serves as a check on the centered differencing in Equation 3.14]. The middle row shows the SST anomalies due to the deterministic, or predictable component of the LIM [first term on the right-hand side of Equation 3.5] while the bottom row shows the unpredictable, or noise forced component, of the SST anomalies [second term on the right-hand side of Equation 3.5], as explained above. By definition, the dynamical SST anomalies plus the noise forced SST anomalies equals the

SST anomalies produced by the full LIM (i.e. top row = middle row + bottom row). The label at the very top of each column indicates the month the LIM is initialized; the LIM is initialized with observations from the first pentad of the month. The timing of the initialization is indicated in the Hovmöller diagrams with the horizontal black lines, time increases on the y-axis and longitude (°E) is indicated on the x-axis.

Figure 4.1 indicates that deterministic dynamics do a poor job at reproducing the observed SST anomalies for the 1982/1983 ENSO event prior to October initial conditions; instead, noise forcing dominates. Only when the model is initialized in October or later does the dynamical forecast reproduce the peak amplitude of the 1982/1983 ENSO event. This suggests the state of the system in October, once the ENSO event has begun, is sufficient for generating a skillful dynamical forecast of the ENSO event, while the state of the tropical Pacific prior to October was insufficient to generate a strong ENSO event without the influence of stochastic forcing. More specifically, these results suggest the noise forcing that occurs after the August initialization but prior to the October initialization is critical for producing the October conditions that generate the large amplitude SST anomalies at the peak of the 1982/1983 ENSO event. Furthermore, once the deterministic dynamics begin to dominate the ENSO development in boreal fall, they also dominate the development of the La Niña that occurs the following boreal winter. This shows that the 1983/1984 La Niña was a result of deterministic evolution from El Niño conditions in late 1982.

To determine whether the CP or EP noise forcing is more important for the generation of the 1982/1983 event, we repeat the LIM simulations, except that we systematically remove the CP or EP noise forcing from the LIM and calculate the RMSE of the CP and EP index of the resulting SST 'forecast'. These results are summarized in the RMSE calculations for the 1982/1983 event shown in Figure 4.2a. The red +'s show the CP index

RMSE of the LIM run without CP noise forcing, while the black x's represent the EP index RMSE of the LIM run without EP noise forcing. The large EP index errors suggest EP noise forcing is critical to the development of the strong EP characteristics observed during the 1982/1983 event while CP noise forcing is much less influential (indicated by small RMSE values for the CP index). These results also show the noise forcing is particularly important during boreal spring and summer. However, the magnitude of the EP errors decreases dramatically when the LIM is initialized in late summer/fall which supports the previous conclusions that the state of the system during fall is sufficient to develop into an ENSO event through deterministic dynamics alone, while the noise forcing during boreal spring and summer is necessary to generate those conditions.

Finally, we analyze the structures of atmospheric noise forcing during the key months identified above for the development of the 1982/1983 EP El Niño. Uncoupled noise structures in fields that are not included in the state vector are identified by a full multiple linear regression of pentad data onto the PC noise time series. Composites of the resulting noise are then presented for specific months. Figure 4.3 shows the monthly mean, uncoupled SLP (contours), 850mb wind (vectors), and OAFLUX (shading) anomalies for July through October 1982. Since October 1982 initial conditions are sufficient for generating ENSO growth through deterministic dynamics alone, we primarily focus on the stochastic forcing patterns in the months prior to October. The July, August, and September noise patterns show strong positive zonal wind anomalies located in the western equatorial Pacific. These zonal wind anomalies extend across much of the equatorial Pacific during September 1982. These westerly wind structures also match the EP noise forcing patterns seen in JJA and SON in Figure 3.4. Note that our calculation of the noise forcing in (Equation 3.14) assumes that unresolved nonlinearity may be treated as white noise, although it is easy to adjust this term to account for red noise.

4.4 1997/1998 El Niño Event

We next analyze the atmospheric noise patterns that occurs during the development of the 1997/1998 EP El Niño. Figure 4.4 shows the same LIM simulations as in Figure 4.1, except for the 1997/1998 El Niño. Unlike the 1982/1983 EP event which appears to have been largely influenced by noise forcing in late boreal summer, the Hovmöller diagrams in Figure 4.4 show that the deterministic dynamics of the LIM reproduce the observed evolution of the 1997/1998 El Niño more accurately from much earlier initializations. This agrees with previous studies that also show a relatively long predictability of the 1997/1998 event (Newman and Sardeshmukh 2017). Our results show this is especially true when the LIM is initialized in June or later. Indeed, beyond June the noise forcing has little to no effect on the amplitude of equatorial SST anomalies during the ensuing El Niño, though they do contribute to a more rapid decay of the event and transition toward the 1998/1999 La Niña.

Next, we determine if the noise forcing of the 1997/1998 event is dominated by CP or EP noise. These results are shown in Figure 4.2b which shows the RMSE of the CP and EP index from the LIM forecasts without CP or EP noise forcing, respectively. Again, the RMSE is calculated from the model initialization date through the end of the February following the peak of the warming. The LIM without CP noise forcing reproduces the observed event well as indicated by the small magnitudes of the CP index RMSE (Figure 4.2b; red +'s) indicating CP noise forcing is not important in the development of the 1997/1998 event. EP noise forcing, on the other hand, appears to be much more important to the development of the event, especially early in the year. The large RMSE of the EP index for the LIM forecast without EP noise forcing (Figure 4.2b; black x's) through May 1997 shows the importance of EP noise forcing early in the year, however,

the magnitude of the errors decreases drastically beginning in early boreal summer. The sharp decrease in RMSE that occurs after May 1997 indicates the EP noise during boreal spring is important for generating a state where deterministic dynamics dominate the event development.

Figure 4.5 shows the monthly mean uncoupled SLP, 850mb wind, and OAFLUX noise patterns associated with the development of the 1997/1998 event, focusing on March through June 1997 in accord with the RMSE results above. The noise forcing shows strong westerly wind anomalies located along the equator in the central Pacific, during March and April of 1997 which match the boreal spring (MAM) EP noise forcing structures in Figure 3.4. These results indicate that EP noise forcing, particularly the positive zonal wind anomalies located in the equatorial Pacific early in the year, was important for the observed magnitude and strong eastern Pacific characteristics of the 1997/1998 ENSO event. In contrast to the 1982/1983 EP El Niño, this noise forcing occurred much earlier, and hence the 1997/1998 EP El Niño was predictable with a longer lead time.

4.5 2009/2010 El Niño Event

Figure 4.6 shows the role of deterministic dynamics versus noise forcing though Hovmöller diagrams for the 2009/2010 CP ENSO event, as before. For any lead time the deterministic dynamics do a poor job at reproducing the observed warming while the noise forcing dominates the development of the event. This shows the importance of noise forcing to the development of the 2009/2010 CP event and its low predictability skill. Additionally, these results show, unlike the deterministic development of the La Niña events that occur after the strong EP events described above, the La Niña that peaks during the boreal winter of 2010/11 is primarily driven by noise forcing, even after the peak of the 2009/2010 El Niño.

To identify the relative importance of EP and CP noise forcing to the 2009/2010 CP El Niño and determine which months the noise forcing is most important, we calculate the CP and EP index RMSE of the LIM forecasts run without CP and EP noise forcing, respectively (Figure 4.2c). The low RMSE values of the EP index (black x's) indicates the LIM run without EP forcing has very little influence on the resulting SST patterns, indicating the 2010 CP event was not highly influenced by EP noise forcing. However, the LIM is unable to accurately reproduce the observed event when the CP noise forcing is removed from the model, especially when the model is initialized prior to June 2009.

The monthly mean structures of the uncoupled SLP, 850mb wind, and OAFLUX noise that occurs between March and June of 2009 are shown in Figure 4.7. The SLP patterns show slight NPO-like SLP anomalies located in the north central Pacific, which match the CP noise forcing structures seen in Figure 3.4. The dipole SLP structure associated with the NPO is most apparent during April and May, however, the negative SLP anomaly located in the central north Pacific around 40°N is evident in all four months. The 850mb wind structures show extra-tropical wind anomalies associated with the SLP patterns, as expected. March and April also show strong positive zonal wind anomalies located along the equator in the central Pacific. These zonal wind patterns closely match the CP noise forcing structures shown in Figure 3.4. Finally, the OAFLUX patterns include downward heat flux anomalies in the subtropics, which project strongly onto the PMM spatial structure. These OAFLUX patterns also agree with the CP noise forcing structures in Figure 3.5.

4.6 2015/2016 El Niño Event

Figure 4.8 shows the same analysis applied to the strong 2015/2016 El Niño. Results show that deterministic dynamics simulated the evolution of the 2015/2016 event well

with very long lead times. More specifically, these results show that the deterministic dynamics predict a large El Niño in early boreal Spring, and capture the full amplitude of the ensuing event late boreal summer (August). The noise forcing appears to be especially important during February, 2015, and again in July and August, 2015, in generating the large magnitude ENSO event that was observed.

Figure 4.2d. shows the RMSE results to quantify the importance of CP noise forcing vs EP noise forcing to the 2015/1016 CP event. These results show small RMSE for both the CP and EP index, except during February and March of 2015, which contain relatively large EP errors. The monthly composite SLP, 850mb wind, and OAFLUX noise forcing structures for February through May 2015 are shown in Figure 4.9. The most striking noise forcing features are the large zonal wind anomalies that occur in the western and central Equatorial Pacific during February and March. These zonal wind anomalies strongly resemble the MAM EP noise forcing patterns identified in Figure 3.4. The southern hemisphere SLP, zonal wind and OAFLUX anomalies in March all strongly resemble the South Pacific Oscillation of You and Furtado (2017), which is also evident in Figure 3.4. The monthly composites also show noise patterns that project onto the previously identified CP noise forcing patterns in Figures 3.4 and 3.5. For example, the OAFLUX during February contains a flux into the ocean that resembles the PMM pattern seen in Figure 3.5 (left column).

These results show the 2015 ENSO event was largely predictable in nature, due to the dominant role the deterministic component of the LIM played in the forecast. Furthermore, this event highlights the diversity of the noise forcing for any given event. The 2015 event is difficult to classify as either a CP or EP event as there is a significant projection onto both CP and EP patterns (refer to the CP and EP index time series in Figure 3.3b

and c, respectively). This blend of CP and EP characteristics is apparent in the influence of both CP and EP noise forcing structures.

4.7 2014 Non-Event

Finally, we analyze 2014 to see if the ENSO event that many expected to occur at the end of 2014 was 'ruined' by the role of the noise forcing. Most noteworthy, our results suggest no event should have been expected during 2014. The deterministic dynamics, or the predicable component of the LIM, do not forecast an El Niño occurring at the end of the 2014 calendar year, no matter when the model is initialized (Figure 4.10). This suggests the state of the tropical Pacific during 2014 did not contain initial SST and thermocline conditions ideal for producing an ENSO event. Although the monthly noise composites (Figure 4.11) do show easterly wind burst activity during June and July of 2014, which stalled the development of a 2014 El Niño event according to Hu and Federov (2016, 2017), the lack of an ENSO event generated by the deterministic forecast using June initial conditions suggests the WWB noise forcing seen in February and March were insufficient to generate a state that could develop into an event at the end of the year.

4.8 Conclusions

The LIM framework presented in Chapter 3 is used to investigate the relative roles of initial conditions vs. stochastic forcing in the evolution of specific ENSO events. We analyze the role of noise forcing during the 1982/1983, 1997/1998 EP ENSO events, the 2009/2010 CP ENSO event, the 2015/2016 event and 2014 conditions. The LIM is integrated forward from specific times along (i) a deterministic trajectory in which initial conditions are integrated forward with zero noise forcing, and (ii) a non-deterministic trajectory in which initial conditions are set to zero and the LIM is integrated forward

using only the estimated noise forcing. The technique accurately captures diversity in timing and spatial structure of noise forcing although the noise forcing is convolved with the estimated deterministic dynamics.

Diversity in timing of initial conditions and noise forcing is especially evident in comparing the 1982/1983 and 1997/1997 EP El Niño events. Results show that positive zonal wind anomalies play a significant role during the development of both the 1982/1983 and 1997/1998 EP ENSO events, although the two events evolve under very different conditions. Additionally, the large amplitude of the 1982/1983 event was caused by strong equatorial wind anomalies in late boreal summer (August and September). Prior to October initialization, the state of the tropical Pacific was not conducive to producing a large event via this LIM deterministic trajectory. In contrast, the deterministic trajectory for the 1997/1998 El Niño event was predictable using observed initial conditions as early as late winter 1997 (February). Large equatorial westerly wind anomalies in March and April 1997 established a tropical Pacific state that was sufficient for producing a large amplitude El Niño event by late 1997. Beyond May, 1997, noise forcing played very little role in the evolution of the 1997/1998 El Niño event. Further, the following La Niña conditions (1983/1984 and 1998/1999) are shown to largely result from the dynamical evolution of the system from their preceding El Niño events.

Analysis of the 2009/2010 CP ENSO event highlights the role of the stochastic forcing in producing some ENSO events. The 2009/2010 event was largely noise-driven throughout the entirety of the event. Only in the late boreal Fall of 2009 did the deterministic trajectory capture the amplitude of the event. CP noise forcing during April and May, 2009, was especially important for the development of CP characteristics for the resulting event. Further, unlike the 1983/1984 and 1998/1999 La Niña conditions, the 2010/2011

La Niña event was almost entirely driven by noise forcing after the peak of the 2009/2010 El Niño event.

Not all events evolve along CP or EP trajectories, as evidenced by the 2015/2016 event. Strong EP forcing (especially equatorial westerly winds) in February and March of 2015 was especially important for setting the stage for the ensuing event. Analysis shows that the 2014 non-event was relatively well predicted by the deterministic trajectory throughout 2014 indicating the equatorial westerly winds observed early in the season had little influence on any potential ENSO development.

While the present study highlights a few interesting case studies, overall, the results confirm that ENSO events are influenced by a rich variety of phenomena that can influence the event throughout its entire evolution. Further, these noise structures themselves are a blend of a variety of phenomena that can excite ENSO growth in the tropical Pacific. While the role of noise forcing for ENSO development varies greatly for each event and characterizing the structures within the noise forcing is challenging, the present study provides a single framework for parsing through the myriad processes that contribute to ENSO diversity.

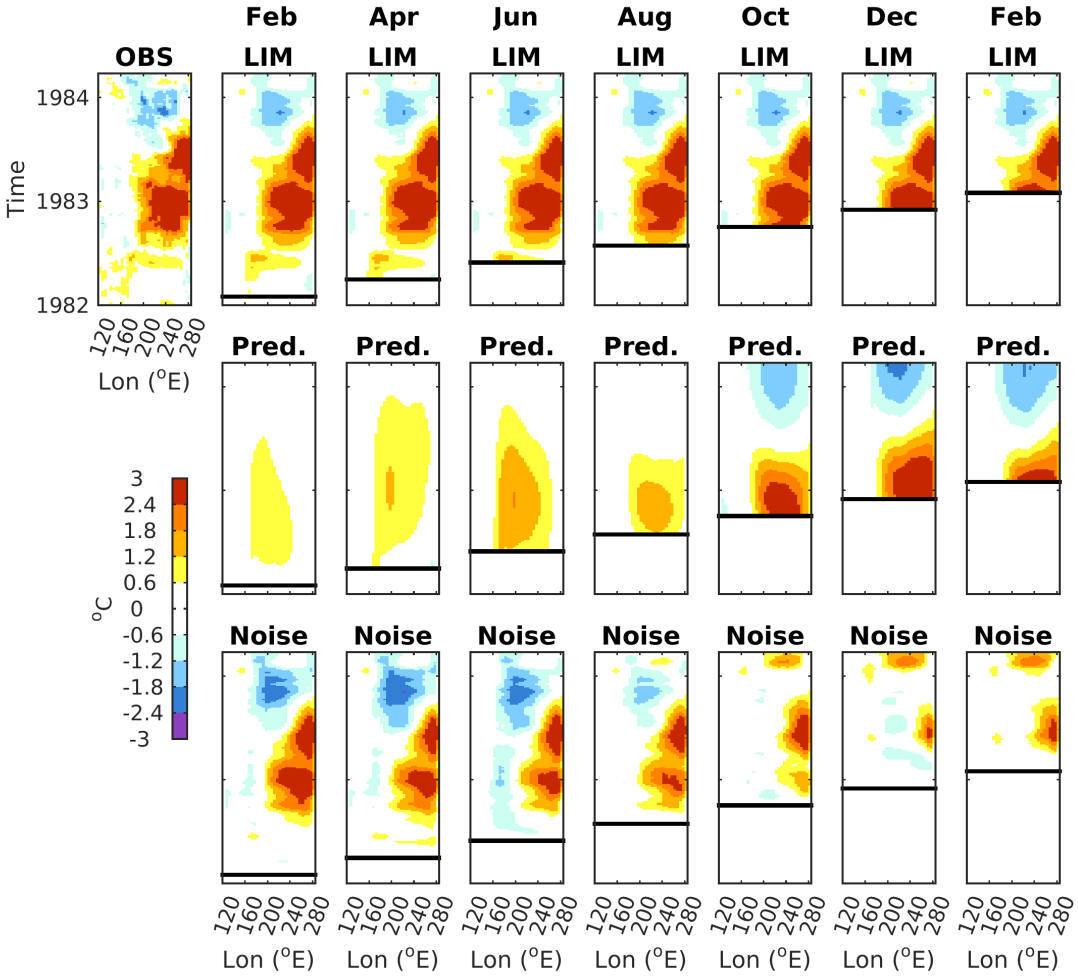

FIGURE 4.1: Hovmöller Diagrams of Equatorial Pacific (120°E:285°E) SST (averaged from 2°S:2°N) for the 1982/83 ENSO event. Time increases upwards on the y-axis and longitude (°E) is indicated on the x-axis. The observed SST anomalies are shown in top left figure. The reminder of the top row shows the SST anomalies predicted from the full LIM containing both deterministic dynamics and stochastic forcing [Calculated using both term on the right-hand side of Equation 3.5]. The second row shows the portion of SST anomalies predicted by the deterministic dynamical component [first term on the right-hand side of Equation 3.5]. The bottom row shows the component of SST anomalies driven by the stochastic forcing term (second term on right-hand side of Equation 3.5]. The columns represent initializations every two months between February 1982 and February 1983. The LIM is initialized using observations during the first pentad of the indicated month. The month of initialization is listed at the very top of each column and is indicated by the horizontal black lines in the diagrams.

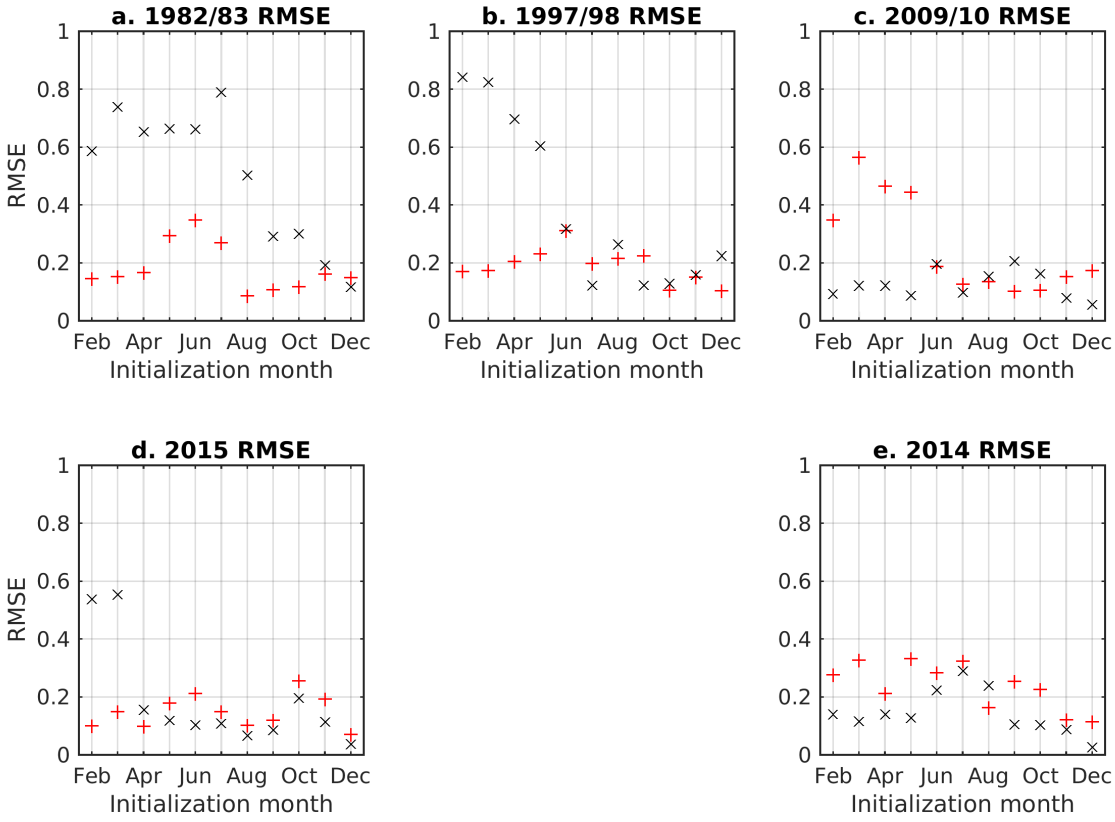

FIGURE 4.2: Root mean square errors (RMSE) calculated for CP (red +) and EP (black x) index for the LIM forecasts containing no CP or EP noise forcing, respectively. The RMSE is calculated between the initialization month (indicated on x axis) through the end of the February following the peak of the event for the a) 1982/1983, b) 1997/1998, c) 2009/2010, d) 2015 El Niño events. The RMSE values for the 'failed' 2014 event are shown in e).

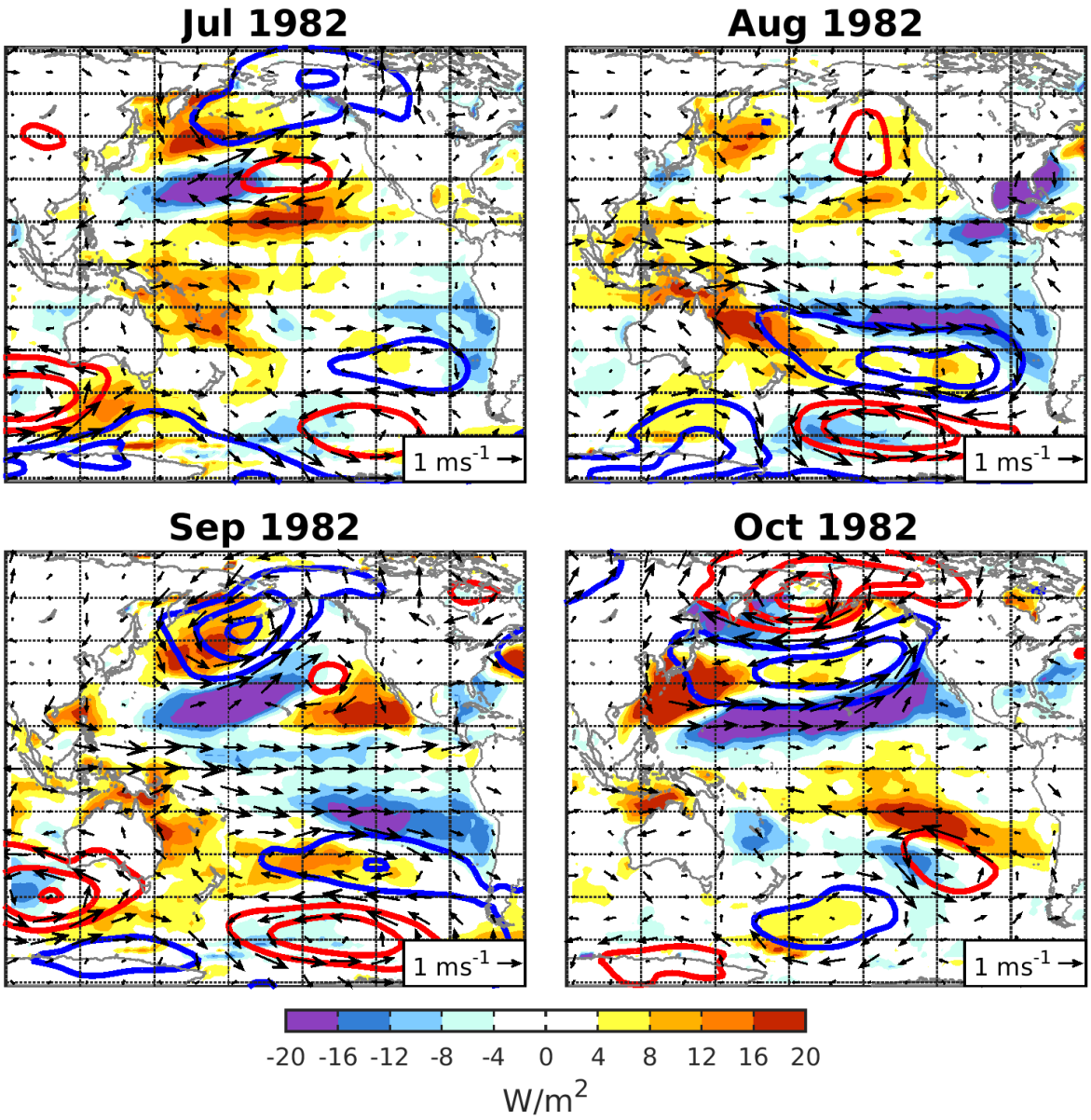

FIGURE 4.3: Monthly mean noise structures for July through October 1982. Sea level pressure (SLP) anomalies (hPa; contours), 850mb wind anomalies (m/s; vectors), and ocean-atmosphere flux (OAFLUX) anomalies (Wm^{-2}; shading) are shown. Positive (negative) SLP anomalies are indicated with red (blue) contours where the contour interval is every 1 hPa. The zero contour has been omitted. OAFLUX fluxes are defined as positive upwards.

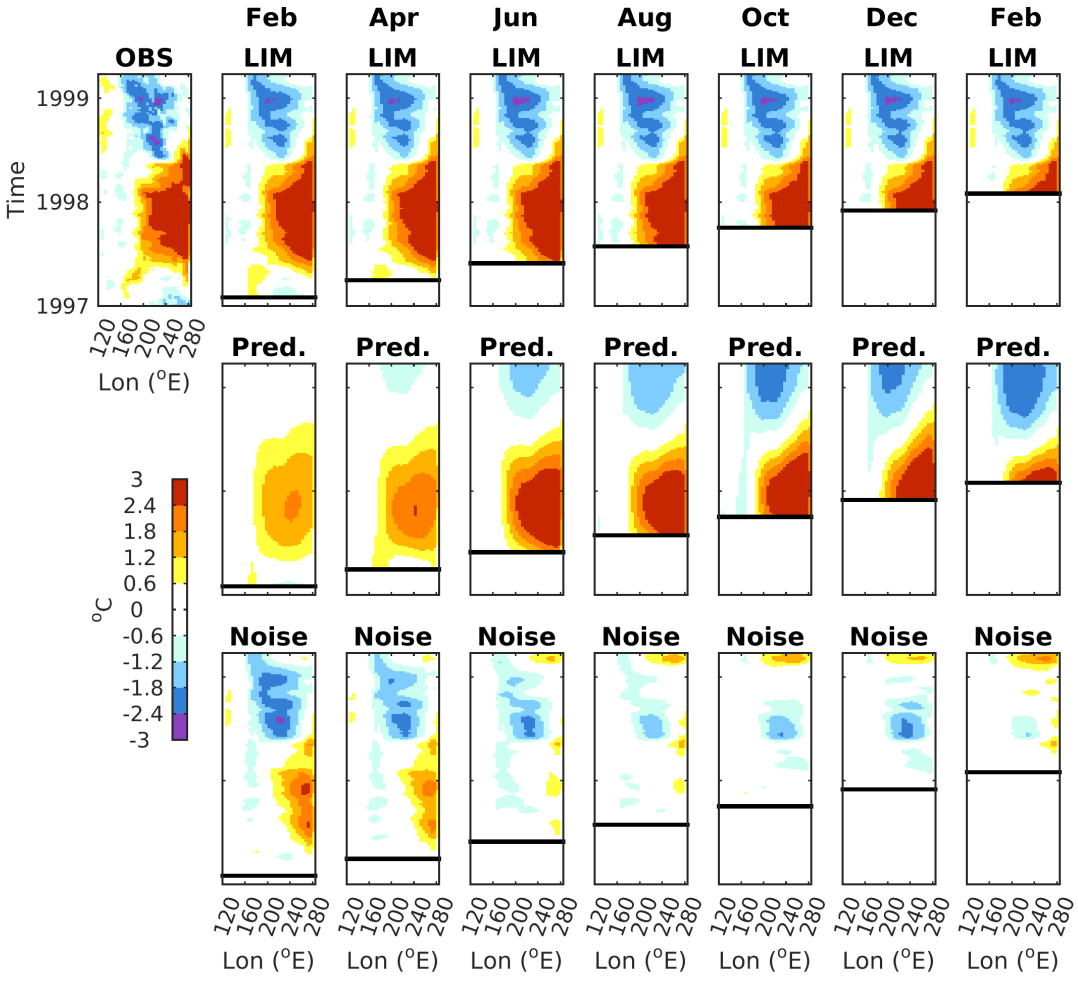

FIGURE 4.4: Same as Figure 4.1 except for the 1997/1998 EP El Niño Event.

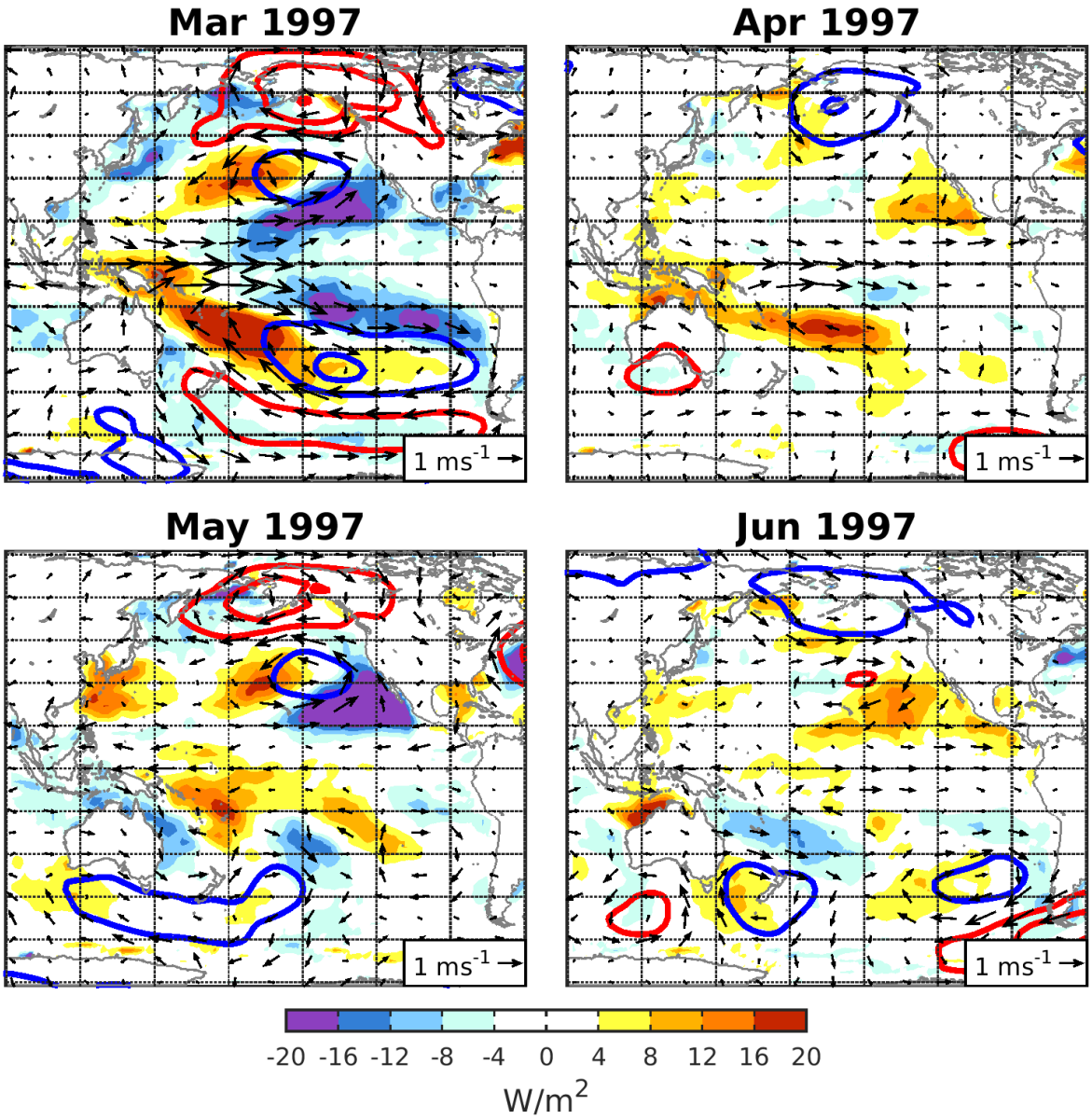

FIGURE 4.5: Same as Figure 4.3, except for March 1997 through June 1997.

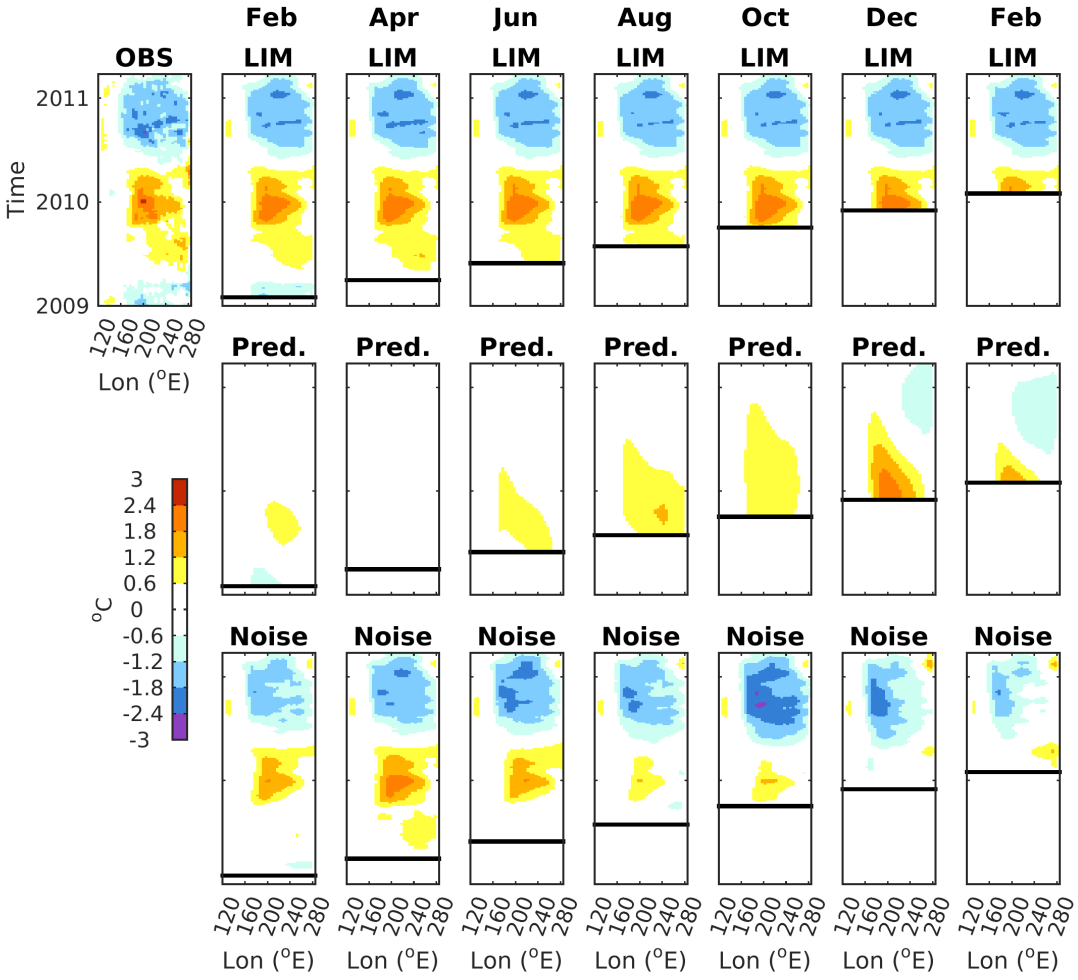

FIGURE 4.6: Same as Figure 4.1, except for the 2009/2010 CP El Niño Event.

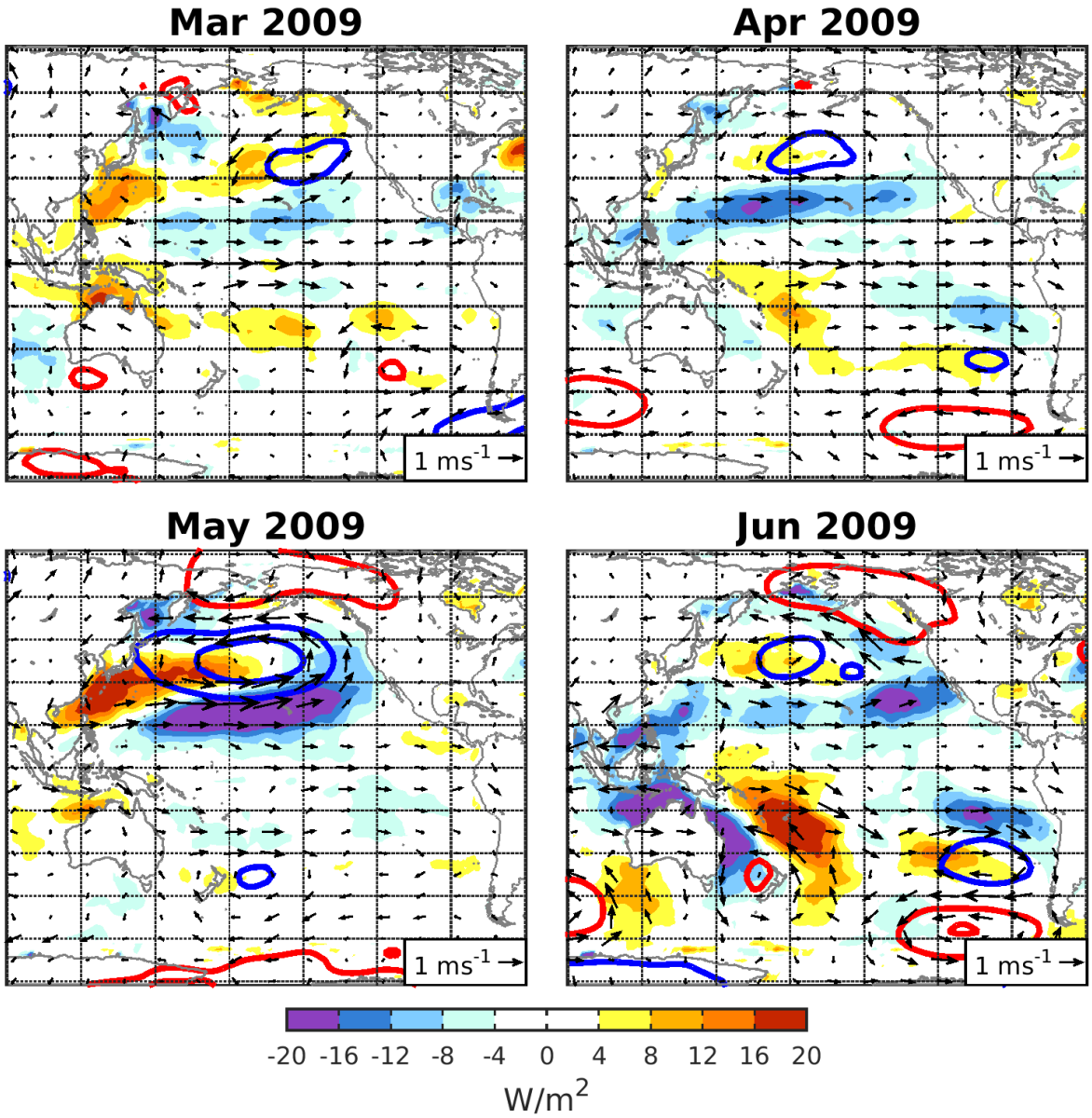

FIGURE 4.7: Same as Figure 4.3, except for March 2009 through June 2009.

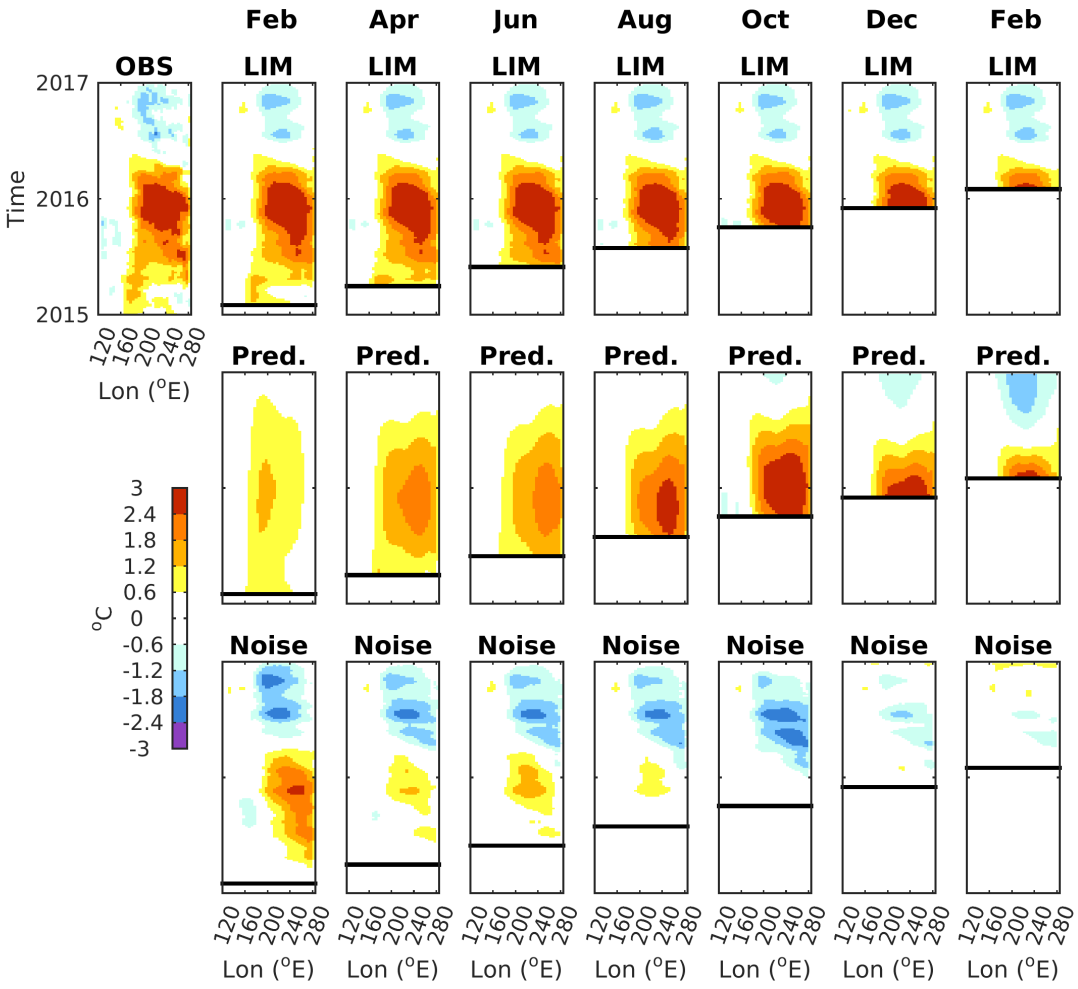

FIGURE 4.8: Same as Figure 4.1, except for the 2015 El Niño event.

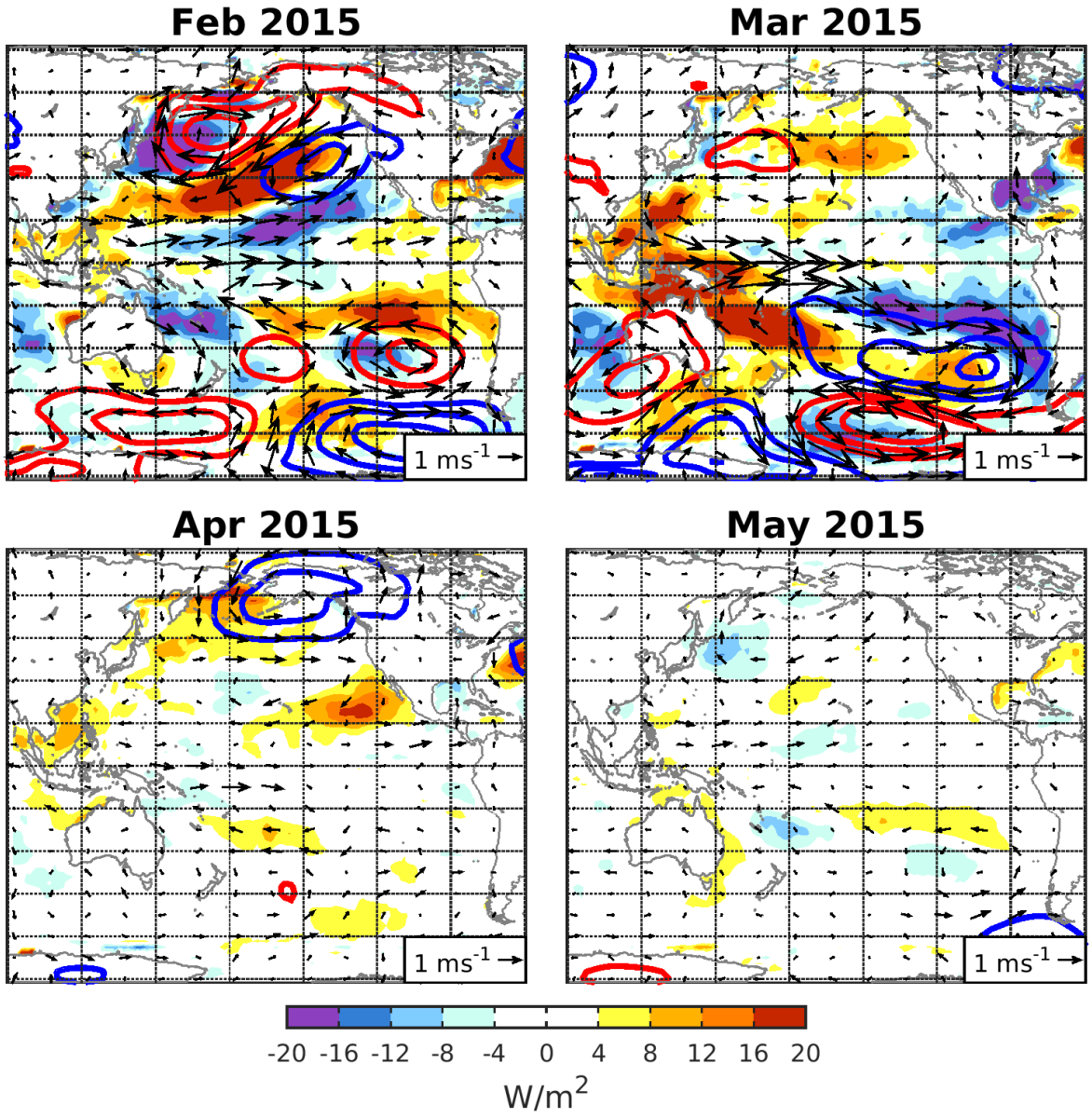

FIGURE 4.9: Same as Figure 4.3, except for February 2015 through May 2015.

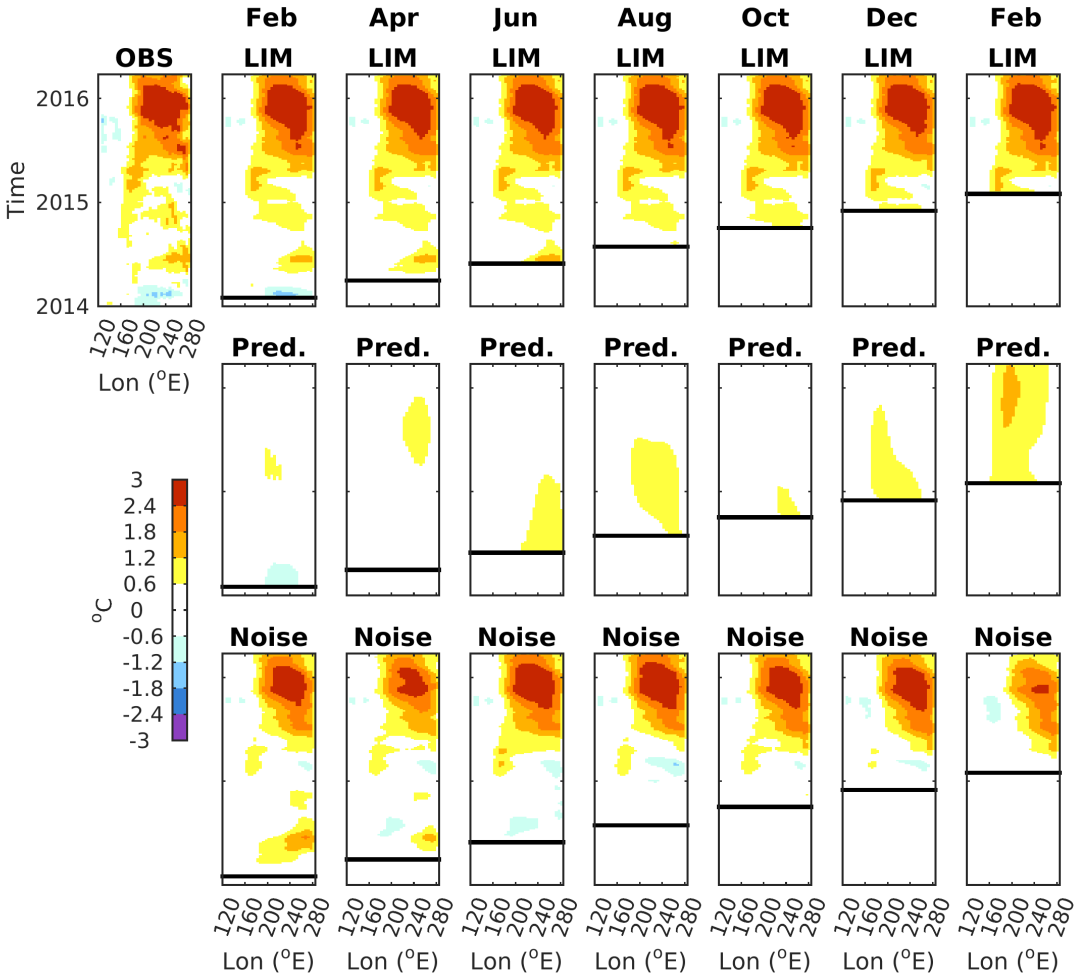

FIGURE 4.10: Same as Figure 4.1, except for the 'failed' 2014 event.

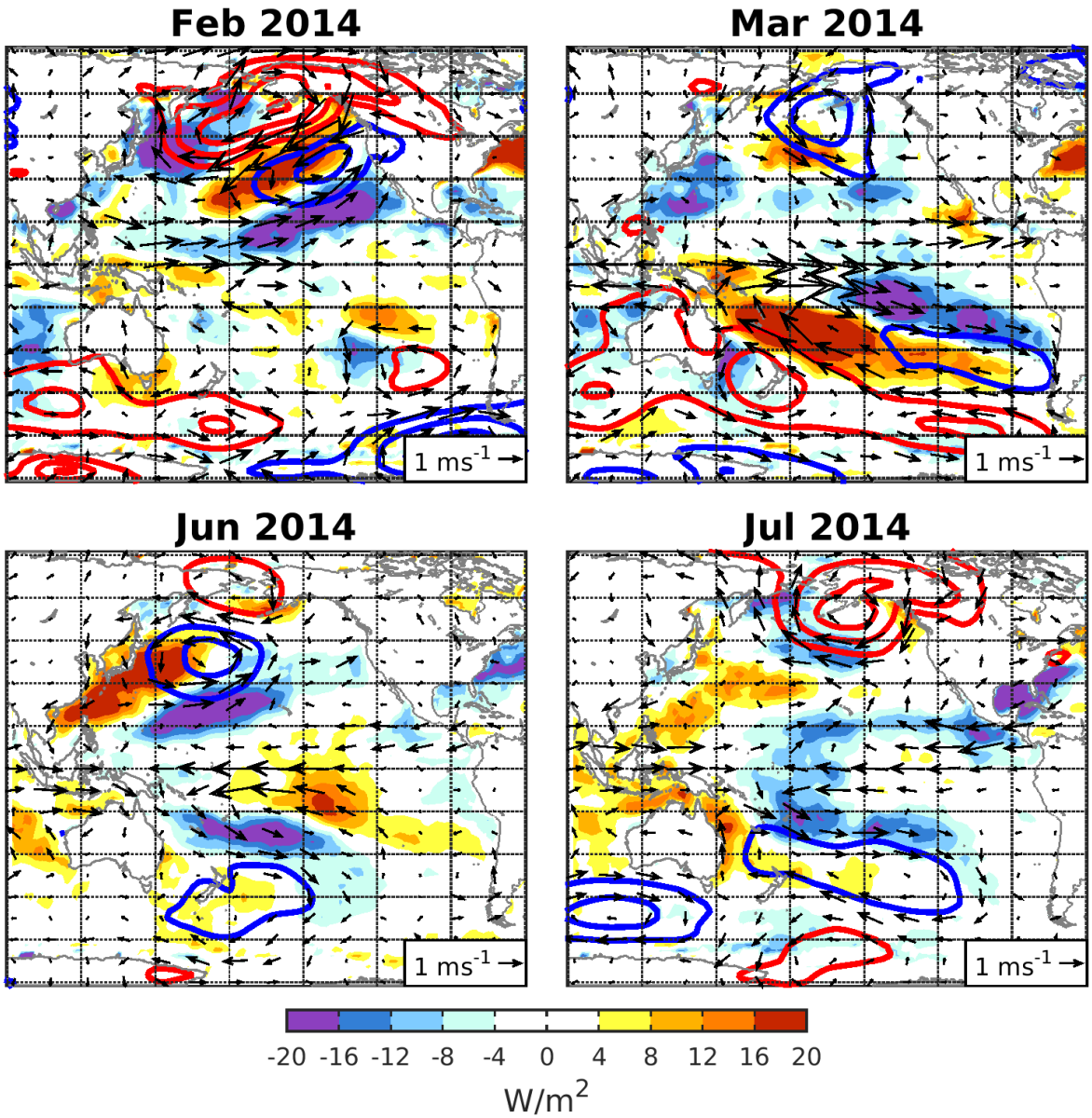

FIGURE 4.11: Same as Figure 4.3, except for February, March, June and July 2014. Only the months with large magnitude noise forcing structures are shown.

Chapter 5

Stochastic Forcing structures associated with ENSO Diversity within the Community Earth System Model

These results are preliminary, however, some of the content of this chapter will be prepared for submission as part of a peer reviewed publication.

5.1 Introduction

Many physical processes may play a role in generating ENSO diversity. This study, as described in Chapter 3, uses a forecast perspective in which the evolution of an individual ENSO event from a given time depends on (i) the specific set of initial conditions that determine how the system will evolve along its deterministic trajectory, as well as (ii) the

"external" forcing that, when convolved with the dynamics, pushes the system away from (in general) the deterministic trajectory. A third possibility exists that ENSO diversity is caused by variations in the internal dynamics responsible for ENSO evolution (e.g. Fedorov and Philander 2000, 2001; An and Wang 2000; An and Jin 2000; Wang and An 2002; Yeh et al. 2009; Capotondi and Sardeshmukh 2017). Here, however, we focus on the role of stochastic forcing in generating ENSO diversity within the CESM.

Chapter 3 describes a method for estimating the noise forcing structures that lead to ENSO diversity using observations. Chapter 4 then showed how these noise forcing structures in combination with the initial state of the tropical Pacific influence the development of ENSO events through the analysis of several historical ENSO events. This allowed us to estimate the relative roles of the deterministic dynamics versus the role of the rapidly varying stochastic forcing.

Testing these noise forcing structures in a fully coupled global climate model will identify the mechanisms though which these noise forcing structures influence ENSO growth. However, since models do not exactly simulate the observed climate system the model may not realistically respond to the observed forcing structures (see Chapter 3) as expected. Therefore, we must force the model with comparable noise structures simulated by the model. This chapter uses the same methods as described in Chapter 3 to determine the noise forcing structures within CESM that are analogous the the observed noise forcing structures. The physical mechanisms of the CESM noise forcing structures calculated in this chapter will be tested using a set of forced CESM experiments described in Chapter 6.

We apply the Linear Inverse Model (LIM) method that is thoroughly described in Chapter 3 to 35 ensembles from the CESM Large Ensemble Project (LENS) to estimate the

noise forcing structures associated with generating the CP and EP optimal initial conditions within the CESM model. This chapter is organized as follows: Section 5.2 describes the LENS data and LIM methods, Section 5.3 describes the noise forcing structures associated with CP and EP growth within the CESM and Section 5.4 discusses the conclusions of this work.

5.2 Data and Methods

We develop a LIM using data from the CESM-Large Ensemble Project (LENS; Kay et al. 2015). We use data from the LENS project since it contains the daily output necessary to calculate the stochastic noise forcing of Central and Eastern Pacific optimal initial conditions. As with the methods described in Chapter 3, we follow the methods outlined in Penland and Hartten (2014) to empirically calculate the noise forcing conducive to CP and EP growth directly from the LENS data. We then identify the physical mechanisms within the noise forcing that lead to CP or EP growth within CESM. The implications for CP and EP ENSO predictability will be discussed.

5.2.1 Data: LENS

The LIM is constructed using monthly mean sea surface temperature (SST) and sea surface height (SSH) data in the tropical Pacific [120°:285°E, -25°:25°N] between 1982 and 2015 from the first 35 ensemble members of the LENS project. SSH is used rather than thermocline depth (as done in the observational analysis, see Chapter 3) since the LENS does not contain daily 3D ocean temperature fields which is needed to calculate the thermocline depth. However, SSH is a good proxy for thermocline depth and upper ocean heat content (Rebert et al. 1985), therefore the conclusions in this study are comparable with studies that use thermocline depth. Each of the 35 ensemble members is de-trended

and averaged into 2° latitude by 5° longitude grids. Monthly anomalies are calculated by removing the ensemble-mean annual cycle and smoothed with a three month running mean.

As previously done with the observations (Chapter 3), EOF analysis is applied as a prefilter the monthly SST and SSH anomalies. The state vector x (Equation 5.1) is defined as the leading 9 SST modes and leading 5 SSH modes. The leading two SST EOFs are shown in Figure 5.1a,b and leading EOFs of SSH are shown in Figures Figure 5.1c,d. Similar to the leading modes of observed SST, the leading SST EOF in CESM (explains 60.7% of the variance) shows a canonical ENSO pattern, while SST EOF2 (explains 7.8 % of the variance) shows a patter similar to the PMM. Figure 5.1e,f show the SST patterns of Central and Eastern Pacific ENSO events, respectively, based upon the Takahashi et al. definition (Equation 3.1 and Equation 3.2). These definitions will be used to define the direction of growth in order to determine the CP and EP optimal initial conditions within the CESM. It is well documented that the magnitude of ENSO is over estimated and extends too far west in the CESM (Deser et al. 2012). This bias is clearly seen in Figure 5.1 where the leading SST EOF extends much farther to the west than the observed leading SST EOF (Figure 3.1). Similarly SST EOF2 maximizes much farther west that the observed SST EOF2 (Figure 3.1). This results in a shift of the CP and EP event within the model.

We define the state vector x with sea surface temperature (SST) and sea surface height (SSH) as follows:

$$x = [Z_{SST}, Z_{SSH}] \tag{5.1}$$

where Z_{SST} is the leading 9 SST principal components (PCs) (explains 85.6% of the variance) and Z_{SSH} are the leading 5 SSH PCs (explains 74.1% of the variance). The PC's of the state vector are normalized by the square root of the total variance of the respective field; i.e. Z_{SST} is normalized by the square root of the sum of all SST eigenvalues, and Z_{SSH} is normalized by the square root of the sum of all SSH eigenvalues.

5.2.2 Linear Inverse Model and Optimal Initial Conditions

As seen in (Equation 3.3), we approximate the evolution of the Tropical Pacific by a multivariate linear model. For a detailed explanation of the methodology, refer to Chapter 3.

We calculate the optimal initial conditions that maximize either CP or EP growth within the CESM. Again, the noise forcing that maximizes growth towards CP or EP events will be the noise that pushes the system toward these optimal initial conditions. Using the calculated linear dynamics of the CESM tropical Pacific (Equation 3.7) we determine the initial state that maximizes deterministic growth in a specified direction (Penland and Sardeshmukh 1995; Newman et al. 2011; Vimont et al. 2014), hereafter, referred to as the optimal initial condition. For a complete description of the methods to estimate the optimal initial condition refer to Chapter 3.

Figure 5.2a and Figure 5.2c show the optimal initial conditions that maximize either CP or EP growth within CESM, respectively, over a 6-month time period. We choose to maximize growth over 6 months ($\tau = 6\text{mo}$) to maintain consistency with the observational analysis in Chapter 3. The final CP and EP ENSO states are shown in Figure 5.2b and Figure 5.2d, respectively. The optimal initial and associated final conditions found in the CESM are similar to those seen in observations (Figure 3.2), although the CESM bias that produces ENSO too far west is particularly apparent in both the CP and EP final structures. The CESM optimal initial condition that maximizes CP growth shows

a SST structure representative of the PMM and a thermocline structure containing an increased zonal thermocline gradient, with deep thermocline anomalies in the western Pacific and shoaled thermocline anomalies in the eastern Pacific. Unlike the observed CP optimal pattern, the CESM optimal also contains large warm SST anomalies along the equatorial Pacific. Similar to the observed analysis, the CESM EP optimal initial condition shows a strong zonal SST gradient containing positive SST anomalies located in the far eastern Pacific and negative SST anomalies in the western and central Pacific. The CESM EP optimal also contains a deepened thermocline across much of the central equatorial Pacific, which agrees with the pattern found in observations.

5.3 Noise Forcing of CP and EP optimals within CESM

This section first describes the methods to estimate the noise forcing of CP and EP optimals within the CESM and then presents the physical mechanisms that contribute to the noise forcing.

5.3.1 CESM Stochastic Forcing

We use a centered differencing method (Equation 3.14); Penland and Hartten (2014); Thomas et al. (2017 *in review*)) to estimate the stochastic forcing of the tropical Pacific system in the CESM.

The rapidly varying state vector x (see Equation 3.14) is defined as the projection of the pentad SST and SSH data onto the leading 9 SST and 5 SSH EOF structures, that were identified from monthly data in Section 5.2. As before, the modes (9 SST and 5 SSH) of the high frequency state vector x are normalized by the square root of the total variance

of their respective variable monthly resolved data. SST pentad means are calculated from daily SST from 1982-2015 for all 35 ensembles of the LENS data. Similarly, SSH pentad means are calculated from daily SSH from 1982-2015 for the 35 ensembles of the LENS data. Both SST and SSH pentad data are detrended and averaged onto the same 2° latitude by 5° longitude grid as the monthly data. Pentad anomalies are calculated by removing the ensemble mean annual cycle and smoothed with a five-pentad running mean.

5.3.2 CESM Noise Structures associated with CP and EP Optimals

We estimate the noise forcing that pushes the system towards CP or EP optimal initial conditions by projecting the noise forcing (see Section 5.3.1) onto the spatial patterns of the CP and EP optimals. The result is a time series of the noise forcing that pushes the system towards generating CP or EP optimal initial conditions. Figure 5.3 shows the seasonal variance of the noise forcing time series associated with the CP and EP optimals plotted in red and black, respectively. The variance was smoothed with successive 5- and 7-pentad centered running means. The CESM CP noise variance is highest during boreal winter (DJF), which agrees with observations well. The CESM EP noise variance, on the other hand, contains a much different seasonal cycle than the CP variance. The CESM EP variance is highest during boreal summer (JJA), unlike the seasonal variance of the observed EP noise variance.

To determine physical mechanisms within the stochastic forcing, we regress pentad averaged LENS data onto the stochastic forcing time series associated with either the CP or EP optimals. Pentad means are calculated from daily LENS data between 1982 and 2015 for the detrended 35 ensembles. The ensemble mean annual cycle is then removed. The

anomalous LENS pentad data is then regressed onto the normalized stochastic forcing time series for the CP and EP optimals, respectively.

Figure 5.4 shows seasonal regression maps of SLP (contours), OLR (shading) and 850mb wind (vectors) regressed onto the CP and EP noise forcing in the left and right columns, respectively. Figure 5.5 shows seasonal regression maps of OAFLUX (shading; defined as the sum of sensible heat flux and latent heat flux) and surface wind stress (vectors) regressed onto the CP and EP noise forcing in the left and right columns, respectively. These structures push the system towards the development of CP or EP optimal initial conditions. Again, the regression maps are interpreted as variability in a particular field that covaries with the noise forcing of a given optimal initial condition.

The CP SLP contours (Figure 5.4, left column) show seasonal dependence, where the winter hemisphere dominates. In agreement with the observational results (Figure 3.4), the northern hemisphere SLP pattern during DJF resembles the NPO, with a dipole structure located in the north Pacific. This pattern corresponds to the DJF peak in the seasonal CP noise variance shown in Figure 5.3. The left column of Figure 5.5 shows the corresponding OAFLUX and zonal wind stress patterns associated with the noise forcing of the CP optimal. The OALFUX pattern is consistent with the SLP anomalies and associated winds, showing large heat flux anomalies into the ocean in the subtropical Pacific. The CP forcing patterns in the CESM agree well with the timing and structure of the noise forcing patterns found in the observations. In particular, the boreal winter pattern resembling the NPO appears to be of primary interest in the generation of CP ENSO events within the CESM.

The EP SLP and 850mb wind regressions show a strong dipole pattern during JJA in the southern hemisphere that resembles the SPO (Figure 5.4). This pattern corresponds

to the timing of the maximum in the seasonal EP noise variance in the CESM, however the model produces this peak in the noise forcing variance as well as the corresponding spatial patterns during boreal summer (JJA) rather than spring (MAM), as seen in the observations (Figures 3.4 and 3.5). Furthermore, the 850mb wind patterns show strong zonal wind anomalies in the central equatorial Pacific during JJA. Figure 5.5 shows the corresponding OAFLUX patterns with the JJA SPO pattern. The pattern shown large heat flux anomalies into the ocean off the western coast of South America that extend northwestward toward the central tropical Pacific.

5.4 ENSO response to CP and EP forcing

The LIM forecasting framework is used to estimate the linear ENSO response to the noise forcing (refer to Equation 3.5). Since the CP and EP noise forcing is simply the projection of the noise onto the CP or EP optimal, the LIM is forced with either the CP or EP optimal initial conditions (i.e. ζ in Equation 3.5 is defined as the CP or EP optimal). Considering the noise forcing structures that excite the CP or EP optimal initial conditions appear to be seasonally dependent we apply the forcing for a duration of three months. The forcing is then removed and the LIM continues to integrate forward in time. The initial state of the system ($\mathbf{x}(\mathbf{t_0})$ in Equation 3.5) is set to zero to estimate the response of a linear dynamical system to only the CP or EP forcing.

Figure 5.6 shows the monthly evolution of the LIM in response to three months of constant forcing by the CP optimal. The CP optimal is applied as external forcing during months 1-3. The CP optimal is then removed while the system is continues to respond. The SST (shading) shows an increase in SST in the central Pacific by month 3. The magnitude of the SST anomalies amplifies over the next 9 months, where the maximum amplitude SST anomalies occur in the central Pacific. The SSH (contours) shows increased thermocline

depth along the equator in the central Pacific during month 4. This SSH signal extends eastward over the next several months reaching the coast of South America by month 7. Also notable, is the lack of SSH response in the southern Hemisphere. The SST pattern in response to the CP forcing suggests that CP events evolve as a standing wave in the central Pacific.

Figure 5.7 shows the monthly evolution of the LIM in response to three months of constant EP forcing. The EP optimal is applied as external forcing during months 1-3. The EP optimal is then removed while the system continues to respond. The SSH (contours) rapidly responds to the EP forcing showing a KW like signal along the equator in the central Pacific by month 2. This signal quickly propagates eastward reaching the eastern edge of the basin by month 3 where the SST (shading) shows positive anomalies. A forced Rossby wave signal appears in the western Pacific during months 3-4, propagating westward. Interestingly, this RW signal is not apparent in the CP experiment (Figure 5.6). The demise of the ENSO event begins during months 9 and 10. The SST anomalies begin to decay in month 11 and the ENSO event is noticeably decaying by month 12. The SST and SSH of the linear system in response to the EP forcing suggests EP events may be highly dependent upon thermocline dynamics.

Finally, we wish to look at the entire evolution of the linear system in response to CP and EP forcing. Figure 5.8 shows Hovmoller diagrams of the equatorial SST (averaged between 2S:2N) in the tropical Pacific (from 120°E to 285°E) of the LIM in response to the CP and EP forcing. Time (in months) increases on the y axis, and longitude (°E) is on the x axis. Similar to the conclusions made above, the Hovmoller diagram of tropical Pacific SST shows a standing wave-like response to CP forcing. The CP ENSO event amplifies and decays in the central Pacific. The EP forcing, on the other hand, generate

positive SST anomalies that amplify and decay in the far eastern Pacific followed by a La Niña response located in the central Pacific.

5.5 Conclusions

This chapter identifies patterns within stochastic noise forcing that generate the development of CP and EP characteristics within NCAR's CESM. We use the forecast perspective as discussed in Chapter 3, by applying linear inverse modeling to separate the deterministic evolution of the tropical Pacific system from the noise-forced non-deterministic evolution. In this forecast framework, the noise can either enhance deterministic growth by generating initial conditions that largely project on to optimal initial states, or it can lead to non-deterministic growth (forecast error) by pushing the system away from the deterministic trajectory. While chapter three showed the noise structures conducive to CP and EP growth in observations, the noise forcing that excites the optimal structures has not been previously identified in a fully coupled GCM.

Most of the noise forcing characteristics in the CESM are similar to those seen in observations (Chapter 3), however the model has a few biases. These biases must be taken into consideration when interpreting these results. CESM simulates ENSO variance much too far west in the Pacific. This bias is seen in the spatial structure of the leading SST EOFs, and therefore affects the spatial patterns of CP and EP events according to the definitions used. Additionally, this bias manifests itself in the spatial structures of the CP and EP optimal initial conditions.

The CP noise forcing agrees with the observed analysis well and shows a peak in variance during boreal winter (DJF). The corresponding CP noise forcing spatial structure also matches observations well, the SLP, wind, and heat flux patterns resembles that of the

NPO. The seasonal variance of the EP noise forcing within the CESM is shifted for the EP events. The peak in variance within CESM occurs during JJA instead of MAM as in observations, though it is not clear whether this result is significant. This generates the EP noise patterns of interest which occur during MAM in observations to occur in JJA within the model. Although there is a time lag in the EP noise forcing within the model, the spatial patterns match those of observations well. The JJA EP noise forcing pattern matches the spatial structure of the SPO well. The CESM bias in the timing of the EP noise forcing as compared to observations may contribute to the model's inability to simulate EP ENSO characteristics well. The importance of the noise structures associated with either CP or EP optimal initial conditions will be addressed in the forced CESM experiments described in Chapter 6.

As previously mentioned, these methods contain some limitations. LIM uses a linear estimation of the non-linear dynamics. It is possible the linear approximation fails to capture some non-linear dynamics properly. However, LIM has been shown to represent the Tropical Pacific system well (Penland and Sardeshmukh 1995; Penland 1996; Penland and Matrosova 1998; Newman 2007; Alexander 2008; Newman 2011). Furthermore, we were limited to using the data from the CESM Large Ensemble Project due to the daily data needed in order to calculate the noise forcing using the methods outlined above. The configuration used for the LENS project may not necessarily be the same as other fully coupled models, therefore noise forcing patterns related to CP and EP optimal initial conditions should be tested in other models.

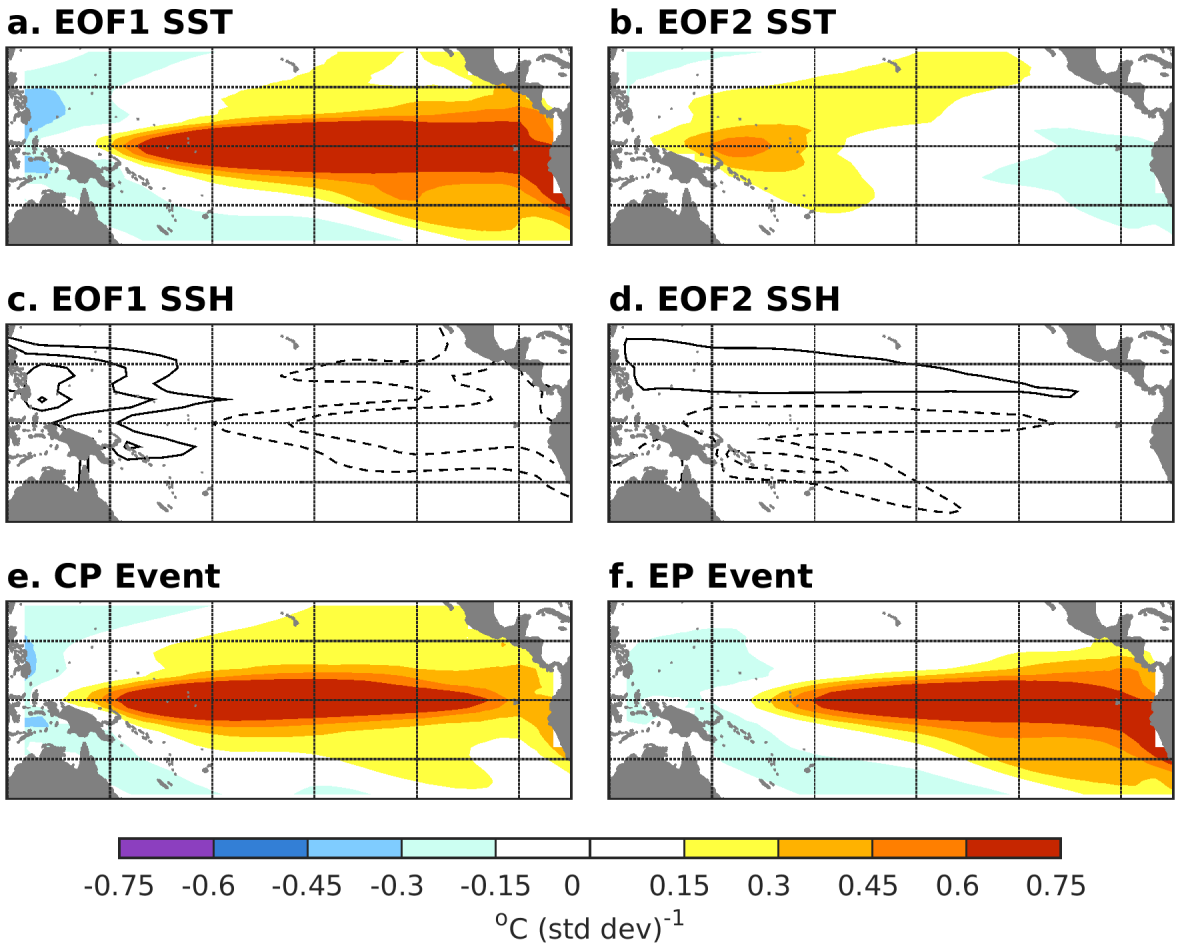

FIGURE 5.1: Leading two EOF patterns of SST(a, b), thermocline depth (c, d), and the defined spatial structure of CP and EP events (e and f; respectively).

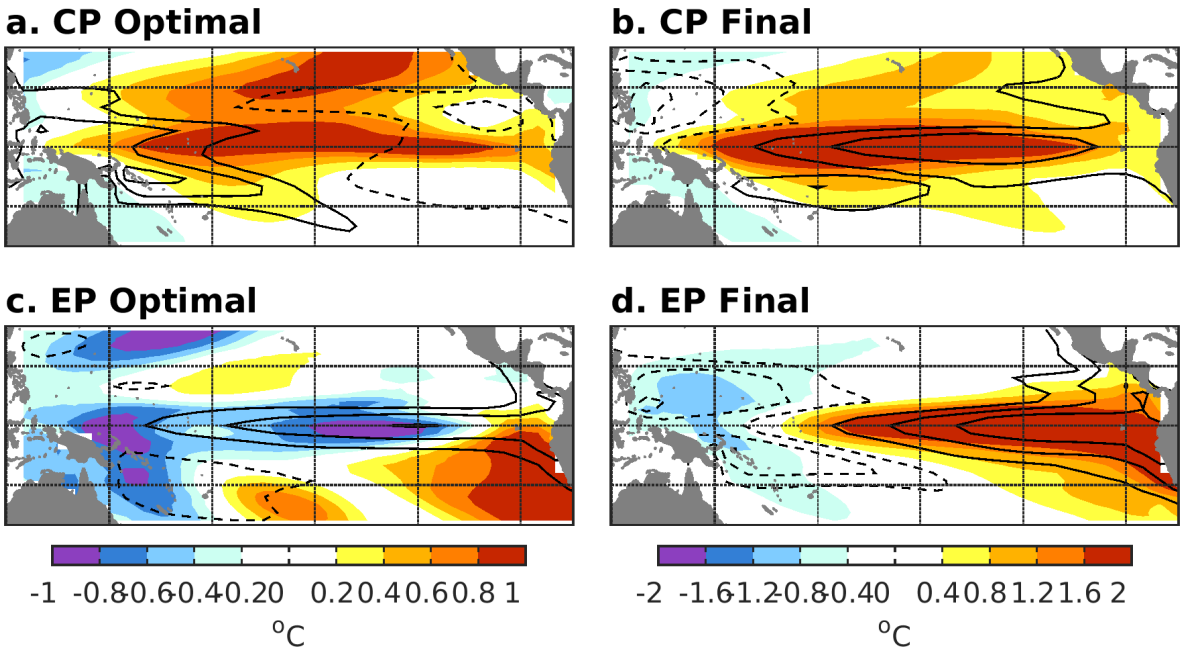

FIGURE 5.2: SST (°C; shading) and thermocline depth (m; black contours) for $\tau = 6$ mo CP and EP optimal initial conditions (a,c) and final states (b,d) within CESM. SST contour interval is .4°C for the optimals and .8°C for the final conditions. Thermocline depth contour interval is 4m for the optimals and 8m for the final conditions. Positive (negative) thermocline depth anomalies correspond to solid (dashed) contours. The zero contour has been omitted.

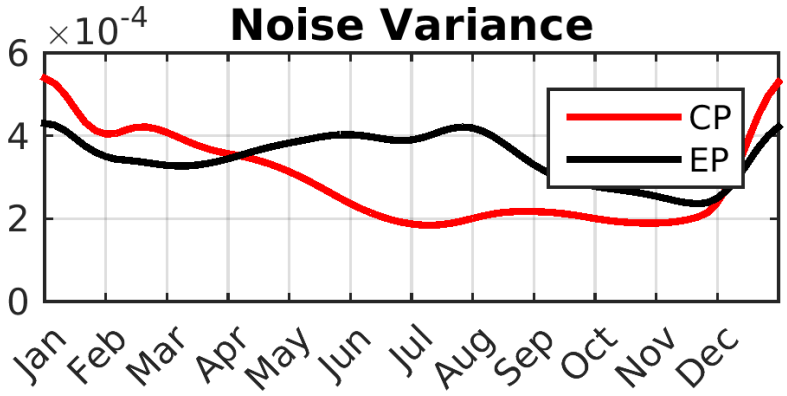

FIGURE 5.3: The seasonal variance of the noise forcing associated with the CP (red) and EP (black) optimals. The variance is smoothed with successive 5- and 7-pentad running means.

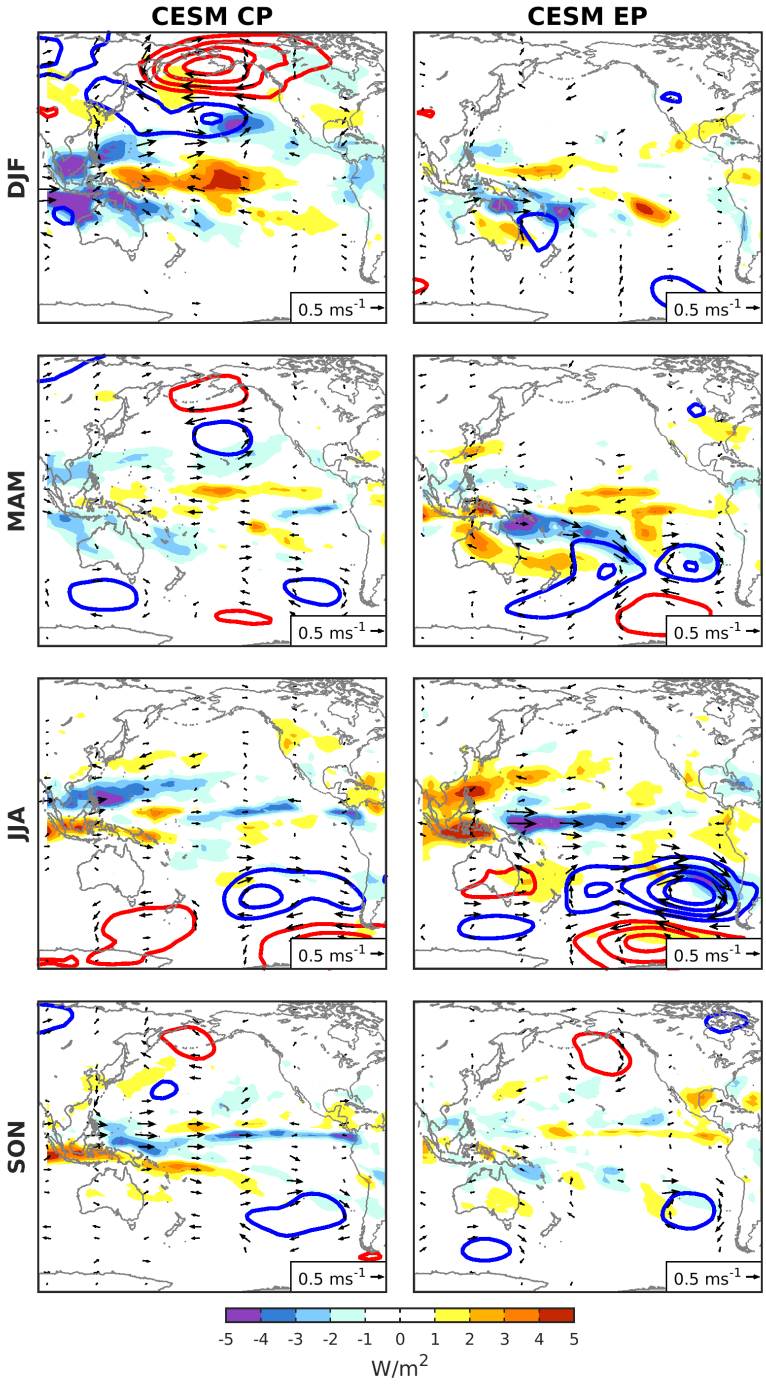

FIGURE 5.4: Atmospheric noise structures associated with Central Pacific and Eastern Pacific optimal initial conditions (left and right columns, respectively). Shown are the seasonal regression coefficients between sea level pressure (SLP; hPa; contours), 850mb wind (m/s; vectors), and outgoing longwave radiation flux (OLR; W/m2; shading) and the noise forcing time series of CP or EP optimal initial conditions. The first row shows the regression coefficients of boreal winter (DJF). The second through fourth rows show the regression coefficients for boreal spring (MAM), summer (JJA) and fall (SON) months, respectively. Positive (negative) SLP indicated with red (blue) contours where the contour interval is every 0.5 hPa. The zero contour has been omitted. OLR is defined as positive upwards. Wind vectors are only shown where the geometric sum of the correlation coefficients is equal to or greater than .1.

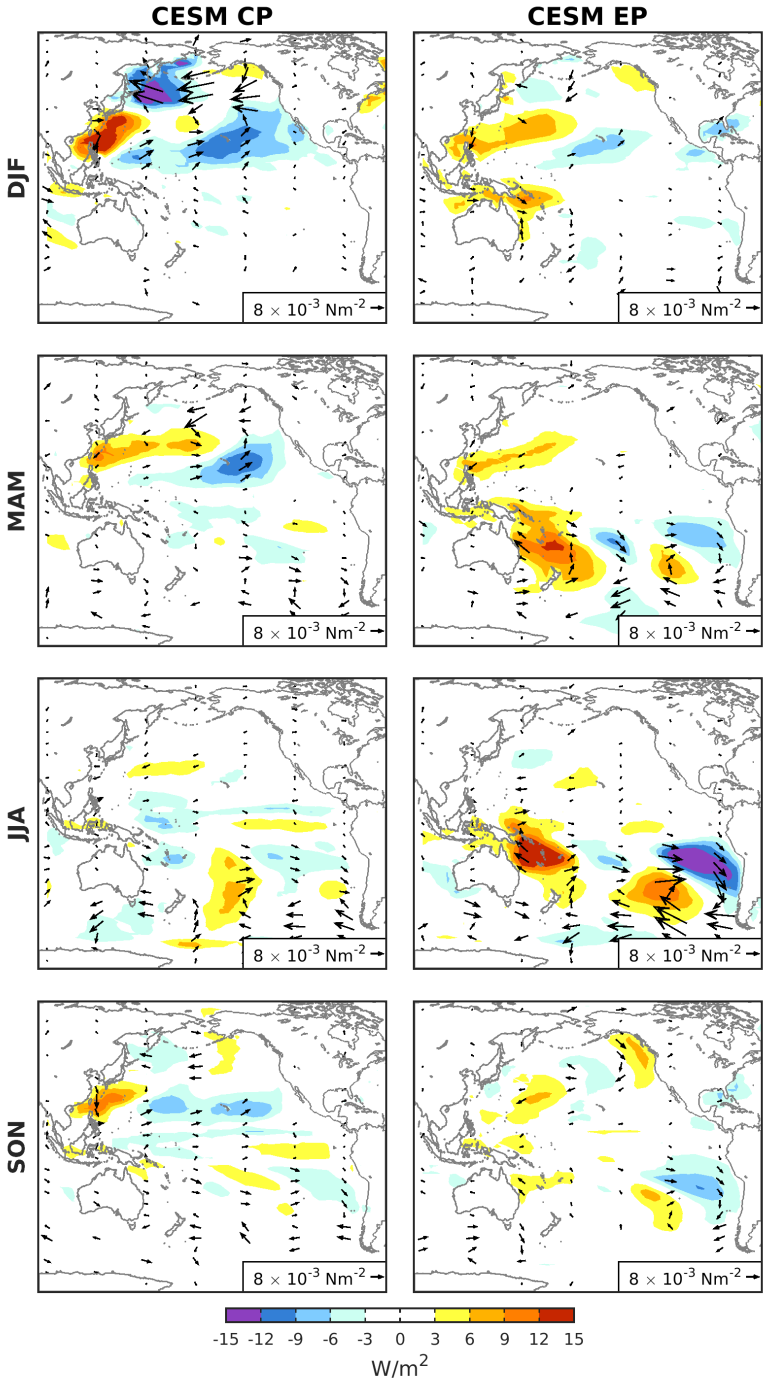

FIGURE 5.5: Noise Forced oceanic structures associated with Central Pacific and Eastern Pacific optimal initial conditions (left and right columns, respectively). Shown are the seasonal regression coefficients between surface wind stress (N/m2; vectors) and ocean-atmosphere flux (OAFLUX; W/m2; shading) and the noise forcing time series of CP or EP optimal initial conditions. The first row shows the regression coefficients of boreal winter (DJF). The second through fourth rows show the regression coefficients for boreal spring (MAM), summer (JJA) and fall (SON) months, respectively. OAFLUX is defined as positive upwards. Wind stress vectors only shown where the geometric sum of the correlation coefficients is equal to or greater than .1.

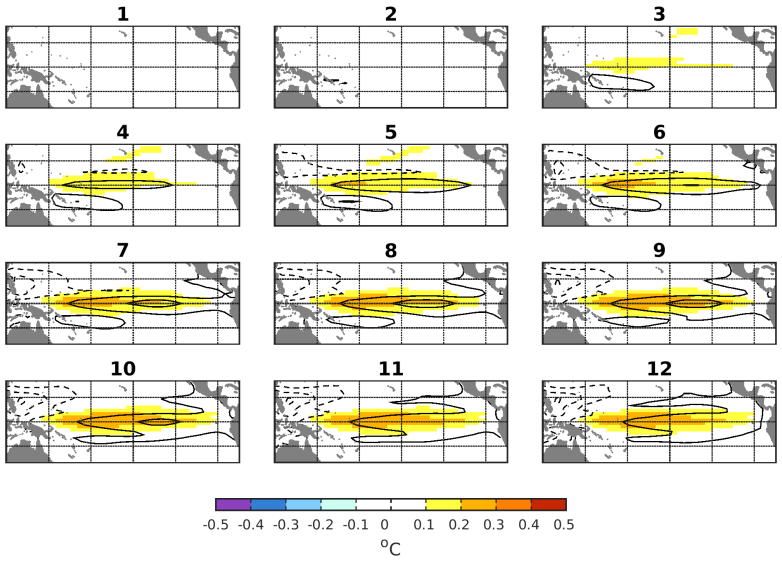

FIGURE 5.6: LIM response to three months of CP forcing by the CP optimal. Monthly evolution of SST (shading) and SSH (contours) anomalies are plotted. SSH contour interval is every .5 cm where positive (negative) anomalies are indicated by solid (dashed) contours. The zero contour has been omitted.

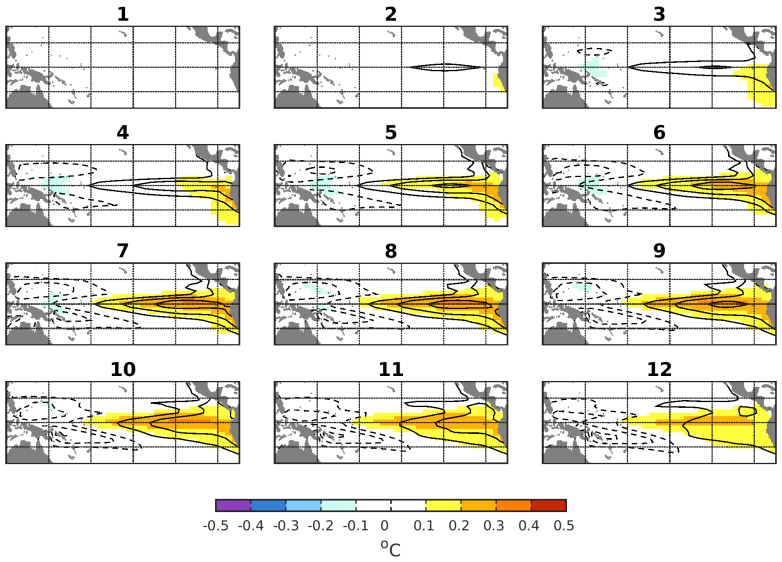

FIGURE 5.7: LIM response to three months of EP forcing by the EP optimal. Monthly evolution of SST (shading) and SSH (contours) anomalies are plotted. SSH contour interval is every .5 cm where positive (negative) anomalies are indicated by solid (dashed) contours. The zero contour has been omitted.

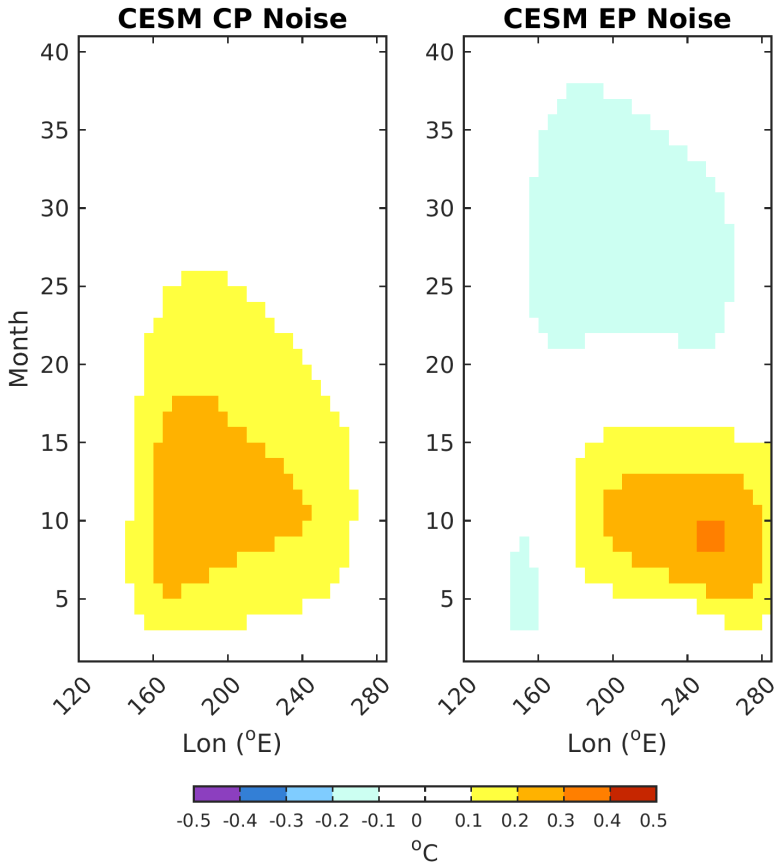

FIGURE 5.8: Hovmoller diagram of equatorial SST (averaged between 2°S:2°N) in response to three months of CP and EP forcing(left and right, respectively). The forcing applied to the LIM is simply the CP or EP optimal initial condition (see text for details). Time (in months) increases on the y axis, longitude (°E) on the x axis.

Chapter 6

The Role of Stochastic Forcing in Generating ENSO Diversity within the Community Earth System Model

These results are preliminary, however, some of the content of this chapter will be prepared for submission as part of a peer reviewed publication.

6.1 Introduction

A variety of physical processes have been proposed to explain ENSO diversity. The varying roles of these physical processes allows any given ENSO event to have a continuous range of CP and EP characteristics (Karnauskas 2013; Capotondi et al. 2015). In particular, stochastic forcing (loosely defined here as forcing that is external to the essential deterministic dynamics that produce ENSO variability) has been shown to generate ENSO diversity (Newman et al. 2011).

CP-related initial conditions are associated with the Pacific Meridional Mode (PMM; Chiang and Vimont 2004). The PMM has been shown to be connected to a mode of wintertime SLP variability in the north Pacific referred to as the North Pacific Oscillation (NPO). The NPO and PMM interact with ENSO variability through the "seasonal footprinting mechanism" (Vimont et al. 2001, 2003a,b, 2009; Zhang et al. 2009; Yu and Kim 2011; Park et al. 2013).

Southern hemisphere atmospheric variability has also been implicated in generating initial heat content anomalies that can influence EP-type ENSO events (You and Furtado 2017). They describe a dipole SLP pattern in the southeast Pacific as the "South Pacific Oscillation" (SPO) and identify it as an EP ENSO precursor. Additionally, similar SLP patterns are also found in Penland and Matrosova (2008). Furthermore, a pattern referred to as the South Pacific Meridional Mode (SPMM; Zhang et al. 2014) may be linked to southern hemisphere wintertime SLP variability and EP ENSO variability (Min et al. 2017). Furthermore, studies also show that ENSO events with strong EP characteristics, such as the 1997/1998 El Niño event, are influenced by westerly wind busts (WWB) that occur in the western tropical Pacific (e.g. Boulanger and Menkes 1999; McPhaden 1999; Harrison and Chiodi 2009; Federov et al. 2015; Chen et al. 2015).

Previously a linear inverse modeling framework calculated the noise forcing patterns associated with generating CP and EP optimal initial conditions with NCAR's CESM (Chapter 5). This chapter selects three individual noise forcing patterns of interest and isolates them from the full spatial domain of the noise forcing seen in Chapter 5. The noise forcing patterns selected support the findings of previous studies and include i) the NPO-like DJF north hemisphere heat flux pattern associated with generating the CP optimal, ii) the SPO-like JJA heat flux pattern in the south east Pacific associated with

the EP optimal, and iii) the JJA wind stress noise forcing in the west equatorial Pacific associated with the EP optimal.

These three patterns of interest are used to force three sets of ensemble experiments using the fully coupled CESM in order to estimate the the relative roles and mechanisms of specific components of the noise forcing patterns that contribute to the development of central or Eastern Pacific ENSO events. This chapter is organized as follows: Section 6.2 provides description of the model configuration (LENS), the experimental setup, and the noise forcing used. Section Section 6.3 describes the results of the noise forced experiments and Section 6.4 discusses the conclusions of this work.

6.2 Model description and Experimental setup

This section provides descriptions of the CESM model, the experimental set-up, and the noise forcing used.

6.2.1 CESM description

CESM experiments using the LENS configuration are performed to determine the role of the noise forcing patterns to the development of CP and EP ENSO characteristics within the model. The experiments use the LENS setup since the noise structures are estimated from LENS data. The LENS setup uses the fully coupled CESM1 with approximately a 1° horizontal grid (f09_g16 resolution). It is a fully coupled model containing the Community Atmosphere Model version 5.2 (CAM5, 30 vertical layers), parallel ocean program, version 2 (POP2, 60 vertical layers), community land model (CLM), and the Los Alamos Sea Ice Model (CICE). The model uses historical radiative forcing until 2005 and RCP8.5 radiative forcing thereafter. For a full description of the LENS model setup refer to Kay et al. (2015).

6.2.2 Experimental Setup

We run a set of 60 control simulations as well as three sets of forced experiments each containing (approximately) 60 ensemble members. January 1, 1990 restart files for the first 30 LENS ensemble members are used to initialize the first half of the control simulations. The second half of the control simulations are initialized using the January 1, 2000 restart files from the first 30 ensemble members of the LENS. The initialization year of the control simulations will be hereafter referred to as year (0). All 60 control simulations are run for a total of 27 months (i.e. Jan(0) through March(2)). Figure 6.1 shows a schematic of the experimental set up.

The first experiment (Experiment 1; Figure 6.1) forces the model with the CP heat flux noise forcing pattern seen in the North Pacific during DJF. The 60 ensemble members for Experiment 1 are initialized during Nov of year (0) from each of the 60 control simulations. We apply a two standard deviation noise forcing anomaly to force the model from Dec(0) through Feb(1). The forcing is then removed and the model allowed to continue to evolve through the end of March(2) (each ensemble is run for a total of 17 months). The following (Section 6.2.3) describes the applied forcing patterns for all three experiments in detail.

The second experiment (Experiment 2; Figure 6.1) forces the model with the EP heat flux noise forcing pattern seen in the south East Pacific during JJA. The 60 ensemble members for Experiment 2 are initialized May(1) from each of the 60 control simulations. We apply a two standard deviation noise forcing anomaly to force the model from Jun(1) through Aug(1). The forcing is then removed and the model allowed to continue to evolve through the end of March (2) (each ensemble is run for a total of 11 months).

The heat flux forcing (Experiments 1 and 2) is applied to the CESM by modifying the

calculation of the net coupled heat flux forcing from fluxes passed from the coupler to ocean component (POP) as follows:

$$\mathbf{F_{Net}} = \mathbf{F_{Force}} + (\mathbf{F_{Evap}})\mathbf{l_v} + \mathbf{F_{SH}} + \mathbf{F_{LWnet}} + \mathbf{F_{Melt}} + (\mathbf{F_{Snow}} + \mathbf{F_{Ice}})\mathbf{l_f}, \tag{6.1}$$

where $\mathbf{F_{Net}}$ is the net surface heat flux forcing applied to the ocean surface, $\mathbf{F_{Force}}$ is the anomalous external heat flux forcing , $\mathbf{F_{Evap}}$ is evaporation flux, l_v is the latent heat of vaporization, $\mathbf{F_{SH}}$ is the sensible heat flux, $\mathbf{F_{LWnet}}$ is the net longwave flux, $\mathbf{F_{Melt}}$ is the melt heat flux, $\mathbf{F_{Snow}}$ is the snow flux, $\mathbf{F_{Ice}}$ is the ice runoff flux, and l_f is the latent heat of fusion.

The third experiment (Experiment 3; Figure 6.1) forces the model with the EP wind stress noise forcing pattern seen during JJA in the west equatorial Pacific. All 60 ensemble members for Experiment 3 are initialized May(1) from each of the 60 control simulations. We apply a two standard deviation wind stress noise forcing anomaly to force the model from Jun(1) through Aug(1). The forcing is then removed and the model continues to evolve through the end of March (2) (each ensemble is run for a total of 11 months).

The wind stress forcing is applied to the CESM by adding the anomalous wind stress forcing to the wind stress passed from the CESM coupler to ocean component (POP) as follows:

$$\tau_{\mathbf{net}} = \tau_{\mathbf{atm}} + \tau_{\mathbf{force}}, \tag{6.2}$$

where $\tau_{\mathbf{net}}$ is the wind stress applied to the ocean surface, $\tau_{\mathbf{atm}}$ is the wind stress passed from the atmosphere component and $\tau_{\mathbf{force}}$ is the anomalous wind stress forcing.

6.2.3 Noise Forcing

Chapter 5 describes the methods in which we use apply Linear Inverse Modeling to the data from the LENS project to calculate the patterns of noise forcing conducive to CP and EP growth within the model. The forcing patterns are calculated by regressing three dimensional variables onto the time series of the CP or EP noise forcing. This results in regression maps that can be interpreted as variability in a particular field that covaries with the noise forcing of either the CP or EP optimal initial condition. For a more complete description of the calculation methods of the noise forcing patterns refer to Chapter 5. Three specific regions of interest within the full spatial domain noise forcing patterns are isolated to generate the three forcing patterns used in the experiments. These patterns of interest are chosen based upon supporting evidence within the scientific literature highlighting the potential importance of these three structures to ENSO diversity (e.g. Vimont et al. 2003a,b; 2014; Kim et al. 2012; Capotondi et al. 2015; Zhang et al. 2014; You and Furtado 2017; Federov et al. 2015; Hu et al. 2014).

Experiment 1 isolates the CP OAFLUX noise forcing pattern during DJF in the north Pacific. Experiment 2 isolates the EP OAFLUX noise pattern in the south east Pacific during JJA, and Experiment 3 isolates the EP wind stress noise pattern in the west equatorial Pacific during JJA. Furthermore, the magnitude of the forcing patterns used in the experiments (Figure 6.2) is equal to two standard deviation anomalies. For example, the CP OAFLUX forcing used in Experiment 1 (Figure 6.2a) is twice the magnitude of the CP OAFLUX noise forcing pattern shown in Figure 5.5.

Figure 6.2a shows noise forcing applied to the ocean component of CESM for experiment 1. The pattern shown is OAFLUX noise forcing associated with the CP optimal in the North Pacific during DJF. The forcing pattern shown represents a two standard deviation anomaly, based upon the normalized noise forcing time series (i.e flux forcing applied to the model is twice the magnitude of the patterns in Figure 5.5). This pattern of forcing is applied to the ocean component of CESM continuously during December through February. The heat flux forcing (defining positive as downwards into the ocean) used is characterized by a positive flux into the ocean extending southwestward from the west coast of North America into the west tropical Pacific.

Figure 6.2b shows the noise forcing applied to the ocean component of CESM for Experiment 2. The pattern shown is the two standard deviation OAFLUX noise forcing associated with the EP optimal in the southeast Pacific during JJA. This pattern of forcing is applied as a constant forcing to the ocean component of CESM during June through August. The heat flux anomalies are defined as positive is downwards into the ocean. Positive heat flux anomalies are located in the subtropics off the west coast of South America and extend northwestward toward the central tropical Pacific. Negative heat flux anomalies are located to the southwest of the positive anomalies. The heat flux forcing pattern resembles that associated with the SPO.

Figure 6.2c shows the noise forcing used in Experiment 3. The noise forcing is the two standard deviation wind stress noise forcing associated with the EP optimal in the west equatorial Pacific during JJA. The forcing is applied continuously to the ocean component of CESM during June through August. The structure contains positive zonal winds anomalies in the equatorial west Pacific, which loosely resembles a weak WWB.

By isolating individual patterns of interest from the full noise forcing regression maps

we are able to test the relative importance of specific components of the noise forcing to CP and EP growth. However, this study only selects three patterns of interest to study and it is important to note other components within the noise forcing may be critical to generating ENSO diversity. Further research is necessary to determine these structures and their relative importance to creating ENSO diversity.

6.3 Results

This section describes the response of the fully coupled CESM to each of the three noise set of noise forcing structures.

6.3.1 Experiment 1: DJF CP OAFLUX forcing

Figure 6.3 shows the monthly evolution of the ensemble mean anomalous SST (shading) and SSH (contours) response to the boreal winter CP OAFLUX forcing in the north Pacific. The NPO-like heat flux forcing quickly generates an SST response resembling the PMM. This pattern first appears in Jan(1) and propagates south-westward into the tropical Pacific and amplifies in magnitude over the next couple of months (Feb(2)-Mar(2)). It persists in the subtropical Pacific through boreal summer (Jun(2)-Aug(2)), long after the forcing has been removed. This PMM pattern decays throughout boreal Fall between Sept(1) and Dec(1).

Furthermore, the ensemble mean SSH response to the NPO heat flux forcing highlights the importance of equatorial wave dynamics in how the PMM generates ENSO. An eastward propagating downwelling Kelvin wave signal, indicated by positive SSH anomalies, appears on the equator in the central Pacific beginning in Feb(1), after the PMM signal reaches the central tropical Pacific. This signal propagates eastward, reaching the South American coast in Mar(1) depressing the thermocline in the east Pacific during boreal

spring. These thermocline anomalies are coincident with warming SST in the east as indicated by the positive SST anomalies that amplify throughout the year. The development of the ENSO event peaks in magnitude near the end of the calendar year (Nov(1)-Dec(1)), after which the SST anomalies begin to decay. The decay of the positive SST anomalies is coincident with an upwelling Kelvin wave signal, which begins to increase the thermocline depth, or reduce the positive SSH anomalies, in the eastern Pacific starting in Jan(2).

The anomalous wind stress response to the boreal winter heat flux forcing (Figure 6.4) shows a coupled wind stress response in the western tropical Pacific to positive SST anomalies in the equatorial Pacific. Positive zonal wind stress anomalies occur in response to the positive SST anomalies associated with the PMM and positive SST anomalies along the equator.

6.3.2 Experiment 2: JJA EP OAFLUX forcing

Figure 6.5 shows the monthly evolution of the ensemble mean anomalous SST (shading) and SSH (contours) response to the JJA OAFLUX forcing in the south-east Pacific. The local SST quickly responds to the SPO-like heat flux forcing and generates positive SST anomalies off the west cost of South America that amplify in magnitude between Jun(1) and Sep(1). These positive SST anomalies, which loosely resemble the positive phase of the SPMM, extend north westward off the coast of South America toward the central Pacific. Beginning in Aug(1), these positive SST anomalies propagate northward towards the equator. Once reaching the eastern Equatorial Pacific, these positive SST anomalies begin to spatially spread out, extending westward. The anomalous SSH response to the JJA SPO-like heat flux forcing show positive SSH anomalies, which corresponds to a deepening of the thermocline depth, that are co-located with positive SST anomalies in the southeast Pacific.

Figure 6.6 shows the monthly evolution of the ensemble mean anomalous zonal wind stress (TAUX; shading) response to the JJA heat flux forcing in the south-east Pacific. The wind stress shown represents the atmospheric response to the SST anomalies generated by the heat flux forcing. the ensemble mean wind stress shows positive wind stress anomalies located in the subtropical south east Pacific, near the western edge of the warm SST anomalies.

6.3.3 Experiment 3: JJA EP Wind Stress forcing

Figure 6.7 shows the monthly evolution of the ensemble mean anomalous SST (shading) and SSH (contours) response to the JJA wind stress forcing in the west equatorial Pacific. The ocean responds by generating positive SST anomalies as well as positive SSH anomalies, which correspond to an increase in the thermocline depth, along the equator in the Central Pacific beginning in Jul(1). The SST anomalies in the central Pacific grow in magnitude until Oct(1) and increase in horizontal extent through the end of the year (Sep(1)-Dec(1)). The SST anomalies begin to decay after Dec(1). The initial positive SST anomalies are consistent with reduced evaporative fluxes due to a relaxation of the trade winds from the wind stress forcing. However, the persistence of the SST response may be due to the coupled atmospheric response to the warming SST, or the positive wind stress anomalies seen between Sep(1)-Dec(1) (Figure 6.8).

The evolution of the SSH structure contains components that are consistent with ocean adjustment and the delayed oscillator theory. The positive SSH anomalies along the equator between Jul(1) through Sep(1) suggests the positive zonal wind stress anomalies excite a eastward propagating downwelling Kelvin wave. This signal reaches the coast of South America in Aug(1). However, the wind stress forcing also appears to generate a Rossby wave response as indicated by large negative off-equatorial SSH anomalies in the

western Pacific. This structure appears to shut any ENSO growth off as the Rossby wave reflects off the western boundary and propagates towards the eastern Pacific as upwelling Kelvin wave signal. This is evident by the positive SSH anomalies in the central Pacific decreasing at the equator beginning in Oct(1) continuing through Jan(2).

6.4 Conclusions

Several physical process are critical in generating ENSO diversity. This study uses a set of three ensemble experiments to identify the mechanisms through which specific noise forcing structures lead to the development of ENSO diversity. One noise forcing structure related to the CP optimal, and thus capable of maximizing CP growth is chosen. This CP noise forcing structure represents the the heat flux pattern associated with the NPO during boreal winter. Two structures associated with the EP optimal, and thus EP growth, are also chosen. The first is the heat flux forcing associated with the SPO in the southeast Pacific, the second forcing pattern chosen is a wind stress pattern located in the west equatorial Pacific. Both EP foricng patterns occur during austral winter.

The ensemble mean ENSO response to the boreal wintertime NPO-like CP heat flux forcing (Experiment 1) supports many previous studies which indicate the NPO, PMM and the seasonal footprinting mechanism as an important pathway through which ENSO variability can be generated (e.g. Vimont et al. 2003; Vimont et al. 2009; Pegion 2013; Thomas and Vimont 2016; Chang et al. 2007; Alexander et al. 2010; Yu and Kim 2011; Kim et al. 2012; Park et al. 2013; Kao and Yu 2009). The SST response contains a PMM structure in the subtropics and positive SST anomalies along the equator in boreal summer (May(1) through August(1)). These patterns contain many spatial characteristics of the 6mo CP optimal initial conditions. This suggests the NPO is an important component of the stochastic noise forcing that leads to the generation of the

CP optimal and the subsequent growth of CP events. Interestingly, the ensemble mean SST and SSH response to the NPO heat flux forcing contains many CP characteristics although it does not exactly resemble an idealized CP event (refer to the CP optimal and final in Figure 5.2). For instance, the ensemble mean SST pattern in December(1), during the peak of the ENSO response, contains much larger magnitude SST anomalies in the far eastern Pacific than an ideal CP event contains.

The ensemble-mean response of the CESM to the austral winter SPO-like EP heat flux forcing (Experiment 2) suggests the SPO forcing generates a local response that resembles the SPMM. Interestingly, the lack of an ENSO response indicates the SPO and SPMM are insufficient mechanisms to initiate an ENSO event. Furthermore, the SPO forcing does not generate a pattern that resembles the EP optimal initial conditions, even though the pattern projects strongly onto the noise forcing of the EP optimal. However, the SPO and SPMM may have the potential to increase the magnitude of an existing El Niño event due to the positive SST anomalies generated in the eastern equatorial Pacific between September and May. Futhermore, the JJA EP heat flux forcing does not generate a pattern that strongly resembles the EP optimal or an EP ENSO event. Although, the heat flux forcing does create warming in the far eastern Pacific similar to the SST structure seen in the EP optimal, the thermocline anomalies found in the EP optimal are not generated (refer to Figure 5.2). This suggests the SPO, SPMM and the resulting warming in the far eastern Pacific is not sufficient to trigger an EP event.

The ensemble-mean response of the CESM to the austral winter EP wind stress forcing (Experiment 3) suggests zonal wind stress anomalies in the equatorial pacific are capable of generating a local SST response and the wave dynamics associated with ENSO variability. Although many studies suggest the importance of WWB to the generation of ENSO events, these results suggest the uncoupled, stochastic wind stress forcing associated with

the EP optimal may insufficient by itself to generate the full structure of the EP optimal and the development of an ENSO event. Although the wind stress forcing does not generate a SST pattern representative of the EP optimal, the SSH response suggests the thermocline structure generated does contain characteristics of the EP optimal, however the wind stress forcing also initiates theromcline anomalies that ultimately negates any ENSO growth .

The results of experiments 2 and 3 suggest that some combination of the positive zonal wind stress anomalies along the equator and the occurrence of the SPO may be necessary to generate both the thermocline and SST components of the EP optimal and in order to initiate ENSO development. Additional experiments should be performed to test this theory as well as other interesting components contained within the CP and EP noise forcing.

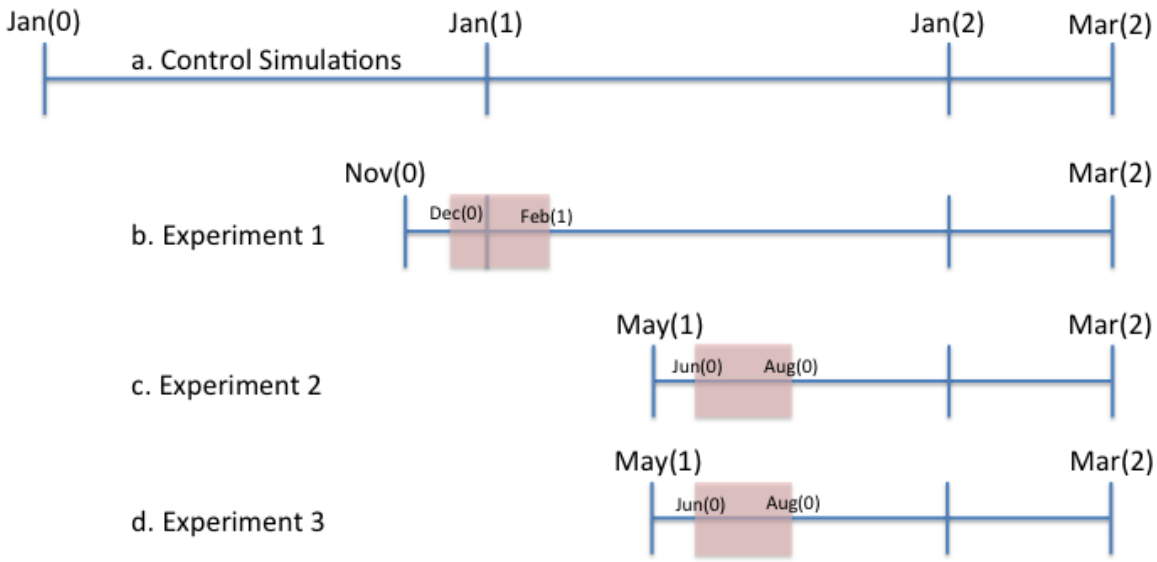

FIGURE 6.1: Diagram of the experimental setup. The timing of the forcing for each of the three forced experiments indicated by the red boxes. The control simulations (a) are run from the start of Jan(0) through the end of Mar(2). Experiment 1 (b) is initialized at the start of Nov(0) and run through the end of Mar(2) and the forcing is applied for three months between Dec(0) and Feb(1). Experiments 2 and 3 (c and d, respectively) are initialized May(1) and run through the end of Mar(2) and the forcing is applied for three months between Jun(1) and Aug(1). See text and Figure 6.2 for a description of the forcing applied to each experiment.

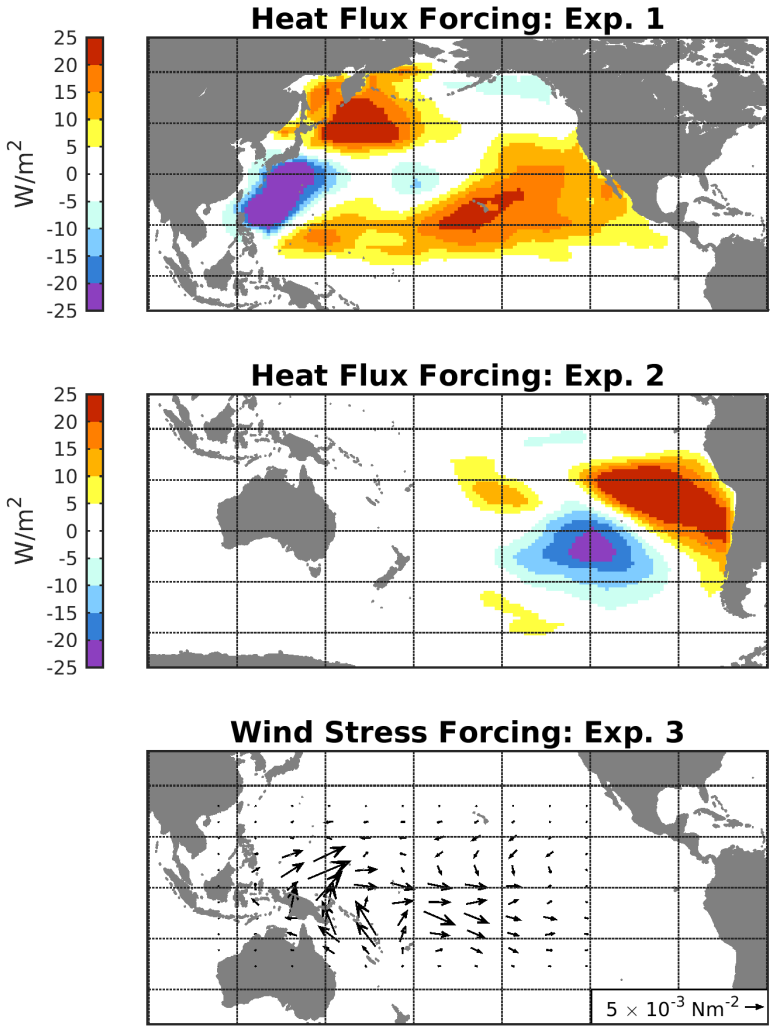

FIGURE 6.2: Forcing structures for the three forcing experiments. Boreal winter (DJF) CP OAFLUX (Wm^{-2}) forcing in north Pacific as applied to Experiment 1 (top). Middle figure shows austral winter (JJA) EP OAFLUX (Wm^{-2}) forcing in south east Pacific used in Experiment 2. Bottom figure shows austral winter (JJA) EP wind stress (Nm^{-2}) forcing pattern in the west equatorial pacific used to force Experiment 3. OAFLUX is defined as positive downwards.

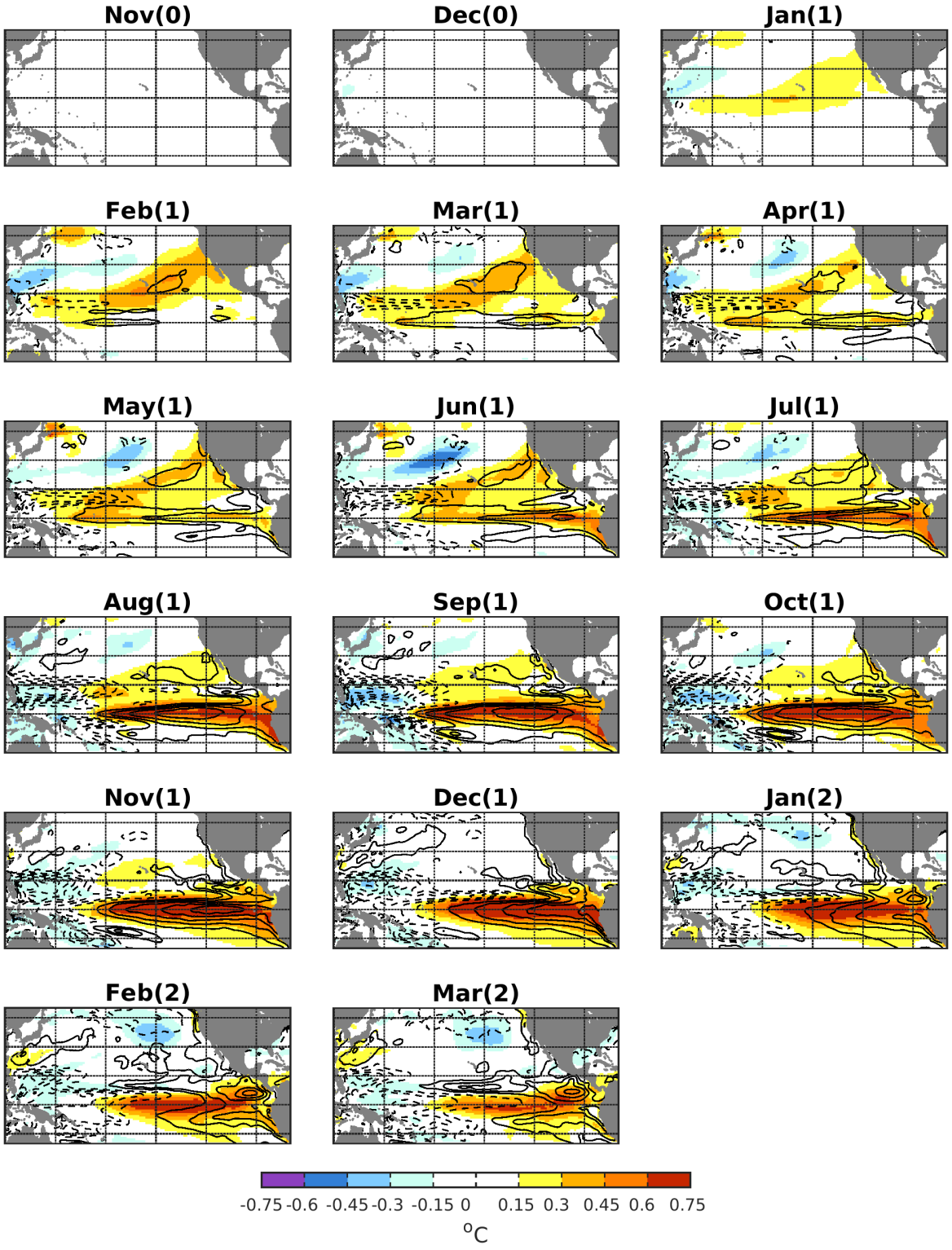

FIGURE 6.3: Monthly evolution (November(0) through March(2)) of the ensemble mean SST (°C; shading) and SSH (cm; contours) response to the DJF CP heat flux forcing. The SSH contour interval is every 1cm where the zero contour has been omitted.

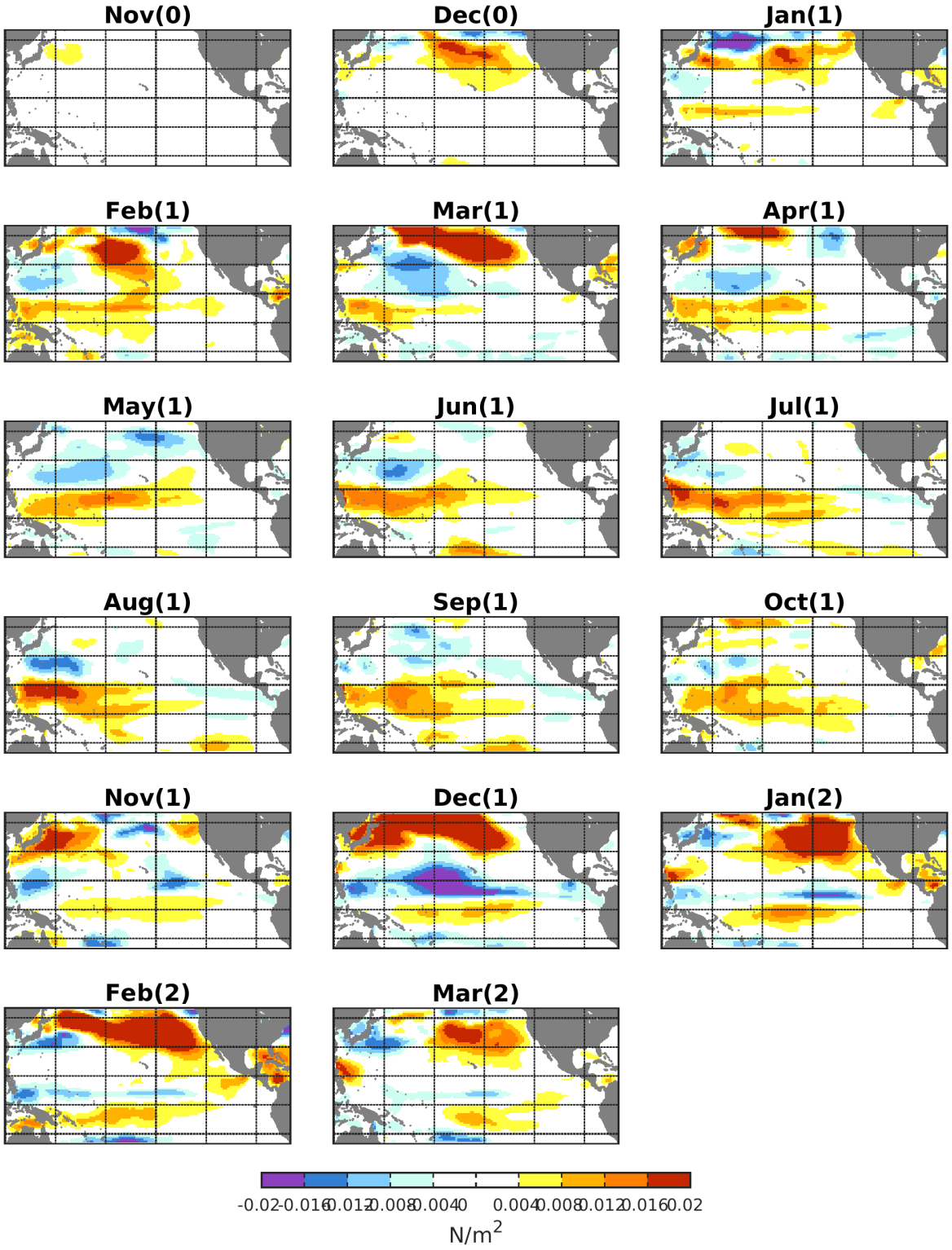

FIGURE 6.4: Monthly evolution (November(0) through March(2)) of the ensemble mean zonal wind stress (TAUX; Nm^{-2}; shading) response to the DJF CP heat flux forcing.

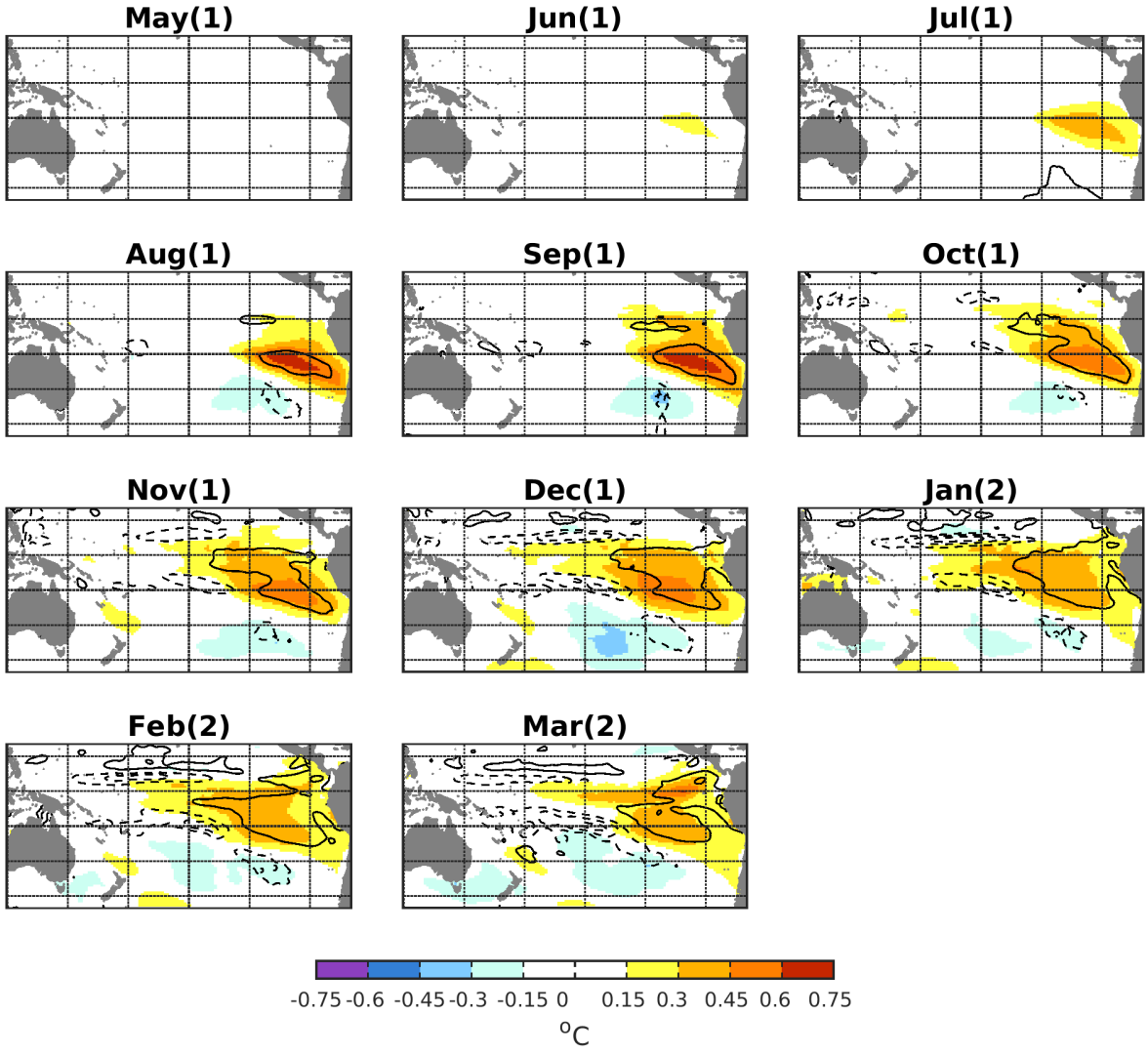

FIGURE 6.5: Monthly evolution (May(1) through March(2)) of the ensemble mean SST (°C; shading) and SSH (cm; contours) response to the JJA EP heat flux forcing. The SSH contour interval is every 1cm where the zero contour has been omitted.

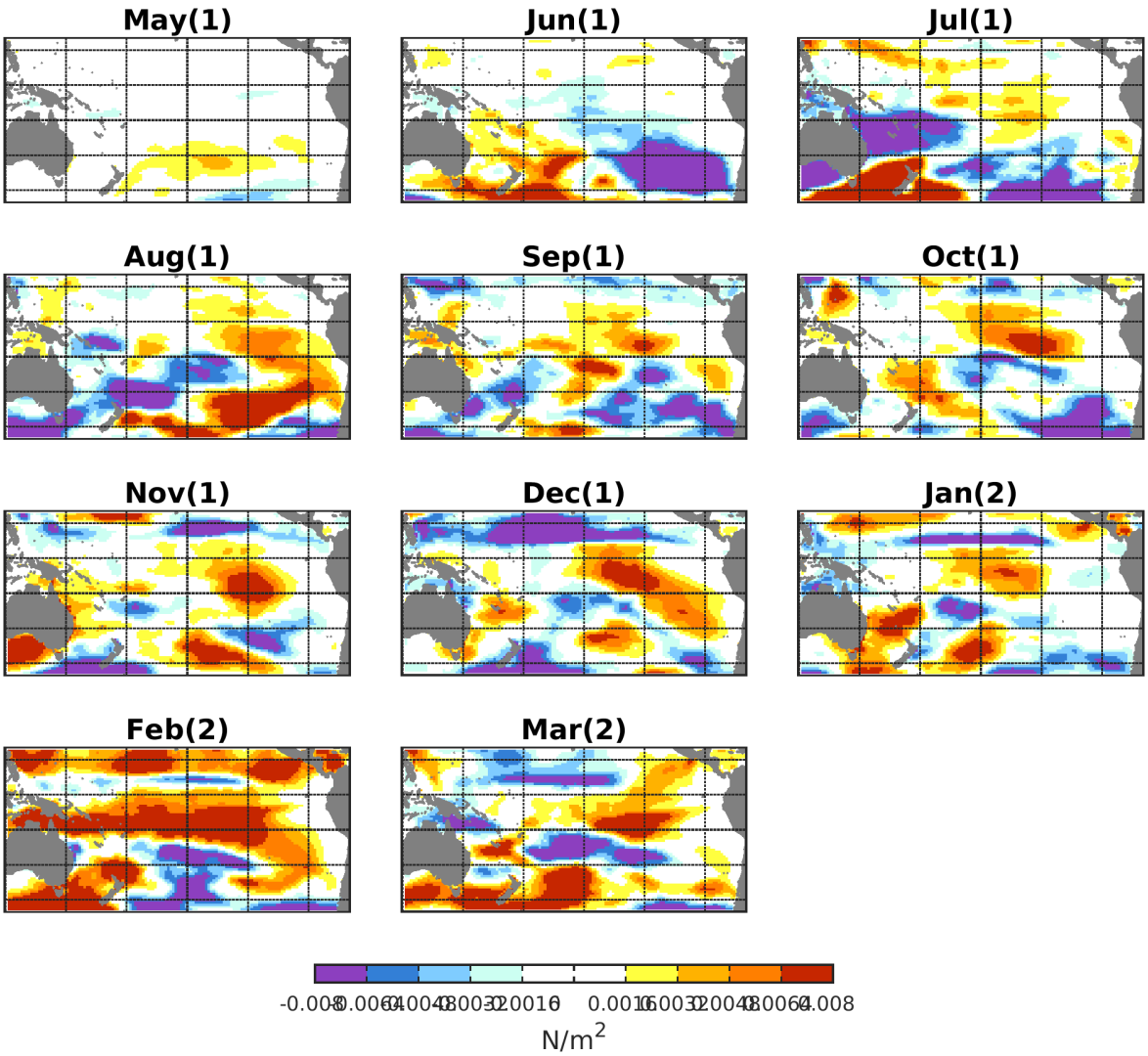

FIGURE 6.6: Monthly evolution (May(1) through March(2)) of the ensemble mean zonal wind stress (TAUX; Nm^{-2}; shading) response to the JJA EP OAFLUX forcing.

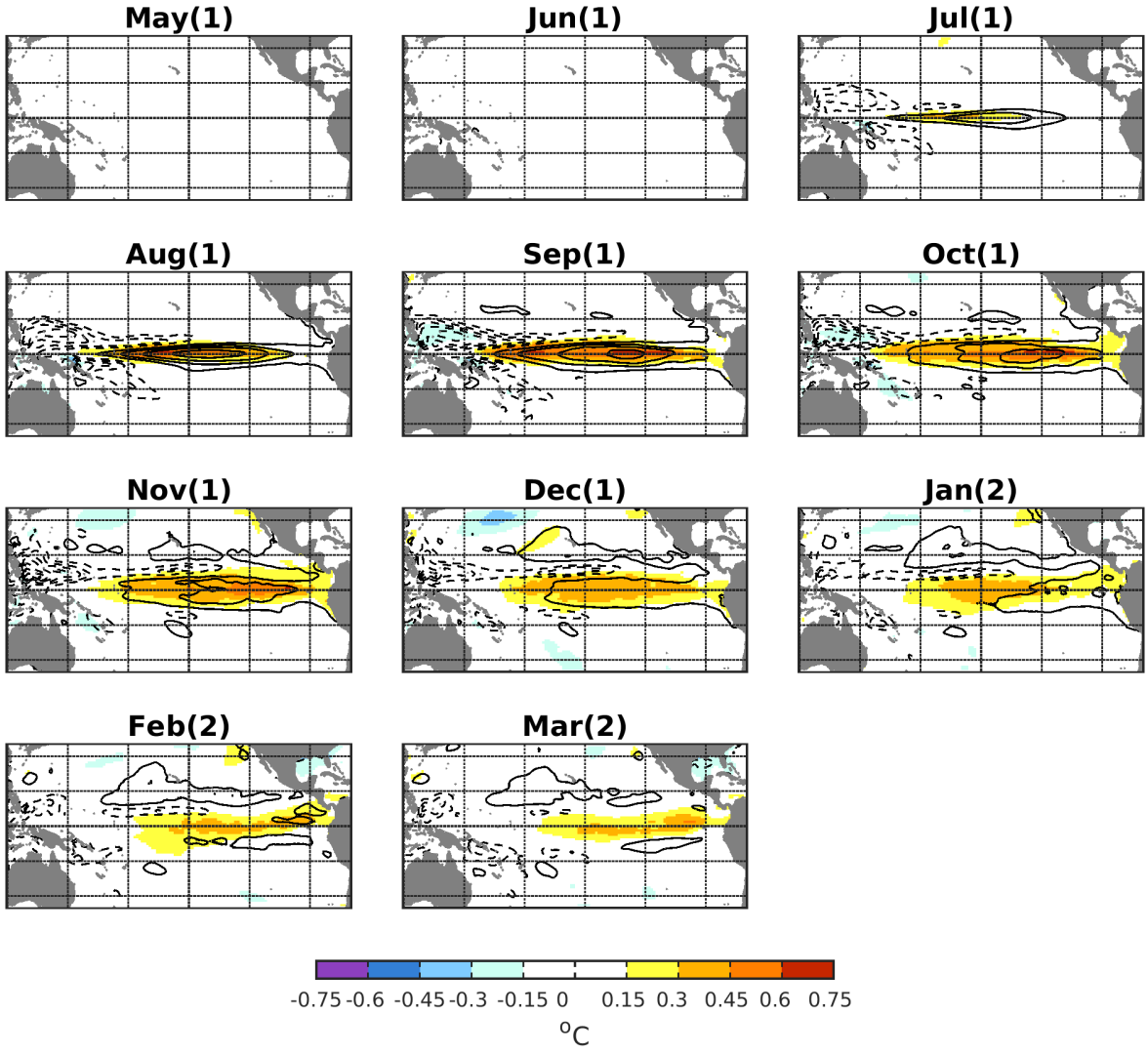

FIGURE 6.7: Monthly evolution (May(1) through March(2)) of the ensemble mean SST (°C; shading) and SSH (cm; contours) response to the JJA EP wind stress forcing. The SSH contour interval is every 1cm where the zero contour has been omitted.

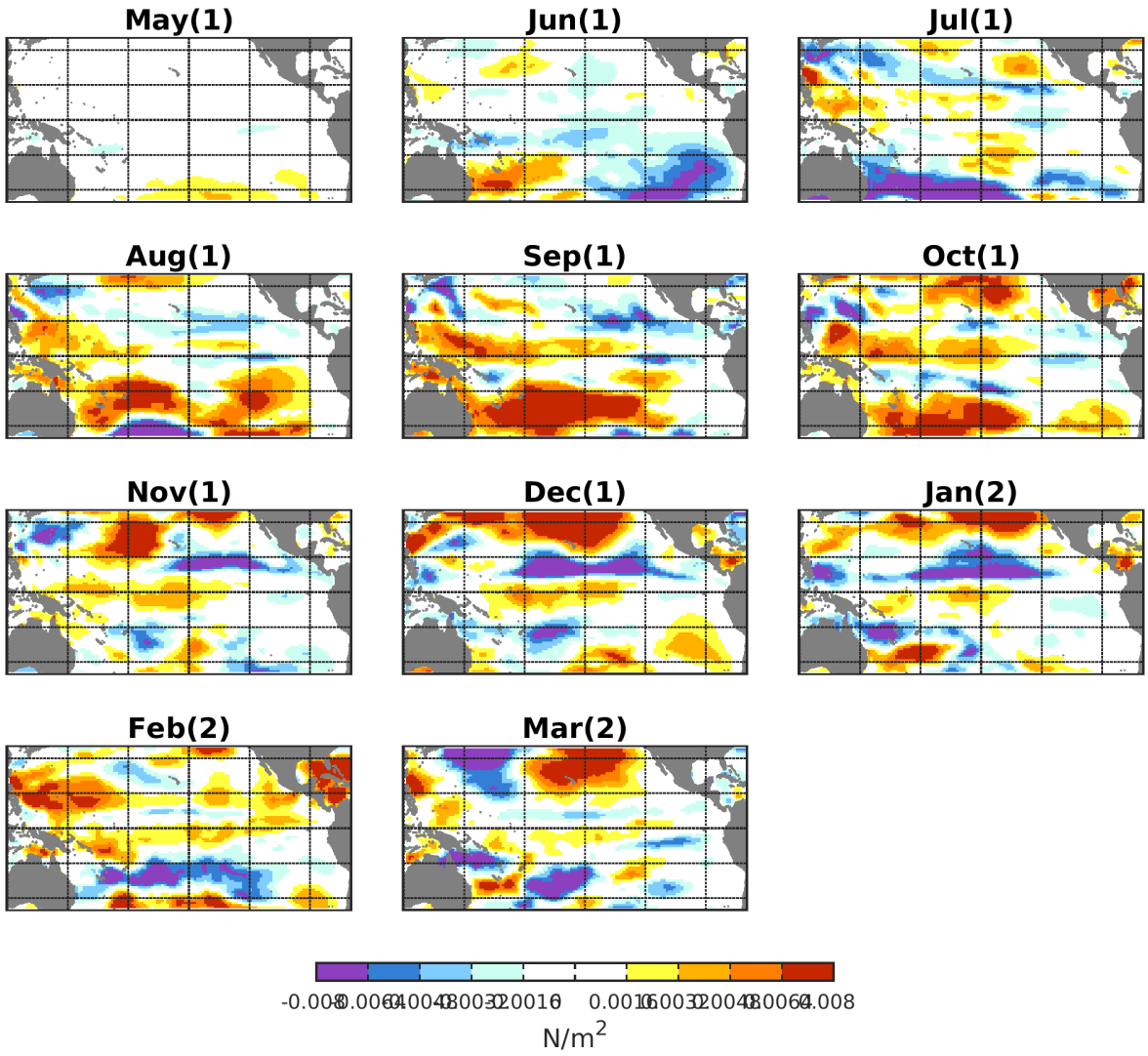

FIGURE 6.8: Monthly evolution (May(1) through March(2)) of the ensemble mean zonal wind stress (TAUX; Nm^{-2}; shading) response to the JJA EP wind stress forcing.

Chapter 7

Conclusions and Discussion

The research presented in this dissertation utilizes a combination of physical model experiments and statistical models to identify i) the interactions between the extra-tropical forcing and ENSO, ii) the role of stochastic forcing on the development of ENSO diversity, and iii) the physical mechanisms connecting noise forcing structures to subsequent ENSO development. In doing so, this work identifies observationally grounded structures within the stochastic forcing and tests the physical mechanisms through which they influence ENSO development. Additionally, this dissertation presents a unique framework that allows us to cleanly parse through the myriad processes that contribute to ENSO diversity. Overall, the approach used in this dissertation addresses ENSO variability by bridging the gap between the 'low frequency oscillation' (i.e ENSO is a self sustained evolution) and 'episodic' (i.e. ENSO events are stochastically forced) theories of ENSO variability.

7.1 Summary of Results

ENSO is the largest source of interannual variability in the tropical Pacific and has profound influences on global climate patterns. However, our understanding of how individual ENSO events are initiated is currently incomplete. ENSO dynamics are difficult to fully understand due to the large spatial and temporal diversity of events as well as a multitude of processes capable of influencing tropical Pacific variability. For example, ENSO diversity is influenced by extra-tropical atmospheric variability, stochastic forcing, and thermocline dynamics. Isolating the interactions between these processes and ENSO development is challenging but necessary in order to improve our understanding of ENSO initiation and potentially increase the skill of ENSO predictability. This thesis presents three separate studies that include (1) a dynamical modeling exercise designed to investigate mechanisms by which the PMM influences ENSO, (2) an observational approach that allows investigation of specific noise structures that influence ENSO diversity, and (3) a physical modeling approach that tests the physical effects of specific noise structures identified from the observational analyses.

An ensemble of physical model experiments isolate the PMM from ENSO variability in the tropical Pacific in order to identify the exact mechanisms responsible for ENSO initiation due to extra-tropical atmospheric forcing. NCAR's CESM (run with a slab ocean) simulates the PMM, but not ENSO variability. An ICM contains the physics necessary to simulate ENSO variability but not the PMM. The combination of these two physical models allows us to identify the dominant mechanisms through which the NPO, the PMM and ENSO interact. Generally, the results indicate the positive (negative) phase of the NPO generates the positive (negative) phase of the PMM which in turn can initiate a warm (cold) ENSO event through the excitation of eastward propagating equatorial

Kelvin waves. However, excited Rossby waves appear to play a significant role in the ENSO response to the negative phase of the PMM. These physical model experiments highlight the importance of deterministic dynamics (namely, Kelvin wave propagation) for ENSO growth due to extra tropical forcing. However, the large spread among ensemble members indicates the role of natural variability cannot be neglected when studying ENSO initiation mechanisms as it has important implications for ENSO predictability. These results imply that further understanding the role of natural variability and noise forcing on ENSO development is necessary to improve predictability of ENSO.

A forecasting framework using a statistical dynamical model, or more specifically, LIM, identifies observationally grounded structures within the noise forcing that contribute to the development of CP and EP ENSO events. In the framework used, noise forcing may lead to non-deterministic growth (forecast error) by pushing the system away from the deterministic trajectory, or it may enhance deterministic growth by generating initial conditions with large projection on to optimal initial states. The results show the noise forcing patterns that push the system toward generating CP optimal initial conditions, and thus lead to CP growth, strongly resemble the boreal winter (DJF) atmospheric pattern located in the north Pacific known as the NPO. The noise forcing patterns related to the EP optimal contain a structure in the south east Pacific during boreal spring (MAM) that strongly resembles a SPO pattern. Additionally, positive zonal wind stress anomalies in the west equatorial Pacific are also associated with the EP optimal initial conditions.

The statistical framework is tested by applying it to several historical ENSO events containing a range of spatial characteristics to estimate the relative roles of the deterministic dynamics and the noise forcing to ENSO diversity. Results show that positive zonal wind anomalies in the equatorial Pacific play a significant role during the development

of the two EP ENSO events analyzed (the 82/83 event and the 97/98 event), although each event evolves under very different conditions. Noise forcing early during the year in 1997 generating initial conditions that were ideal for deterministic ENSO growth and large predictability skill. However, the 82/83 event was much less predicable and the noise forcing was more crucial to the resulting ENSO event late in the year. Additionally, the results show the 2010 CP event was largely stochastically forced and the lack of an ENSO event during 2014 was well predicted by the deterministic forecast. While the results confirm a well known fact that individual ENSO events are influenced by a rich variety of phenomena throughout their evolution, this framework allows us to parse through those phenomena to identify how specific noise forcing processes interact with the low-frequency dynamics in the tropical Pacific to contribute to ENSO diversity for individual events.

Finally, we identify the mechanisms through which the identified noise forcing patterns induce ENSO development through an ensemble of physical model experiments. However, since the model does not exactly simulate the observed climate system, we first identify analogous noise forcing structures within the model. This ensures the model physically reacts to the forcing as expected. The same statistical framework developed in the observational analysis is used on data from the NCAR CESM Large Ensemble (LENS) experiment. In general, the spatial patterns of the noise forcing structures found within CESM match the patterns found in the observational analysis well. The CP noise forcing shows a DJF pattern representative of the NPO. The EP noise forcing shows a SPO-like pattern and positive zonal wind anomalies in the western equatorial Pacific, however, these structures occur during JJA, rather than MAM as seen in observations. The agreement between the model and observational spatial noise patterns, which are also found in previous studies (e.g. Vimont et al. 2003a; You and Furtado 2017; McPhaden

1999), suggests these structures are not statistical artifacts nor model dependent, but rather meaningful to ENSO development. However, physical model experiments must be performed to confirm the physical behaviors of these structures.

Three sets of fully coupled physical model experiments are conducted to test the mechanisms through which three specific noise forcing structures of interest develop into ENSO events and contribute to ENSO diversity. These noise forcing structures force the ocean component of the fully-coupled CESM. The CP noise forcing associated with the NPO during DJF supports previous findings that the NPO can initiate ENSO development through the PMM. The EP noise forcing associated with the SPO during JJA generates some warming in the eastern Pacific but does not excite ENSO development. The EP equatorial wind stress forcing during JJA also only weakly excites EP ENSO growth, though it does generate equatorial waves that are characteristic of ENSO dynamics.

7.2 Overall Context

The research contained within this dissertation takes a new approach to advance scientific understanding of ENSO variability by bridging the gap between two ENSO theories. Although most current research suggests ENSO events are stochastically-forced and episodic, the "oscillation" theories of ENSO variability explain the low frequency dynamics observed during the evolution of ENSO events once they have been initiated. The LIM used in this dissertation accounts for the low frequency, oscillatory behavior of ENSO dynamics, while the method used to estimate the noise forcing accounts for the episodic forcing of ENSO events (see Chapter 3 for a complete description of how the dynamics and noise forcing was estimated). This framework illuminates a key difference between dynamical behaviors of EP and CP events. The wave-like patterns of the EP

optimal suggests EP events contain more oscillatory behavior than CP events. For example, the EP optimal initial conditions and results from the modeling experiments suggest decaying positive EP events are more likely to develop into negative ENSO events than CP events. CP events appear to simply grow and decay as a standing mode.

Furthermore, the research presented in this dissertation explores some of the complex characteristics of the episodic or stochastically forced behaviors of ENSO diversity. Assuming ENSO is stochastically forced (i.e. the episodic theory of ENSO), the prediction skill of ENSO is limited by our understanding of the noise forcing. Therefore, characterizing the noise forcing is necessary in order to better characterize the skill of ENSO predictability and determine the mechanisms responsible for the development of ENSO diversity. This research describes a novel method that can be used to identify specific mechanisms within the stochastic forcing capable of exciting CP and EP spatial characteristics. The results highlight the critical and unpredictable role noise forcing plays on ENSO development. The physical model experiments (Chapters 2 and 6) further clarify the relationship between the NPO, the PMM and ENSO. Additionally, the results from the fully coupled model experiments in Chapter 6 suggest the SPO and SPMM may not be strongly linked to ENSO development, as previous studies suggest.

The results of the EP noise experiments suggest that the identified stochastic forcing mechanisms may not be critical for initiating EP ENSO events. It is possible that instead, these mechanisms become more important once an EP ENSO event is underway; this possibility was not tested in the present analysis. Furthermore, considering the statistical framework used to identify the noise forcing patterns, we must consider the possibility that the structures within this study are statistical artifacts and contain no physical relationship to EP ENSO events. For example, the structures identified may still be a blend of a wide range of phenomena that could influence EP events. Additionally, we

used only a few fields to analyze the noise forcing and may have overlooked some critical component of the noise. Although wind stress and surface heat flux directly influence the ocean, it remains unclear which elements (which spatial regions or which seasons) within the noise forcing are most important for EP generation. With extensive resources and a longer observational record a more complete analysis to identify the mechanisms related to the initiation of EP characteristics could be performed.

Overwhelmingly, the results presented in this dissertation suggest ENSO is difficult to forecast with long lead times due to the wide range of phenomena capable of influencing tropical Pacific variability and the critical role noise forcing plays. Any given ENSO event is strongly shaped by unpredictable, highly variable noise forcing throughout its entire evolution. Although we identify several noise forcing patterns that project onto the CP and EP optimal initial conditions, the occurrence of these noise patterns or optimal initial conditions in nature does not necessarily guarantee the development of an ENSO event.

7.3 Future Research

The research presented in the final chapters of this dissertation is far from complete. Many of the results presented demonstrate interesting characteristics of ENSO behavior that should be examined further. The following ideas are examples of experiments or projects that further advance our understanding of ENSO variability.

One finding from this study is that CP ENSO events tend to amplify and decay, with no real oscillatory behavior, while EP events tend to decay into the opposite phase ENSO event (i.e. a La Niña follows an El Niño). It would be possible to further characterize the oscillatory behavior of CP and EP events by projecting the optimal structures onto the eigenmodes of the LIM. The eigenmodes of the dynamical operator govern the growth and

evolution of the system. The projection of the EP and CP optimals onto the oscillatory eigenmodes (as opposed to the stationary modes) will determine which type of ENSO event is more likely to contain oscillatory behaviors.

The results obtained from the final set of physical model experiments discussed in Chapter 6 are preliminary and need to be further analyzed. In particular, significance testing should be performed and several follow-up experiments should also be conducted to complete this study. For example, only the positive phase of the noise forcing structures were tested. A suite of forced CESM simulations using the negative phase of the noise forcing structures should be run to test the linearity of the forcing mechanisms and the tropical Pacific dynamics. Furthermore, only three noise forcing structures of interest have been tested at this time. The results presented in this dissertation suggest ENSO diversity is influenced by a wide range of phenomena, therefore additional structures contained within the noise forcing should be analyzed and tested. Additionally, the results from the EP noise experiments indicate that the noise forcing necessary for ENSO generation may be the result of multiple forcing mechanisms. For example, neither the heat flux forcing nor wind stress associated with the EP optimal is capable of initiating ENSO development on their own, however, the combination of both forcing mechanisms occurring in tandem may have a different ENSO response and should be tested.

In reality the noise forcing related to CP and EP growth is white in time. This suggests that applying a constant forcing for a three month duration is not necessarily observationally realistic. However, applying a constant forcing is only the first step to understanding how certain noise forcing structures lead to ENSO development. Applying the noise to the model as white noise time series with a mean forcing embedded would more realistically simulate the ENSO response to observed noise forcing. Additionally, several sensitivity

studies should be conducted to determine the importance of the magnitude, timing, and persistence of forcing structures on ENSO development.

We must note the CESM contains biases (in the mean state and ENSO variability). These biases influence the patterns of the CP and EP optimals which in turn may influence the patterns of noise forcing. It is reassuring that the spatial patterns of the noise forcing is consistent between the model and observations. This agreement suggests the noise structures are not simply statistical artifacts, however, it is possible these structures evolve via different dynamics within the real world and the model. It would be exceedingly difficult to resolve this issue, however, the implications of fully resolving the dynamical differences between the model and reality would be highly beneficial for future simulations and model development. One possible route forward would be to develop LIMs from the model and from observations, and investigate how specific structures evolve differently for each system. While unlikely to resolve the specific role of biases in the evolution of ENSO events, this method might be instructive for an overall understanding of how model bias may affect ENSO dynamics.

Lastly, other techniques may prove to be useful to improving our understanding ENSO development. For example, data assimilation techniques could be applied in an unconventional way in order to analyze the role of stochastic forcing on ENSO development. Data assimilation would be used to assimilate certain structures of the CP and EP optimal initial conditions into the model in order to realistically "nudge" the model into generating these optimal structures and result in ENSO growth.

References

Alexander, M. A., I. Bladé, M. Newman, J. R. Lanzante, N.-C. Lau, and J. D. Scott, 2002: The Atmospheric Bridge: The Influence of ENSO Teleconnections on Air–Sea Interaction over the Global Oceans. *Journal of Climate*, **15**, 2205–2231.

Alexander, M. A., L. Matrosova, C. Penland, J. D. Scott, and P. Chang, 2008: Forecasting Pacific SSTs: Linear inverse model predictions of the PDO. *Journal of Climate*, **21**, 385–402, doi:10.1175/2007JCLI1849.1.

Alexander, M. a., D. J. Vimont, P. Chang, and J. D. Scott, 2010: The Impact of Extratropical Atmospheric Variability on ENSO: Testing the Seasonal Footprinting Mechanism Using Coupled Model Experiments. *Journal of Climate*, **23**, 2885–2901, doi:10.1175/2010JCLI3205.1.

An, S. and F. Jin, 2000: An eigen analysis of the interdecadal changes in the structure and frequency of ENSO mode. *Geophysical Research Letters*, **27**, 2573, doi:10.1029/1999GL011090.

An, S. I. and B. Wang, 2000: Interdecadal change of the structure of the ENSO mode and its impact on the ENSO frequency. *Journal of Climate*, **13**, 2044–2055.

Anderson, B. T. and E. Maloney, 2006: Interannual Tropical Pacific Sea Surface Temperatures and Their Relation to Preceding Sea Level Pressures in the NCAR CCSM2. *Journal of Climate*, **19**, 998–1012, doi:10.1175/JCLI3674.1.

Anderson, B. T. and R. C. Perez, 2015: ENSO and non-ENSO induced charging and discharging of the equatorial Pacific. *Climate Dynamics*, **45**, 2309–2327, doi:10.1007/s00382-015-2472-x.

Anderson, B. T., R. C. Perez, and A. Karspeck, 2013: Triggering of El Niño onset through trade wind-induced charging of the equatorial Pacific. *Geophysical Research Letters*, **40**, 1212–1216, doi:10.1002/grl.50200.

Ashok, K., S. K. Behera, S. a. Rao, H. Weng, and T. Yamagata, 2007: El Niño Modoki and its possible teleconnection. *Journal of Geophysical Research: Oceans*, **112**, 1–27, doi:10.1029/2006JC003798.

Ashok, K. and T. Yamagata, 2009: The El Nino with a difference. *Nature*, **461**, 481–484.

Barnett, T., 1977: An attempt to verify some theories of El Nino. *Journal of Physical Oceanography*, **7**, 633–647.

Batstone, C. and H. Hendon, 2005: Characteristics of stochastic variability associated with ENSO and the role of the MJO. *Journal of climate*, **18**, 1773–1789, doi:10.1175/JCLI3374.1.

Battisti, D. S., 1988: Dynamics and Thermodynamics of a Warming Event in a Coupled Tropical Atmosphere–Ocean Model. *Journal of the Atmospheric Sciences*, **45**, 2889–2919.

Battisti, D. S. and A. C. Hirst, 1989: Interannual Variability in a Tropical Atmosphere–Ocean Model: Influence of the Basic State, Ocean Geometry and Nonlinearity. *Journal of the Atmospheric Sciences*, **46**, 1687–1712, doi:10.1175/1520-0469(1989)046¡1687:IVIATA¿2.0.CO;2.

Behringer, D. and Y. Xue, 2004: Evaluation of the Global Ocean Data Assimilation System at NCEP: The Pacific Ocean.

Bjerknes, J., 1969: Atmospheric Teleconnections From The Equatorial Pacific. *Monthly Weather Review*, **97**, 163–172.

Blanke, B., J. D. Neelin, and D. Gutzler, 1997: Estimating the effect of stochastic wind stress forcing on ENSO irregularity. *Journal of Climate*, **10**, 1473–1486.

Boschat, G., P. Terray, and S. Masson, 2013: Extratropical forcing of ENSO. *Geophysical Research Letters*, **40**, 1605–1611, doi:10.1002/grl.50229.

Boulanger, P. and C. Menkes, 1999: Long equatorial wave reflection in the Pacific Ocean from TOPEX / POSEIDON data during the 1992 – 1998 period. *Climate Dynamics*, 205–225.

Cane, M. A. and S. E. Zebiak, 1985: A Theory for El Niño and the Southern Oscillation. *Science*, **228**, 1085–1087.

Capotondi, A., 2013: ENSO diversity in the NCAR CCSM4 climate model. *Journal of Geophysical Research: Oceans*, **118**, 4755–4770, doi:10.1002/jgrc.20335.

Capotondi, A. and P. D. Sardeshmukh, 2015: Optimal precursors of different types of ENSO events. *Geophysical Research Letters*, **42**, 9952–9960, doi:10.1002/2015GL066171.

— 2017: Is El Niño really changing? *Geophysical Research Letters*, doi:10.1002/2017GL074515.

Capotondi, A., A. T. Wittenberg, M. Newman, E. Di Lorenzo, J. Y. Yu, P. Braconnot, J. Cole, B. Dewitte, B. Giese, E. Guilyardi, F. F. Jin, K. Karnauskas, B. Kirtman, T. Lee, N. Schneider, Y. Xue, and S. W. Yeh, 2015: Understanding ENSO Diversity. *Bulletin of the American Meteorological Society*, **96**, 921–938, doi:10.1175/BAMS-D-13-00117.1.

Caviedes, C. N. ., 1975: El Nino 1972 : Its Climatic , Ecological , Human, and Economic Implications. *Geographical Review*, **65**, 493–509.

Chang, P., L. Ji, and H. Li, 1997: A decadal climate variation in the tropical Atlantic Ocean from thermodynamic air-sea interactions. *Nature*, **385**, 516–518.

Chang, P., R. Saravanan, T. DelSole, and F. Wang, 2004: Predictability of linear coupled systems. Part I: Theoretical analyses. *Journal of Climate*, **17**, 1474–1486.

Chang, P., L. Zhang, R. Saravanan, D. J. Vimont, J. C. H. Chiang, L. Ji, H. Seidel, and M. K. Tippett, 2007: Pacific meridional mode and El Nino - Southern oscillation. *Geophysical Research Letters*, **34**, 1–5, doi:10.1029/2007GL030302.

Chen, D., M. A. Cane, A. Kaplan, S. E. Zebiak, and D. Huang, 2004: Predictability of El Niño over the past 148 years. *Nature*, **428**, 733–736, doi:10.1038/nature02439.

Chen, D., T. Lian, C. Fu, M. A. Cane, Y. Tang, R. Murtugudde, X. Song, Q. Wu, and L. Zhou, 2015: Strong influence of westerly wind bursts on El Niño diversity. *Nature Geoscience*, **8**, 339–345, doi:10.1038/ngeo2399.

Chiang, J. and D. Vimont, 2004: Analogous Pacific and Atlantic Meridional Modes of Tropical Atmosphere-Ocean Variability*. *Journal of Climate*, **17**, 4143–4158, doi:10.1175/JCLI4953.1.

Clarke, A. J., 1992: Low-Frequency Reflection From a Nonmeridional Eastern Ocean Boundary and the Use of Coastal Sea-Level To Monitor Eastern Pacific Equatorial Kelvin Waves. *Journal of Physical Oceanography*, **22**, 163–183.

Clement, A., P. DiNezio, and C. Deser, 2011: Rethinking the ocean's role in the Southern Oscillation. *Journal of Climate*, **24**, 4056–4072, doi:10.1175/2011JCLI3973.1.

Coker, R. E., 1918: Ocean Temperatures off the Coast of Peru. *Geographical Review*, **5**, 127–135.

Dayan, H., J. Vialard, T. Izumo, and M. Lengaigne, 2014: Does sea surface temperature outside the tropical Pacific contribute to enhanced ENSO predictability? *Climate Dynamics*, **43**, 1311–1325, doi:10.1007/s00382-013-1946-y.

Deser, C., A. S. Phillips, R. A. Tomas, Y. M. Okumura, M. A. Alexander, A. Capotondi, J. D. Scott, Y.-O. Kwon, and M. Ohba, 2012: ENSO and Pacific Decadal Variability in the Community Climate System Model Version 4. *Journal of Climate*, **25**, 2622–2651, doi:10.1175/JCLI-D-11-00301.1.

Diaz, H. F., M. P. Hoerling, and J. K. Eischeid, 2001: ENSO variability, teleconnections and climate change. *International Journal of Climatology*, **21**, 1845–1862, doi:10.1002/joc.631.

Dijkstra, H. A., 2006: The ENSO phenomenon: theory and mechanisms. *Advances in Geosciences*, **6**, 3–15, doi:10.5194/adgeo-6-3-2006.

Eckert, C. and M. Latif, 1997: Predictability of a stochastically forced hybrid coupled model of El Niño. *Journal of Climate*, **10**, 1488–1504.

Enfield, D. B., 1989: EL NINO , PAST AND PRESENT. *Reviews of Geophysics*, **27**, 159–187.

Fedorov, A. V., S. Hu, M. Lengaigne, and E. Guilyardi, 2015: The impact of westerly wind bursts and ocean initial state on the development, and diversity of El Niño events. *Climate Dynamics*, **44**, 1381–1401, doi:10.1007/s00382-014-2126-4.

Fedorov, A. V. and S. G. Philander, 2000: Is El Niño Changing ? *Science*, **288**, 1997–2002, doi:10.1126/science.288.5473.1997.

— 2001: A stability analysis of tropical ocean-atmosphere interactions: Bridging measurements and theory for El Niño. *Journal of Climate*, **14**, 3086–3101.

Flugel, M. and P. Chang, 1996: Impact of Dynamical and Stochastic Processes on the Predictability of ENSO. *Geophysical Research Letters*, **23**, 2089–2092.

Furtado, J. C., E. Di Lorenzo, B. T. Anderson, and N. Schneider, 2012: Linkages between the North Pacific Oscillation and central tropical Pacific SSTs at low frequencies. *Climate Dynamics*, **39**, 2833–2846, doi:10.1007/s00382-011-1245-4.

Gebbie, G., I. Eisenman, A. Wittenberg, and E. Tziperman, 2007: Modulation of Westerly Wind Bursts by Sea Surface Temperature: A Semistochastic Feedback for ENSO. *Journal of the Atmospheric Sciences*, **64**, 3281–3295, doi:10.1175/JAS4029.1.

Gill, A. E., 1980: Some simple solutions for heat-induced tropical circulation. *Quarterly Journal of the Royal Meteorological Society*, **106**, 447–462, doi:10.1002/qj.49710644905.

Gill, A. E. and E. M. Rasmusson, 1983: The 1982-83 Climate Anomaly in the Equatorial Pacific. *Nature*, **306**, 229–234, doi:10.1038/306229a0.

Godfrey, J. S., 1975: On Ocean Spindown I: A Linear Experiment. *Journal of Physical Oceanography*, **5**, 399–409, doi:10.1175/1520-0485(1975)005¡0399:OOSIAL¿2.0.CO;2.

Graham, N. E. and T. P. Barnett, 1987: Sea Surface Temperature, Surface Wind Divergence, and Convection over Tropical Oceans. *Science*, **238**, 657–659, doi:10.1126/science.238.4827.657.

Graham, N. E. and W. B. White, 1988: The el nino cycle: a natural oscillator of the pacific ocean–atmosphere system. *Science (New York, N.Y.)*, **240**, 1293–302, doi:10.1126/science.240.4857.1293.

Harrison, D. E. and A. M. Chiodi, 2009: Pre- and post-1997/98 Westerly wind events and equatorial pacific cold tongue warming. *Journal of Climate*, **22**, 568–581, doi:10.1175/2008JCLI2270.1.

Hirst, A. C., 1986: Unstable and Damped Equatorial Modes in Simple Coupled Ocean-Atmosphere Models. *Journal of the Atmospheric Sciences*, **43**, 606–632.

Hoerling, M. P., a. Kumar, and M. Zhong, 1997: El Nino, La Nina, and the nonlinearity of their teleconnections. *Journal of Climate*, **10**, 1769–1786.

Horel, J. D. and J. M. Wallace, 1982: Planetary-Scale Atmospheric Phenomena Associated with the Southern Oscillation. *Monthly Weather Review*, **109**, 813–829.

Horii, T., I. Ueki, and K. Hanawa, 2012: Breakdown of ENSO predictors in the 2000s: Decadal changes of recharge/discharge-SST phase relation and atmospheric intraseasonal forcing. *Geophysical Research Letters*, **39**, 2–6, doi:10.1029/2012GL051740.

Hoskins, B. and D. Karoly, 1981: The Steady Linear Reposonse of a Spherical Atmosphere to Thermal and Orographic Forcing. *Journal of the Atmospheric Sciences*, **38**, 1179–1196.

Hu, S. and A. V. Fedorov, 2016: Exceptionally strong easterly wind burst stalling El Niño of 2014. *Proceedings of the National Academy of Sciences*, **113**, 201514182, doi:10.1073/pnas.1514182113.

— 2017: The extreme El Niño of 2015/2016: the role of westerly and easterly wind bursts, and preconditioning by the failed 2014 event. *Climate Dynamics*, **0**, 1–19, doi:10.1007/s00382-017-3531-2.

Hu, S., A. V. Fedorov, M. Lengaigne, and E. Guilyardi, 2014: The impact of westerly wind bursts on the diversity and predictability of El Niño events: An ocean energetics perspective. *Geophysical Research Letters*, **41**, 4654–4663, doi:10.1002/2014GL059573.

Hu, Z. Z., A. Kumar, B. Jha, W. Wang, B. Huang, and B. Huang, 2012: An analysis of warm pool and cold tongue El Niños: Air-sea coupling processes, global influences, and recent trends. *Climate Dynamics*, **38**, 2017–2035, doi:10.1007/s00382-011-1224-9.

Jin, E. K., J. L. Kinter, B. Wang, C. K. Park, I. S. Kang, B. P. Kirtman, J. S. Kug, A. Kumar, J. J. Luo, J. Schemm, J. Shukla, and T. Yamagata, 2008: Current status of ENSO prediction skill in coupled ocean-atmosphere models. *Climate Dynamics*, **31**, 647–664, doi:10.1007/s00382-008-0397-3.

Jin, F. and B. J. Hoskins, 1995: The Direct Response to Tropical Heating in a Baroclinic Atmosphere.

Jin, F.-F., 1997: An Equatorial Ocean Recharge Paradigm for ENSO. Part I: Conceptual Model. *Journal of the Atmospheric Sciences*, **54**, 830–847.

Julian, P. R. and R. M. Chervin, 1978: A Study of the Southern Oscillation and Walker Circulation Phenomenon. *Monthly Weather Review*, **106**, 1433–1451, doi:10.1175/1520-0493(1978)106¡1433:ASOTSO¿2.0.CO;2.

Kao, H.-Y. and J.-Y. Yu, 2009: Contrasting Eastern-Pacific and Central-Pacific Types of ENSO. *Journal of Climate*, **22**, 615–632, doi:10.1175/2008JCLI2309.1.

Kapur, A. and C. Zhang, 2012: Multiplicative MJO Forcing of ENSO. *Journal of Climate*, **25**, 8132–8147, doi:10.1175/JCLI-D-11-00609.1.

Kapur, A., C. Zhang, J. Zavala-Garay, and H. H. Hendon, 2011: Role of stochastic forcing in ENSO in observations and a coupled GCM. *Climate Dynamics*, **38**, 87–107, doi:10.1007/s00382-011-1070-9.

Karnauskas, K. B., 2013: Can we distinguish canonical El Niño from Modoki? *Geophysical Research Letters*, **40**, 5246–5251, doi:10.1002/grl.51007.

Kay, J. E., C. Deser, A. Phillips, A. Mai, C. Hannay, G. Strand, J. M. Arblaster, S. C. Bates, G. Danabasoglu, J. Edwards, M. Holland, P. Kushner, J. F. Lamarque, D. Lawrence, K. Lindsay, A. Middleton, E. Munoz, R. Neale, K. Oleson, L. Polvani, and M. Vertenstein, 2015: The community earth system model (CESM) large ensemble project : A community resource for studying climate change in the presence of internal climate variability. *Bulletin of the American Meteorological Society*, **96**, 1333–1349, doi:10.1175/BAMS-D-13-00255.1.

Kessler, W. S., 1991: Can Reflected Extra-equatorial Rossby Waves Drive ENSO? *Journal of Physical Oceanography*, **21**, 444–452.

— 2002: Is ENSO a cycle or a series of events ? *Geophys. Res. Lett.*, **29**, 2125, doi:10.1029/2002GL015924.

Kim, J.-S., K.-Y. Kim, and S.-W. Yeh, 2012a: Statistical evidence for the natural variation of the Central Pacific El Niño. *Journal of Geophysical Research*, **117**, 1–9, doi:10.1029/2012JC008003.

Kim, S. T., J.-Y. Yu, A. Kumar, and H. Wang, 2012b: Examination of the Two Types of ENSO in the NCEP CFS Model and Its Extratropical Associations. *Monthly Weather Review*, **140**, 1908–1923, doi:10.1175/MWR-D-11-00300.1.

Kleeman, R. and A. M. Moore, 1997: A theory for the limitation of ENSO predictability due to stochastic atmospheric transients. *Journal of the Atmospheric Sciences*, 54(6), 753–767, March 15, 1997.

Kleeman, R. and S. B. Power, 1994: Limits to predictability in a coupled ocean-atmosphere model due to atmospheric noise. *Tellus A*, **46**, 529–540, doi:10.1034/j.1600-0870.1994.00014.x.

Kug, J. S., J. Choi, S. I. An, F. F. Jin, and A. T. Wittenberg, 2010a: Warm pool and cold tongue El Niño events as simulated by the GFDL 2.1 coupled GCM. *Journal of Climate*, **23**, 1226–1239, doi:10.1175/2009JCLI3293.1.

Kug, J. S., F. F. Jin, and S. I. An, 2009: Two types of El Niño events: Cold tongue El Niño and warm pool El Niño. *Journal of Climate*, **22**, 1499–1515, doi:10.1175/2008JCLI2624.1.

Kug, J. S., K. P. Sooraj, T. Li, and F. F. Jin, 2010b: Precursors of the El Niño/La Niña onset and their interrelationship. *Journal of Geophysical Research Atmospheres*, **115**, 1–9, doi:10.1029/2009JD012861.

Kumar, K. K., B. Rajagopalan, M. Hoerling, G. Bates, and M. Cane, 2006: Unraveling the Mystery of Indian Monsoon Failure During El Nino. *Science*, **314**, 115–119.

Larkin, N. K. and D. E. Harrison, 2002: ENSO warm (El Nino) and cold (La Nina) event life cycles: Ocean surface anomaly patterns, their symmetries, asymmetries, and implications. *Journal of Climate*, **15**, 1118–1140.

— 2005: Global seasonal temperature and precipitation anomalies during El Nino autumn and winter. *Geophysical Research Letters*, **32**, 1–4, doi:10.1029/2005GL022860.

Larson, S. and B. Kirtman, 2013: The Pacific Meridional Mode as a trigger for ENSO in a high-resolution coupled model. *Geophysical Research Letters*, **40**, 3189–3194, doi:10.1002/grl.50571.

Larson, S. M. and B. P. Kirtman, 2014: The Pacific Meridional Mode as an ENSO Precursor and Predictor in the North American Multi-Model Ensemble. *Journal of Climate*, **27**, 7018–7032, doi:10.1175/JCLI-D-14-00055.1.

— 2015: An alternate approach to ensemble ENSO forecast spread: Application to the 2014 forecast. *Geophysical Research Letters*, n/a–n/a, doi:10.1002/2015GL066173.

Latif, M., D. Anderson, T. Barnett, M. Cane, R. Kleeman, A. Leetmaa, J. O'Brien, A. Rosati, and E. Schneider, 1998: A review of the predictability and prediction of ENSO. *Journal of Geophysical Research*, **103**, 14375, doi:10.1029/97JC03413.

Lengaigne, M., J.-P. Boulanger, C. Menkes, S. Masson, G. Madec, and P. Delecluse, 2002: Ocean response to the March 1997 Westerly Wind Event. *Journal of Geophysical Research: Oceans*, **107**, SRF 16–1–SRF 16–20, doi:10.1029/2001JC000841.

Lengaigne, M., E. Guilyardi, J. P. Boulanger, C. Menkes, P. Delecluse, P. Inness, J. Cole, and J. Slingo, 2004: Triggering of El Niño by westerly wind events in a coupled general circulation model. *Climate Dynamics*, **23**, 601–620, doi:10.1007/s00382-004-0457-2.

Levine, A. F. and F. F. Jin, 2017: A simple approach to quantifying the noise-ENSO interaction. Part I: deducing the state-dependency of the windstress forcing using monthly mean data. *Climate Dynamics*, **48**, 1–18, doi:10.1007/s00382-015-2748-1.

Lin, C.-Y., J.-Y. Yu, and H.-H. Hsu, 2014: CMIP5 model simulations of the Pacific meridional mode and its connection to the two types of ENSO. *International Journal of Climatology*, n/a–n/a, doi:10.1002/joc.4130.

Linkin, M. E. and S. Nigam, 2008: The North Pacific Oscillation–West Pacific Teleconnection Pattern: Mature-Phase Structure and Winter Impacts. *Journal of Climate*, **21**, 1979–1997, doi:10.1175/2007JCLI2048.1.

Liu, Z. and S. Xie, 1994: Equatorward Propagation of Coupled Air–Sea Disturbances with Application to the Annual Cycle of the Eastern Tropical Pacific. *Journal of the Atmospheric Sciences*, **51**, 3807–3822, doi:10.1175/1520-0469(1994)051¡3807:EPOCAD¿2.0.CO;2.

Lockyer, N. and W. J. . S. . Lockyer, 1902: On the Similarity of the Short-Period Pressure Variation over Large Areas. *Proceedings of the Royal Society of London*, volume 71, 134–135.

Lopez, H. and B. P. Kirtman, 2013: Westerly wind bursts and the diversity of ENSO in CCSM3 and CCSM4. *Geophysical Research Letters*, **40**, 4722–4727, doi:10.1002/grl.50913.

Ma, J., S.-P. Xie, H. Xu, J. Ma, S.-P. Xie, and H. Xu, 2017: Contributions of the North Pacific Meridional Mode to Ensemble Spread of ENSO Prediction. *Journal of Climate*, **30**, 9167–9181, doi:10.1175/JCLI-D-17-0182.1.

McPhaden, M. J., 1999: Genesis and Evolution of the 1997-98 El Niño. *Science*, **283**, 950–955, doi:10.5753/cbie.wcbie.2015.1007.

McPhaden, M. J., A. J. Busalacchi, R. Cheney, J.-R. Donguy, K. S. Gage, D. Halpern, M. Ji, P. Julian, G. Meyers, G. T. Mitchum, P. P. Niiler, J. Picaut, R. W. Reynolds,

N. Smith, and K. Takeuchi, 1998: The Tropical Ocean-Global Atmosphere observing system: A decade of progress. *Journal of Geophysical Research*, **103**, 14169, doi:10.1029/97JC02906.

McPhaden, M. J., S. E. Zebiak, and M. H. Glantz, 2006: ENSO as an Integrating Concept in Earth Science. *Science*, **314**, 1740–1745, doi:10.1126/science.1132588.

Meinen, C. S. and M. J. McPhaden, 2000: Observations of Warm Water Volume Changes in the Equatorial Pacific and Their Relationship to El Nino and La Nina. *Journal of Climate*, **13**, 3551–3559.

Min, Q., J. Su, R. Zhang, Q. Min, J. Su, and R. Zhang, 2017: Impact of the South and North Pacific Meridional Modes on the El Niño–Southern Oscillation: Observational Analysis and Comparison. *Journal of Climate*, **30**, 1705–1720, doi:10.1175/JCLI-D-16-0063.1.

Moore, A. M. and R. Kleeman, 1999: Stochastic forcing of ENSO by the intraseasonal oscillation. *Journal of Climate*, **12**, 1199–1220.

Murphy, R. C., 1923: The Oceanography of the Peruvian Littoral with Reference to the Abundance and Distribution of Marine Life. *Geographical Review*, **13**, 64–85.

— 1926: Oceanic and Climatic Phenomena along the West Coast of South America during 1925. *Geographical Review*, **16**, 26–54.

Neelin, J. D., D. S. Battisti, A. C. Hirst, F.-F. Jin, Y. Wakata, T. Yamagata, and S. E. Zebiak, 1998: ENSO theory. *Journal of Geophysical Research*, **103**, 14261, doi:10.1029/97JC03424.

Newman, M., 2007: Interannual to decadal predictability of tropical and North Pacific sea surface temperatures. *Journal of Climate*, **20**, 2333–2356, doi:10.1175/JCLI4165.1.

Newman, M., M. A. Alexander, and J. D. Scott, 2011a: An empirical model of tropical ocean dynamics. *Climate Dynamics*, **37**, 1823–1841, doi:10.1007/s00382-011-1034-0.

Newman, M. and P. D. Sardeshmukh, 2017: Are we near the predictability limit of tropical Indo-Pacific sea surface temperatures? *Geophysical Research Letters*, **44**, 5807–5817, doi:10.1002/2017GL074088.

Newman, M., S.-I. Shin, and M. A. Alexander, 2011b: Natural variation in ENSO flavors. *Geophysical Research Letters*, **38**, n/a–n/a, doi:10.1029/2011GL047658.

Okumura, Y. M. and C. Deser, 2010: Asymmetry in the Duration of El Niño and La Niña. *Journal of Climate*, **23**, 5826–5843, doi:10.1175/2010JCLI3592.1.

Park, J.-Y., S.-W. Yeh, J.-S. Kug, and J. Yoon, 2013: Favorable connections between seasonal footprinting mechanism and El Niño. *Climate Dynamics*, **40**, 1169–1181, doi:10.1007/s00382-012-1477-y.

Pegion, K. and M. Alexander, 2013: The seasonal footprinting mechanism in CFSv2: Simulation and impact on ENSO prediction. *Climate Dynamics*, **41**, 1671–1683, doi:10.1007/s00382-013-1887-5.

Penland, C., 1996: A stochastic model of IndoPacific sea surface temperature anomalies. *Physica D*, **98**, 534–558, doi:10.1016/0167-2789(96)00124-8.

— 2010: A Linear Stochastic Model of Tropical Sea Surface Temperatures Related to El Niño. *Climate Dynamics: Why Does Climate Vary?*, D.-Z. Sun and F. Bryan, eds., American Geophysical Union, Washington, D.C., 65–77.

Penland, C. and L. Hartten, 2014: Stochastic forcing of north tropical Atlantic sea surface temperatures by the North Atlantic Oscillation. *Geophysical Research Letters*, 2126–2132, doi:10.1002/2014GL059252.Received.

Penland, C. and T. Magorian, 1993: Prediction of Niño 3 sea surface temperatures using linear inverse modeling. *Journal of Climate*, **6**, 1067–1076, doi:10.1175/1520-0442(1993)006¡1067:PONSST¿2.0.CO;2.

Penland, C. and L. Matrosova, 1998: Prediction of Tropical Atlantic Sea Surface Temperatures Using Linear Inverse Modeling. *Journal of Climate*, **11**, 483–496.

— 2006: Studies of El Niño and interdecadal variability in tropical sea surface temperatures using a nonnormal filter. *Journal of Climate*, **19**, 5796–5815, doi:10.1175/JCLI3951.1.

— 2008: A Southern Hemisphere footprint in American Midwest precipitation. *Geophysical Research Letters*, **35**, 1–5, doi:10.1029/2008GL033612.

Penland, C. and P. Sardeshmukh, 1995: The optimal growth of tropical sea surface temperature anomalies. *Journal of climate*, **8**, 1999–2024.

Pezet, F., 1895: The counter-current El Niño on the coast of Northern Peru. *Sixth International Geographical Congress*, 603–606.

Philander, G. S., 1990: *El Nino, La Nina, and the Southern Oscillation*, volume 46. Academic Press.

Rasmusson, E. M. and T. H. Carpenter, 1982: Variations in tropical sea surface temperature and surface wind fields associated with the Southern Oscillation/El Niño. *Monthly Weather Review*, **110**, 354–384, doi:10.1175/1520-0493(1982)110¡0354:VITSST¿2.0.CO;2.

Rebert, J. P., J. R. Donguy, G. Eldin, and K. Wyrtki, 1985: Relations between sea level, thermocline depth, heat content, and dynamic height in the tropical Pacific Ocean. *Journal of Geophysical Research*, **90**, 11719, doi:10.1029/JC090iC06p11719.

Reynolds, R. W., N. A. Rayner, T. M. Smith, D. C. Stokes, and W. Wang, 2002: An improved in situ and satellite SST analysis for climate. *Journal of Climate*, **15**, 1609–1625.

Rogers, J. C., 1981: The North Pacific Oscillation. *Journal of Climatology*, **1**, 39–57, doi:10.1002/joc.3370010106.

Schopf, P. S. and M. J. Suarez, 1988: Vacillations in a coupled ocean-atmosphere model. *Journal of Atmospheric Sciences*, **45**, 549–566, doi:10.1175/1520-0469(1988)045

Sheinbaum, J., 2003: Current theories on El Niño-Southern Oscillation : A review. *Geofísica Internacional*, **42**, 291–305.

Suarez, M. J. and P. S. Schopf, 1988: A Delayed Action Oscillator for ENSO. *Journal of the Atmospheric Sciences*, **45**, 3283–3287.

Takahashi, K., A. Montecinos, K. Goubanova, and B. Dewitte, 2011: ENSO regimes: Reinterpreting the canonical and Modoki El Niño. *Geophysical Research Letters*, **38**, doi:10.1029/2011GL047364.

Thomas, E. E. and D. J. Vimont, 2016: Modeling the Mechanisms of Linear and Nonlinear ENSO Responses to the Pacific Meridional Mode. *Journal of Climate*, **29**, 8745–8761, doi:10.1175/JCLI-D-16-0090.1.

Thompson, C. J. and D. S. Battisti, 2001: A linear stochastic dynamical model of ENSO. Part II: Analysis. *Journal of Climate*, **14**, 445–466.

Trenberth, K. E., G. W. Branstator, D. Karoly, A. Kumar, N.-C. Lau, and C. Ropelewski, 1998: Progress during TOGA in understanding and modeling global teleconnections associated with tropical sea surface temperatures. *Journal of Geophysical Research*, **103**, 14291, doi:10.1029/97JC01444.

Tziperman, E., L. Zanna, and C. Penland, 2008: Nonnormal Thermohaline Circulation Dynamics in a Coupled Ocean–Atmosphere GCM. *Journal of Physical Oceanography*, **38**, 588–604, doi:10.1175/2007JPO3769.1.

Vimont, D., D. Battisti, and A. Hirst, 2001: Footprinting: A seasonal connection between the tropics and mid-latitudes. *Geophysical research letters*, **60278**, 6–9, doi:10.1029/2001GL013435.

Vimont, D., J. Wallace, and D. Battisti, 2003a: The seasonal footprinting mechanism in the Pacific: implications for ENSO*. *Journal of climate*, 2668–2675.

Vimont, D. J., 2010: Transient Growth of Thermodynamically Coupled Variations in the Tropics under an Equatorially Symmetric Mean State*. *Journal of Climate*, **23**, 5771–5789, doi:10.1175/2010JCLI3532.1.

Vimont, D. J., M. Alexander, and A. Fontaine, 2009: Midlatitude Excitation of Tropical Variability in the Pacific: The Role of Thermodynamic Coupling and Seasonality*. *Journal of Climate*, **22**, 518–534, doi:10.1175/2008JCLI2220.1.

Vimont, D. J., M. A. Alexander, and M. Newman, 2014: Optimal growth of Central and East Pacific ENSO events. *Geophysical Research Letters*, **41**, 4027–4034, doi:10.1002/2014GL059997.

Vimont, D. J., D. S. Battisti, and A. C. Hirst, 2003b: The Seasonal Footprinting Mechanism in the CSIRO Coupled General Circulation Models*. *Journal of Climate*, **16**, 2653–2667.

Walcott, F. C., 1925: An Expedition to the Laguna Colorada, Southern Bolivia: With a Note on the recent occurrence of El Niño. *Geographical Review*, **15**, 345–366.

Walker, G., 1928: World Weather. *Quarterly Journal Royal Meteoh1Ological Society*, **5**, 79–87.

Walker, G. T. and E. W. Bliss, 1932: World Weather V. *Memoirs of the Royal Meteorological Society*, **4**, 53–84.

Wallace, J. M., E. M. Rasmusson, T. P. Mitchell, V. E. Kousky, E. S. Sarachik, and H. von Storch, 1998: On the structure and evolution of ENSO-related climate variability in the tropical Pacific: Lessons from TOGA. *Journal of Geophysical Research*, **103**, 14241, doi:10.1029/97JC02905.

Wang, B. and S. I. An, 2002: A mechanism for decadal changes of ENSO behavior: Roles of background wind changes. *Climate Dynamics*, **18**, 475–486, doi:10.1007/s00382-001-0189-5.

Weng, H., K. Ashok, S. K. Behera, S. a. Rao, and T. Yamagata, 2007: Impacts of recent El Nino Modoki on dry/wet conditions in the Pacific rim during boreal summer. *Climate Dynamics*, **29**, 113–129, doi:10.1007/s00382-007-0234-0.

Weng, H., S. K. Behera, and T. Yamagata, 2009: Anomalous winter climate conditions in the Pacific rim during recent El Nino Modoki and El Nino events. *Climate Dynamics*, **32**, 663–674, doi:10.1007/s00382-008-0394-6.

Wyrtki, K., 1975: El Niño—The Dynamic Response of the Equatorial Pacific Oceanto Atmospheric Forcing. *Journal of Physical Oceanography*, **5**, 572–584, doi:10.1175/1520-0485(1975)005¡0572:ENTDRO¿2.0.CO;2.

Xie, S.-P. and S. G. H. Philander, 1994: A coupled ocean-atmosphere model of relevance to the ITCZ in the eastern Pacific. *Tellus A*, **46**, 340–350, doi:10.3402/tellusa.v46i4.15484.

Yeh, S.-w., J.-s. Kug, B. Dewitte, M.-h. Kwon, B. P. Kirtman, and F.-f. Jin, 2009: El Niño in a changing climate. *Nature*, **461**, 511–4, doi:10.1038/nature08316.

You, Y. and J. C. Furtado, 2017: The role of South Pacific atmospheric variability in the development of different types of ENSO. *Geophysical Research Letters*, 1–9, doi:10.1002/2017GL073475.

Yu, J.-Y. and S. T. Kim, 2011: Relationships between Extratropical Sea Level Pressure Variations and the Central Pacific and Eastern Pacific Types of ENSO. *Journal of Climate*, **24**, 708–720, doi:10.1175/2010JCLI3688.1.

Zavala-Garay, J. and A. Moore, 2003: The response of a coupled model of ENSO to observed estimates of stochastic forcing. *Journal of Climate*, 2827–2842.

Zebiak, S. E. and M. A. Cane, 1987: A Model El Nino-Southern Oscillation. *Monthly Weather Review*, **115**.

Zhang, H., A. Clement, and P. Di Nezio, 2014: The South Pacific Meridional Mode: A Mechanism for ENSO-like Variability. *Journal of Climate*, **27**, 769–783, doi:10.1175/JCLI-D-13-00082.1.

Zhang, L., P. Chang, and L. Ji, 2009: Linking the Pacific meridional mode to ENSO: Coupled model analysis. *Journal of Climate*, **22**, 3488–3505, doi:10.1175/2008JCLI2473.1.

Zhu, J., A. Kumar, and B. Huang, 2015: The relationship between thermocline depth and SST anomalies in the eastern equatorial Pacific: Seasonality and decadal variations. *Geophysical Research Letters*, **42**, 4507–4515, doi:10.1002/2015GL064220.